Technische Universität München
TUM School of Engineering and Design

Local modeling and uncertainty quantification of the linear flame response

Alexander Avdonin

Vollständiger Abdruck der von der TUM School of Engineering and Design der Technischen Universität München zur Erlangung des akademischen Grades eines

Doktors der Ingenieurwissenschaften

genehmigten Dissertation.

Vorsitzender:
Prof. Dr.-Ing. Oskar J. Haidn
Prüfer der Dissertation:
1. Prof. Wolfgang Polifke, Ph.D.
2. Prof. Michael Bauerheim, Ph.D.

Die Dissertation wurde am 02.11.2021 bei der Technischen Universität München eingereicht und durch die TUM School of Engineering and Design am 03.02.2022 angenommen.

Abstract

This thesis and the corresponding publications cover the local modeling and uncertainty quantification of the linear flame response. The local flame modeling is required at high frequencies when the flame is no longer acoustically compact. This thesis suggests to model a local flame response by the *linearized reactive flow* (LRF) approach. This approach is analytically derived by linearizing the Navier-Stokes equations and transport equations for reacting species. Therefore, the LRF includes a flow–flame–acoustics interaction by design. As a proof of concept, the LRF approach is applied to an attached and a lifted laminar premixed flame in a low-frequency regime. The flame transfer functions (FTFs) computed with the LRF solver agree with the reference FTFs identified from the CFD simulation with a broadband excitation. The LRF solver also computes thermo-acoustic eigenmodes of the laminar flames, i.e. the mode growth-rate, frequency, and shape. Results are compared to the established hybrid methods that couple FTFs with a low-order thermoacoustic network-model or with a linearized Navier-Stokes equations solver. All solvers capture the dominant thermoacoustic mode, but only the LRF resolves the local flow-flame interaction, revealing e.g. the onset of the flame movement and the convective propagation of distortions along the flame. Although this example demonstrates that the LRF approach works well for laminar flames in the low-frequency regime, the first application of the LRF solver to a turbulent auto-ignition flame at high frequencies gives results that do not agree at all with the CFD results. Nevertheless, a significant result is achieved: a simplified formulation of the LRF (neglecting convection and one part of the reaction term) yields a conservation equation for the fluctuating heat-release rate that captures the acoustic flame motion. This simplified LRF model is compared against two other sophisticated linear local flame models: the *Eulerian Flame Acoustic Motion Equation* by Méry [70] and the *flame displacement model* by Zellhuber and Schwing [114].

The linear flame response models are developed to perform a fast stability analysis of combustion systems. Nevertheless, the real-life combustion systems include many uncertain parameters such as operating conditions, so the linear stability analysis has to be combined with an uncertainty quantification to estimate the probability of instability. This thesis shows how to incorporate uncertainties in the modeling of the linear flame response using a *non-intrusive polynomial chaos expansion* (NIPCE). The NIPCE is a simple black-box approach that perfectly suits problems with expensive system evaluations, e.g. CFD simulations, where it is unfeasible to generate enough samples to propagate uncertainties confidently using a Monte Carlo technique. Instead, the NIPCE requires only a few samples and can perform sensitivity analysis as well. This thesis performs uncertainty quantification and sensitivity analysis of thermoacoustic stability for two premixed flame configurations. The first configuration is a turbulent swirl combustor, modeled by the Helmholtz equation with an $n-\tau$ flame; the flame parameters and the outlet reflection

coefficients are uncertain. The first-order NIPCE suffices to yield an accurate growth rate of the combustor. The second configuration is a laminar slit burner. Its stability is investigated using a low-order network model with the flame transfer function identified from the reactive flow CFD simulations. The uncertainties come from the boundary conditions in the CFD simulations (flow velocity, burner-plate temperature, and equivalence ratio) and acoustic reflection coefficients in the network model. In this case, the second-order NIPCE is sufficient to model the uncertainties in the growth rate. Additionally, it is shown how to propagate the uncertain boundary conditions in the CFD to the flame transfer function and identify the most dominant uncertain parameters using Sobol indices.

Kurzfassung

Diese Arbeit und die dazugehörenden Publikationen befassen sich mit der lokalen Modellierung und Unsicherheitsquantifizierung der linearen Flammenantwort. Die lokale Modellierung der linearen Flammenantwort ist die bei hohen Frequenzen erforderlich, weil die Flamme nicht mehr akustisch kompakt ist. Es wird vorgeschlagen, ein lokales Flammenverhalten durch den *linearized reactive flow* (LRF) Ansatz zu modellieren. Dieser Ansatz wird analytisch durch Linearisierung der Navier-Stokes- und Transportgleichungen für reagierende Spezies hergeleitet. Daher beinhaltet das LRF eine Interaktion zwischen Strömung, Akustik und Flamme. Als Konzeptnachweis wird der LRF-Ansatz auf eine angehängte und eine angehobene laminare vorgemischte Flamme in einem niederfrequenten Bereich angewendet. Die mit dem LRF-Löser berechneten FTFs stimmen mit den aus den CFD-Zeitreihen ermittelten Referenz-FTFs überein. Der LRF-Löser berechnet auch die thermoakustischen Eigenmoden der laminaren Flammen, d.h. die Wachstumsrate, Frequenz und Form. Die Ergebnisse werden mit den etablierten hybriden Methoden verglichen die FTFs mit einem thermoakustischen Netzwerkmodell oder mit einem linearisierten Navier-Stokes-Löser koppeln. Alle drei Löser sind in der Lage die instabilen Moden zu bestimmen, aber nur der LRF-Löser löst die Interaktion zwischen Strömung, Akustik und Flamme örtlich auf und kann deshalb den Ansatz der Flammenbewegung andeuten. Obwohl dieses Beispiel beweist, dass der LRF-Ansatz für laminare Flammen im niederfrequenten Bereich gut funktioniert, scheitert die erste Anwendung des LRF-Lösers auf eine turbulente Selbstzündungsflamme bei hohen Frequenzen. Dennoch wird ein wichtiges Ergebnis erzielt: eine vereinfachte Formulierung des LRF (Vernachlässigung der Konvektion und eines Teils des Reaktionsterms) liefert eine Erhaltungsgleichung für die fluktuierende Wärmefreisetzungsrate, die eine akustische Flammenbewegung darstellt. Das vereinfachte LRF-Modell wird mit zwei anderen hochwertigen linearen lokalen Flammenmodellen verglichen: der *Eulerian Flame Acoustic Motion Equation* von Méry [70] und dem *Flammenverschiebungsmodell* von Zellhuber und Schwing [114].

Die linearen Flammenantwortmodelle wurden entwickelt, um eine schnelle Stabilitätsanalyse von Verbrennungssystemen durchzuführen. Dennoch, muss die lineare Stabilitätsanalyse mit einer Quantifizierung der Unsicherheit kombiniert werden, um die Wahrscheinlichkeit der Instabilität abzuschätzen. In dieser Arbeit wird gezeigt, wie die Unsicherheiten bei der Modellierung des linearen Flammenverhaltens mit *non-intrusive polynomial chaos expansion* (NIPCE) quantifiziert werden. Das NIPCE ist ein einfacher Black-Box-Ansatz, der sich hervorragend für Probleme mit teuren Systemauswertungen eignet, z. B. CFD-Simulationen, bei denen es unmöglich ist, genügend Stichproben zu generieren, um Unsicherheiten mit der Monte-Carlo Methode auszurechen. Stattdessen benötigt das NIPCE nur wenige Stichproben und kann zusätzlich auch eine Sensitivitätsanalyse durchführen. In dieser Arbeit wird eine Unsicherheitsquan-

tifizierung (UQ) und Sensitivitätsanalyse der thermoakustischen Stabilität von zwei vorgemischten Flammenkonfigurationen durchgeführt. Die erste Konfiguration ist ein turbulenter Drallbrenner, der durch die Helmholtz-Gleichung mit einer $n-\tau$ Flamme modelliert wird; die Flammenparameter und die Auslassreflexionskoeffizienten sind unsicher. Das NIPCE erster Ordnung reicht aus, um eine genaue Wachstumsrate der Brennkammer zu erhalten. Die zweite Konfiguration ist ein laminarer Schlitzbrenner. Seine Stabilität wird unter Verwendung eines Netzwerkmodells niederer Ordnung mit der Flammentransferfunktion (FTF) untersucht. Die FTF wird aus den CFD-Simulationen der reaktiven Strömung identifiziert. Die Unsicherheiten kommen von den Randbedingungen in den CFD-Simulationen (Strömungsgeschwindigkeit, Brennerplattentemperatur und Äquivalenzverhältnis) und den akustischen Reflexionskoeffizienten im Netzwerkmodell. In diesem Fall ist das NIPCE zweiter Ordnung ausreichend, um die Unsicherheiten in der Wachstumsrate zu modellieren. Zusätzlich wird es gezeigt, wie die unsicheren Randbedingungen in CFD-Simulationen sich auf die FTF übertragen lassen und die dominanten unsicheren Parameter mit Sobol-Indizes identifiziert werden.

Acknowledgment

I gratefully acknowledge funding provided by the German Federal Ministry for Economics & Energy (FKZ 03ET7021U) and GE Power. The investigations were conducted in the framework of the joint research program AG Turbo (COOREFLEX-turbo 2.1.2c). The Gauss Centre for Supercomputing e.V. provided computing time on the GCS Supercomputer SuperMUC (grant pr27je) and on the CooLMUC2 Cluster (grant pr94ho) at Leibniz Supercomputing Centre.

I would like to thank my supervisor Prof. Wolfgang Polifke for the incredible clever guidance. It was an honor for me to work under your supervision! When I had a problem, you always gave me a direction where to search for an answer. Only after leaving the university, I understood how many valuable things you taught me that help me now in my career development as an engineer and researcher. Thank you!

Furthermore, I would like to thank my colleague Maximilian Meindl for a pleasant and fruitful work together. I always remember this time with great joy!

I would like to thank Helga Basset and Sigrid Schulz-Reichwald for their eternal readiness to help me with all these organizational tasks.

Thanks to all my colleagues at TFD and TD for a friendly work environment and support.

Last but not least, I would like to thank my mother and my wife. My mother did all to allow me to study at the university and do this Ph.D. My wife motivated me to make the last effort and, finally, to finish the thesis.

Contents

Nomenclature

Greek characters

α	thermal diffusivity ($\mathrm{kg/(ms)}$) or polynomial weighting coefficient
γ	heat-capacity ratio
Δ_i	acoustic displacement (m)
Δh°	standard enthalpy of reaction ($\mathrm{J/kg}$)
Δt	sampling time (s)
δ_{ij}	Kronecker delta
θ	phase (rad)
κ	thermal conductivity ($\mathrm{W/(mK)}$)
λ	wave length (m)
μ	dynamic viscosity ($\mathrm{kg/(ms)}$)
ξ	uncertain input parameter
π	number π
ρ	fluid density ($\mathrm{kg/m^3}$) or probability density function
τ	time delay of the n–τ model (s)
τ_{ij}	viscous stress tensor (Pa)
Ψ	multidimensional orthogonal polynomial
ψ	one-dimensional orthogonal polynomial
Ω	spatial region or uncertain input parameter space
$\dot{\omega}_k$	mass-specific reaction rate of species k ($\mathrm{1/s}$)
$\dot{\omega}_q$	mass-specific heat-release rate ($\mathrm{W/kg}$)

Latin characters

c	progress variable or speed of sound ($\mathrm{m/s}$)
c_p	heat capacity at constant pressure ($\mathrm{J/(kgK)}$)
D	mass diffusivity ($\mathrm{kg/(ms)}$)
E	expected value
$E(\,\vert\,)$	conditional expectation
$\mathscr{F}$	flame transfer function (FTF)
f	frequency (Hz)
h	sensible enthalpy ($\mathrm{J/kg}$)
He	Helmholtz number
I_{in}	acoustic wave intensity (Pa)

Im	imaginary part
$i,\ j,\ k,\ l$	indices
l_f	characteristic flame dimension (m)
Le	Lewis number
N	number of uncertain input parameters
n	gain of the n–τ model
P	total number of expansion terms
P_{in}	power of acoustic incoming waves (W)
P	Prandtl number
p	pressure (Pa) or one-dimensional polynomial-order bound
$\dot{Q}$	global heat release rate (W)
$\dot{q}$	local heat release rate (volume-specific, $\mathrm{W/m^3}$)
Re	real part
R	mass specific gas constant ($\mathrm{J/(kgK)}$)
RI	global Rayleigh index (W)
ri	local Rayleigh index (W)
S	Sobol index
Sc	Schmidt number
T	temperature (K)
t	time (s)
u	velocity (m/s)
Var	variance
W_k	molar mass of species k (kg/kmol)
$\dot{\omega}_k$	reaction rate of species k ($\mathrm{kg/(m^3 s)}$)
x_i	spatial coordinate i (m)
Y_k	mass fraction of species k
y	output quantity

Other symbols

$\overline{(\,)}$	mean or time-averaged quantity
$(\,)'$	fluctuating quantity
$\hat{(\,)}$	Laplace transformed quantity
$\widetilde{(\,)}$	LES filtered quantity
$[\,]^{tab}$	tabulated quantity

Abbreviations

BPDN	Basis Pursuit Denoising
CFD	computational fluid dynamics
DG-FEM	discontinuous Galerkin finite-element method
E-FLAME	Eulerian Flame Acoustic Motion Equation
FIR	finite impulse response
FTF	flame transfer function
LES	large-eddy simulation
LRF	linearized reactive flow
RI	Rayleigh index
SGS	subgrid scale
T1	first transverse mode
T2	second transverse mode
TNM	thermoacoustic network modeling
UQ	uncertainty quantification
ZS	Zellhuber & Schwing (model)

List of Figures

List of Tables

1 Introduction

1.1 Thermoacoustic analysis

Thermoacoustics studies a coupling between acoustics and heat release, see Fig. 1.1. This coupling may lead to a self-induced instability with excessive fluctuations in pressure, velocity, and temperature. Such instabilities occur, e.g. in gas turbines or rocket engines, where they can lead to a catastrophic system failure. To guarantee safety margins and normal operating conditions, a combustor's thermoacoustic behavior should be carefully analyzed. Indeed, a comprehensive thermoacoustic stability analysis should be an essential step in any combustor design. Despite increased efforts to explore non-linear aspects of combustion dynamics [56, 80, 94, 99], linear analysis remains extremely useful and important for fundamental studies of flow–flame interaction mechanisms, sensitivity or uncertainty analysis, optimization, and industrial applications. Therefore, this thesis focuses on linear stability analysis.

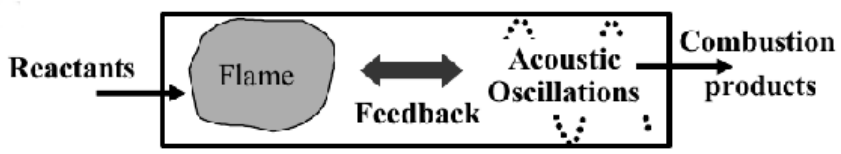

Figure 1.1: Schematic of thermoacoustic coupling (feedback). Reprinted from Lieuwen and Yang [66].

Usually, thermoacoustic instabilities are classified in low and high-frequency instabilities. The following two sections give an overview of both instabilities and different methods to model them.

1.2 Low-frequency instabilities

Low-frequency instabilities are longitudinal (or azimuthal) instabilities with acoustically compact flames. An acoustic Helmholtz number He_a defines flame compactness as a ratio between a characteristic flame dimension l_f and an acoustic wavelength λ_a:

$$He_a = 2\pi l_f / \lambda_a. \tag{1.1}$$

If the flame is compact ($He \ll 1$), the local perturbation of the flame front occurs at scales much smaller than the acoustic wave length. In this case the entire flame can be described by an integral quantity - the global heat release rate $\dot{Q}$. Typically, the fluctuation of the global heat-release rate $\dot{Q}'$ is related to the acoustic velocity fluctuation at a reference point upstream of the

flame u'_{ref} through a flame transfer function (FTF):

$$\frac{\dot{Q}'}{\overline{\dot{Q}}} = \mathscr{F}\frac{u'_{ref}}{\overline{u}_{ref}} \tag{1.2}$$

Typically, the flame transfer function is a superposition of several time-lagged responses of varying strength with distributed time delays [89, 102]. Following this idea, the simplest FTF is a single time-lagged response. This simple FTF is the $n-\tau$ model introduced by Crocco [26, 27]. More realistic flame response functions with several time delays are derived from experiments [59] or CFD simulations [8, 104, 105]. Considering discrete-time signals, the flame response can be expressed as a finite impulse response (FIR):

$$\frac{\dot{Q}'[l]}{\overline{\dot{Q}}} = \sum_{k=0}^{N-1} b_k \frac{u'_{ref}[l-k]}{\overline{u}_{ref}}, \tag{1.3}$$

where $[l]$ indicates the l-th discrete time step, b_k are the FIR coefficients. Given the sampling time Δt, the time delay between l-th and k-th steps is $(l-k)\,\Delta t$, and the length of FIR is $N\Delta t$. The finite impulse response can be z-transformed to the flame transfer function $\mathscr{F}$:

$$\mathscr{F}(s) = \sum_{k=0}^{N-1} b_k e^{-sk\Delta t}. \tag{1.4}$$

Note that this FTF is defined for a Laplace variable s, see for instance [32]. Nevertheless, for practical purposes, the FTF is typically evaluated for purely imaginary values s, which corresponds to the angular frequency $\dot{\omega}$ with zero growth-rate.

In experiments, the flame response is usually determined separately for each frequency, using a harmonic excitation signal. The same procedure can be applied in numerical simulations, but it results in a very significant computational effort. A more sophisticated method is to impose a broadband excitation, estimate the FIR from the time series applying a system identification technique [41, 88, 105], and convert the FIR to the FTF using Eqn. (1.4). This method requires only a single dynamic simulation.

The state-of-the-art technique to predict the combustor stability in a low-frequency regime is thermoacoustic network modeling (TNM) [31, 33, 88]. TNM is a low-order approach that represents a combustion system as a conjunction of elements, such as ducts and area jumps. Acoustic waves propagate through the resulting network of elements. The heat-release fluctuations are modeled using an FTF and produce acoustic perturbations according to the linearized Rankine–Hugoniot jump conditions [22]. TNM resolves acoustic plane waves, as well as non-plane higher order modes [34, 90]. The main advantage of TNM is robustness and high computational speed.

A more sophisticated method is the application of a Helmholtz solver with an FTF [79, 81, 99]. Helmholtz solver resolves acoustics in three dimensions and allows to study complex geometries but requires more computational resources than TNM. Helmholtz solver does not account for the mean flow effects, therefore it is extremely robust and does not require a fine mesh resolution to resolve dominant acoustic modes accurately.

The next step towards higher accuracy that can incorporate mean-flow effects and yield an accurate prediction of dissipative effects is applying the linearized Euler or linearized Navier-Stokes equations [67, 112]. An FTF models again the flame–acoustics interaction. Because of

the convective terms, this approach is very sensitive to the mesh resolution. The local flow changes (such as recirculation zones) must be well resolved to predict their dissipative effects accurately. All the methods mentioned above are *hybrid methods* since they couple a model for acoustic propagation and dissipation with an FTF, see Fig. 1.2

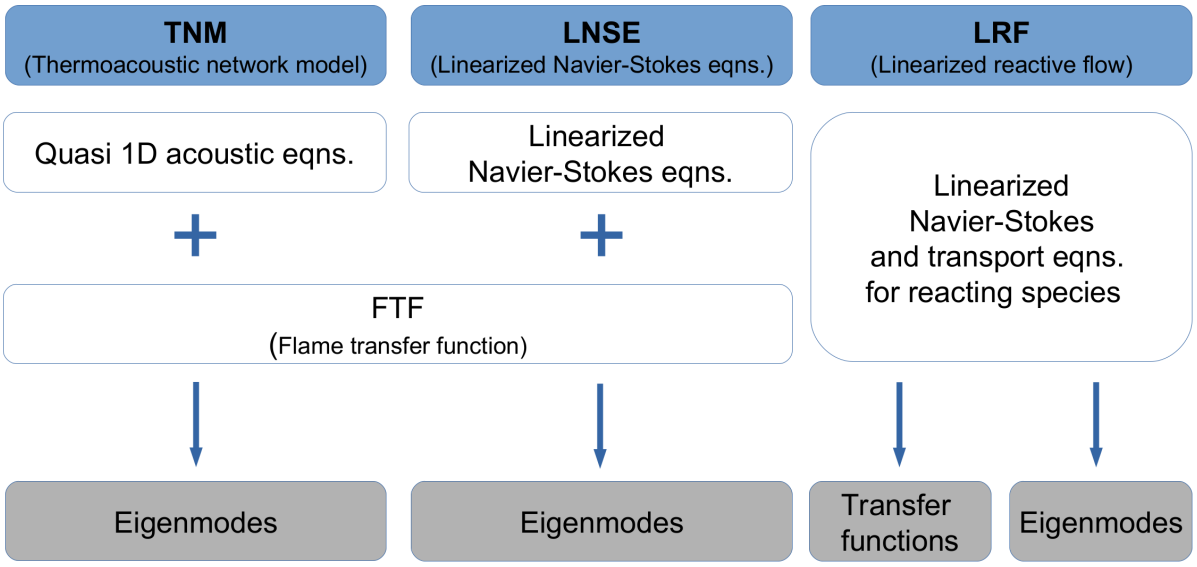

Figure 1.2: Schematic overview of the modeling methods for low-frequency stability analysis.

This thesis suggests another approach with an inherent description of the flame dynamics that is more accurate than the *hybrid methods*. This new approach is the *linearized reactive flow* (LRF). It is analytically derived by linearizing the Navier-Stokes and reacting species transport equations. Hence, the LRF is monolithic: the linear flame dynamics is by design inherited from the governing equations, the flame fluctuations are locally resolved, and an external FTF is not required. The LRF solver requires only a single CFD simulation to obtain mean fields, but no additional unsteady CFD simulations are needed to identify the FTF. The LRF is introduced in PAPER-LRF and successfully applied for thermoacoustic analysis of attached and lifted laminar premixed flames. The main aspects of the linearization procedure are revealed in Section 2.1, whereas the outcomes of PAPER-LRF are briefly summarized in Section 3.1. The reprint of PAPER-LRF is shown in Appendix 5. Recently, Meindl et al. [68] have shown, that a *hybrid method* coupled with a global FTF generates spurious entropy waves in the heat release zone, whereas the LRF approach shows no spurious entropy generation.

The works by van Kampen et al. [109] on the response of a premixed flame to equivalence-ratio fluctuations and by Blanchard et al. [17] on the effects of flow disturbances on the flame (and vice versa) may be regarded as precursors of the LRF approach. Those studies employ a numerical linearization of the governing equations and compute the FTF by simulating the step response in the time domain. The numerical linearization of the governing equations requires deep modifications of the CFD solver, which might be cumbersome or not possible at all. In contrast, the LRF equations are derived analytically, so this solver can be realized in a stand-alone application separately from the CFD solver. The LRF solver operates in the frequency domain[1],

[1]The LRF solver can also operate in the time domain and simulate the step response in time to derive the FTF, but it is more convenient and faster to work directly in the frequency domain.

which allows to compute the FTF and thermoacoustic eigenmodes. Furthermore, LRF offers flexibility in choosing plausible inputs and outputs, creating multiple-input and multiple-output systems. Thus, any transfer or scattering matrix of the system can be computed, for instance, a flame response to simultaneous excitations of the inlet velocity and equivalence-ratio, or the local flame transfer function. The ability of the LRF to resolve local flame fluctuations will be exploited at high frequencies, as shown in the following section.

1.3 High-frequency instabilities

In the high-frequency range, flames are acoustically non-compact, i.e. the characteristic flame length is of the same order as the acoustic wavelength or even higher ($He \gtrsim 1$). Typically, high-frequency instabilities are transverse instabilities[2] in rocket engines [28], ramjets, and afterburners [92], or in the second stage of sequential combustion systems (reheat combustors) [111]. This thesis investigates the high-frequency transverse instabilities in a generic reheat combustor.

While low-frequency instabilities are already well understood, the "high-frequency world" is still widely unexplored. The flame response mechanisms are not entirely understood, and until now, there is no established approach to model high-frequency instabilities. The non-compactness of the flame makes it difficult to model the flame–acoustics interaction. First, the flame response should be spatially resolved, so the FTF should be defined for the local heat-release rate $\dot{q}'$ instead of the global heat-release rate $\dot{Q}'$. Moreover, it is not clear what are the inputs of such a non-compact flame transfer function $\dot{q}' = f(?)$. Furthermore, experimental investigations of non-compact flames are complex and cost-intensive, so there are only few data sets for the model validation. Nevertheless, there are some solution strategies:

- Black-box approach: consider all possible inputs, e.g. pressure and velocity from the entire flow field, then use a special algorithm that fits a non-compact FTF and simultaneously minimizes the number of input parameters. One of such algorithms is Basis Pursuit Denoising (BPDN) [108]. In report COOREFLEX-Turbo 2.1.2c [6] BPDN has been applied to identify a global FTF of a premixed laminar flame. Unfortunately, BPDN has never been applied to any test case in the high-frequency regime due to the time constraints of the project COOREFLEX-Turbo 2.1.2c. Therefore, BPDN is out of the scope of this thesis. A detailed investigation of the method is required. Although BPDN can establish a relation between the local heat release rate and the flow field, it is not clear how to give a physical interpretation to such results.

- Coupling a Helmholtz solver with an $n-\tau$ model or another global FTF distributed over the entire flame region [40, 79]. The FTF can be tuned to fit the modal growth rates from experimental or simulation data.

  Nicoud et al. [79] studied azimuthal instabilities in annular combustors in the frequency domain. They considered two approaches: passive and active flame. A passive (or steady) flame results when the flame–acoustics coupling tends to zero, i.e. there is no fluctuation in the heat release rate. For an active flame approach, the authors applied an $n-\tau$

[2] Most of the azimuthal instabilities in annular combustors occur at high frequencies, but the flame usually remains compact. So these instabilities belong rather to the Section 1.2.

model. The time lag and interaction index were distributed locally and determined by post-processing LES results with a broadband longitudinal excitation. The reference velocity was taken at the injector mouth. The second approach accounts for the flame–acoustics interaction but is more computationally demanding. The active flame calculations showed that the effect of the flame-acoustic coupling on the stability is not obvious and can either stabilize or destabilize the system. Although the authors focused on azimuthal instabilities (i.e. compact flames), their active flame approach might be taken to model high-frequency flame response if applying a transverse excitation.

Ghani et al. [40] studied an unstable transverse acoustic mode in a swirled kerosene/air combustion chamber. The authors used an $n-\tau$ model with a single time lag and interaction index. They took the azimuthal acoustic velocity fluctuation at a point in the combustion chamber as a reference. The azimuthal velocity was chosen because it showed a higher correlation with the heat-release fluctuation than the streamwise velocity. The n and τ were determined from the LES of a self-excited oscillation. This combustion model allowed to recover the stability zones observed in the LES.

At first glace, the application of an $n-\tau$ model seems to be a fast and elegant solution, but this model is not universal. Until now there is no analytical approach how to obtain n and τ, so these parameters have to be determined separately for each load point.

- *Zellhuber-Schwing* (ZS) model: Schwing and Sattelmayer [96] experimentally investigated a transverse mode in a lab-scale swirl burner and suggested that the transverse flame displacement destabilizes the flame. Zellhuber et al. [114] formulated a corresponding mathematical model. The authors linearized the local heat-release rate neglecting the mean flow and using a frame, moving with the acoustic velocity. The linearized heat release is modulated due to the flame displacement (caused by acoustic velocity fluctuations), density fluctuations (caused by acoustic pressure fluctuations), and fluctuations in chemical consumption rates. The authors did not explicitly resolve the latter contribution. The ZS model can be coupled with a Helmholtz solver, the linearized Euler or Navier-Stokes equations but neglecting the mean flow.

  Berger et al. [12] performed another more extensive study of transverse instabilities in the swirl burner, previously used by Schwing and Sattelmayer [96]. The authors reconstructed the mean and fluctuating part of the heat-release rate in the burner midplane by means of dynamic pressure measurements and OH^* chemiluminescence imaging. Hummel et al. performed a numerical stability analysis of the same burner using a Helmholtz solver coupled with the ZS model in a joint publication [53]. The mean flow fields were deduced from the experimental measurements. The frequencies of self-induced oscillations were captured well by the thermoacoustic solver. The computed spatial distribution of the fluctuating heat-release rate was in qualitative agreement with the experimentally derived one. The driving force of the density fluctuation was roughly three times larger than the driving force of the flame displacement in this burner configuration. In the next publication [13], Berger et al. investigated the flame behavior at different levels of pulsation amplitudes. The unstable acoustic modes converged into a predominantly rotating character in the direction of the mean flow swirl. Pressure and heat-release rate fluctuations were in phase for all pulsation amplitudes. With increasing pulsation amplitudes, the driving force of the flame displacement becomes more important, than the driving force of the density fluctuation. Although the ZS model suggests a parameter-free model

for the flame displacement, the model derivation is cumbersome and might be flawed. Furthermore, the authors do not provide the explicit model for the consumption rate.

- *Eulerian Flame Acoustic Motion Equation* (E-FLAME): this model was derived by Méry, assuming that the flame motion does not produce a global fluctuation of the heat-release rate. By definition, this model addresses the flame motion only and always has a destabilizing effect. The E-FLAME model can also be coupled to the Helmholtz solver or any other linearized flow solver, neglecting the mean flow. In publication [70], Méry introduces the model and validates it in a one-dimensional configuration with a transversely excited flame. Besides that, a parametric study is performed in an acoustic network of an annular combustor. The superposition of two flame-acoustics coupling mechanisms was considered in this example: a simple $n-\tau$ model and the E-FLAME. At low frequencies, the global response of the compact flame ($n-\tau$ model) is much larger than the response to the flame motion. Nevertheless, the E-FLAME related growth rate increases at high frequencies, and if the transverse combustion dimension becomes smaller, the flame motion mechanism should not be neglected. The E-FLAME provides a parameter-free modeling of the flame movement as well as the SZ model. Section 2.1.6 compares both these models and answers which one is superior.

- Linearization of the reaction term from the governing equations: Sharifi et al. [97] investigated a generic turbulent propagating flame using an LES with a flame surface density approach. The authors excited the flame using transverse acoustic waves to obtain either a velocity or pressure node at the burner centerline and measured the global Rayleigh index. Then they linearized the combustion model and computed the contributions to the RI from each linearized term: density, laminar flame speed, subgrid wrinkling, and flame surface. This concept allowed to study how different heat-release mechanisms (i.e. linear fluctuations of each term in the flame model) affect flame stability. Although the authors did not create a reduced-order model for stability analysis using the linearized reaction term, their work supports this idea and motivates to use the LRF approach to investigate high-frequency instabilities.

As mentioned earlier, the SZ and E-FLAME models are parameter-free models, but they capture the flame motion only without reaction rate fluctuation. The LRF approach should close this gap, since it linearizes the full set of governing equations including the combustion model. Section 2.1 shows the derivation of the LRF model. Section 2.1.6 shows that after some simplifications, the LRF equations can be reduced to the E-FLAME model representing the acoustic flame motion. In Section 3.1, the LRF is successfully applied to a low-frequency response of a laminar flame. Section 3.2 is dedicated to the application of the LRF to the high-frequency flame resonse. Most of the previous numerical works on high-frequency transverse oscillations were focused on the dominant eigenmodes. The eigenfrequencies and growth rates were calculated with linear models at several burner load points. However, it is extremely difficult to extract the growth rates from experiments or LES data. Therefore, the quantitative comparison is not possible, and the results can only be classified as stable-neutral-unstable. This thesis suggests a different approach inspired by the works of Zellhuber et al. [114] and Sharifi et al. [97]. An autoignition flame in a generic reheat combustor is transversely excited, and the resulting Rayleigh index is calculated That allows a quantitative comparison between LES, LRF, E-FLAME and

ZS models. The Rayleigh index shows how much energy is supplied to the system per oscillation period T by combustion [78]:

$$RI = \int_\Omega ri \, dV = \int_\Omega \frac{1}{T} \int_0^T \frac{\overline{\gamma} - 1}{\overline{\gamma}\,\overline{p}} p' \dot{q}' \, dt \, dV, \tag{1.5}$$

where ri and RI are the local and global Rayleigh indices; $\int_\Omega dV$ and $\int_0^T dt$ are the integrals over the space and time; $\overline{\gamma}$ is the mean heat capacity ratio; $\overline{p}$ and p' are the mean and fluctuating parts of the pressure; q' is the fluctuating part of the volume-specific heat-release rate. Under the excitation, there is only one requirement that the burner remains stable. Thus the walls in the simulations are made non-reflecting. In general, this quantitative method to assess the driving force can be applied to experiments and other low-dimensional models. Unfortunately, the straightforward application of the full LRF model to the reheat combustor fails: the results do not agree at all with the CFD results. Hence, the remaining part of Section 3.2 is dedicated to the simplified LRF solver with the E-FLAME and ZS models. Finally, conclusion and outlook given in Section 3.2.4.

1.4 Uncertainty quantification in thermoacoustics

In real-life engineering applications, operating conditions and system parameters are not precisely known but are uncertain. These uncertainties propagate through the system and affect the prediction of the quantities of interest, making them uncertain.

In (linear) thermoacoustic analysis, the most important quantity of interest is the mode growth rate. Uncertainty quantification (UQ) analysis allows to predict the uncertainty of the growth rate and determine the *risk factor* – a probability of the system being unstable.

The most common and straightforward UQ method is the Monte Carlo simulation [72]. The simulation is performed in two steps. First, a set of uncertain input parameters, that follow a presumed distribution, is generated. Then, the quantity of interest is computed for each input sample. The resulting ensemble of realizations is used to characterize the uncertainty of the quantity of interest. Unfortunately, Monte Carlo simulation requires many realizations (typically several thousand) to obtain converged statistics. Therefore, it is feasible only if the computation time of the quantity of interest is at most in the order of minutes. The number of realizations can be somewhat reduced using a smart sampling technique, such as Latin hypercube sampling.

Nevertheless, if the computations are expensive (often in thermoacoustics), more sophisticated UQ methods are required. These methods reduce the original system to a low-order surrogate model that is cheap to evaluate and apply the Monte Carlo simulation on this surrogate model.

Bauerheim et al. [9] investigated a simplified annular combustor with 19 burners using a Helmholtz equation coupled with uncertain n-τ flame models. The authors applied an *active subspace* approach [25] reducing 38 input parameters to three active variables. Fifty samples, i.e. model evaluations, were required to identify the active variables. Linear and quadratic reduced-order algebraic models were fitted using a few dozen samples. Finally, a Monte Carlo simulation was performed on the reduced-order models to quantify the risk factor. The quadratic model showed accurate results in comparison to the original model. The active subspace ap-

proach is well suited for cases with a large number of uncertain parameters since it eliminates the *curse of dimensionality*. However, it works only if the input parameters can be combined to a few active variables, which is not always the case. Furthermore, the method requires several tens or even hundreds of system evaluations to identify the active variables and fit a surrogate model.

Guo et al. [44] followed the active subspace approach to investigate how the uncertainties from identifying the flame impulse response (FIR) affect the growth rate of thermoacoustic modes. The authors considered a turbulent swirled burner and identified the flame response coefficients with the corresponding uncertainties from a CFD simulation with a broadband excitation [103]. The active subspace approach computed the resulting uncertainties in the growth rate with the same accuracy as the reference Monte Carlo simulation, but 5000 times faster. Usually, the uncertainties in the FIR coefficients are reduced by taking a longer time series for the identification, i.e. prolonging the CFD simulation. The developed methodology can also serve as an indicator for terminating the CFD simulation [45].

Ndiaye et al. [76] investigated a single swirled burner, built at EM2C laboratory, using a Helmholtz equation coupled with the uncertain n-τ flame model. The authors applied a multiple linear regression technique to reduce the non-linear Helmholtz equation with two uncertain parameters to a bilinear algebraic model. Then, instead of the original system, the reduced model was used to compute the risk factor with a Monte Carlo simulation. A few dozen samples were enough to tune the reduced model.

Silva et al. [100] investigated the same swirled burner (EM2C) as Ndiaye et al [76], considering four uncertain parameters: n, τ, as well as the magnitude and the phase of the outlet reflection coefficient. Direct and adjoint eigenvectors were used to construct a first and second order expansions of the non-linear Helmholtz equation around a reference eigenvalue. Then applying a Monte Carlo simulation on these expansions, deviations from the reference eigenvalue were computed at a reduced computational cost. The second order expansion results were in good agreement with the results obtained by solving the non-linear Helmholtz equation.

The same strategy was applied by Mensah et al. [69], but the authors used a flame transfer function fitted from the experiment instead of a n–τ flame model. The uncertainty in the flame transfer function was modeled with two parameters, relative error in gain and absolute error in phase, which were assumed constant in the entire frequency range. The second order expansion sufficed to accurately determine the stability margins of the EM2C burner.

Recently, Guo et al. [46] suggested a machine learning method called *Gaussian process* to quantify the uncertainty of the dominant thermoacoustic modes in a swirled burner. The thermoacoustic modes of the burner were accessed using a low-order thermoacoustic network model (TNM) coupled with an FTF. The mode uncertainties were computed with a Monte Carlo simulation. The authors inspected six uncertain input parameters: the reflection coefficient at the burner outlet and the remaining five parameters described the FTF. The Gaussian process built a surrogate model that predicted the growth rate of the dominant modes faster than the TNM. One hundred training samples were needed to obtain good prediction quality. Besides that, the authors explored the fundamental aspects of the robust design in thermoacoustic instability analysis. In the following work [48], the authors applied the developed approach to approximate the Helmholtz solver. They performed UQ of the linear instability (growth rate) and non-linear

instability (amplitude of the limit cycle) in the EM2C burner. In paper [47], the authors studied how the imperfectly trained surrogate model affected the UQ of thermoacoustic instability. They suggested an active learning strategy further to enhance the efficiency of the GP model training. The latest work of these authors [49] indicated an extension of the GP – the multi-fidelity Gaussian process that combined the flame response identification from a short broadband excitation (low-fidelity) and harmonic excitations at few selected frequencies (high-fidelity). This approach allowed for improving the accuracy of the flame response identification even in the presence of strong noise.

This thesis presents a *nonintrusive polynomial chaos expansion* (NIPCE) for UQ and sensitivity analysis in thermoacoustics. NIPCE approximates the quantities of interest as a polynomial expansion of the uncertain input parameters. This method is particularly appealing in the industrial design process since it is easy to use and it treats the investigated system as a black box, so no modifications of the CFD solver are required. The method requires only a few samples to fit a low order polynomial. Hence it is perfectly suitable for problems with expensive system evaluations (such as high fidelity CFD simulations), but constrained to a small number of uncertain parameters. Besides uncertainties, the NIPCE provides a polynomial function for the quantity of interest that can be used as a reduced-order model, or for sensitivity analysis, computing derivatives with respect to the uncertain input parameters.

The NIPCE is an established approach, it has been applied frequently in computational fluid dynamics [50–52, 75, 107] and in simulations of reacting flows [91]. Despite the success in the CFD community, the NIPCE was applied in thermoacoustics only once by Nair et al. [74] to quantify the uncertainty of subcritical bifurcations predicted by a simplistic model of a Rijke tube. This thesis applies the NIPCE for UQ and sensitivity analysis for common thermoacoustic tasks.

Section 2.2 explains the basic methodology. PAPER-UQ-STABILITY (Section 4.1) propagates the uncertainties in operating conditions to the growth rate of the dominant thermoacoustic mode and performs a sensitivity analysis. Additionally, PAPER-UQ-FTF (section 4.2) propagates the uncertainties in operating conditions to the the flame transfer function and uses Sobol indices for the sensitivity analysis.

2 Methods

2.1 Linearized reactive flow

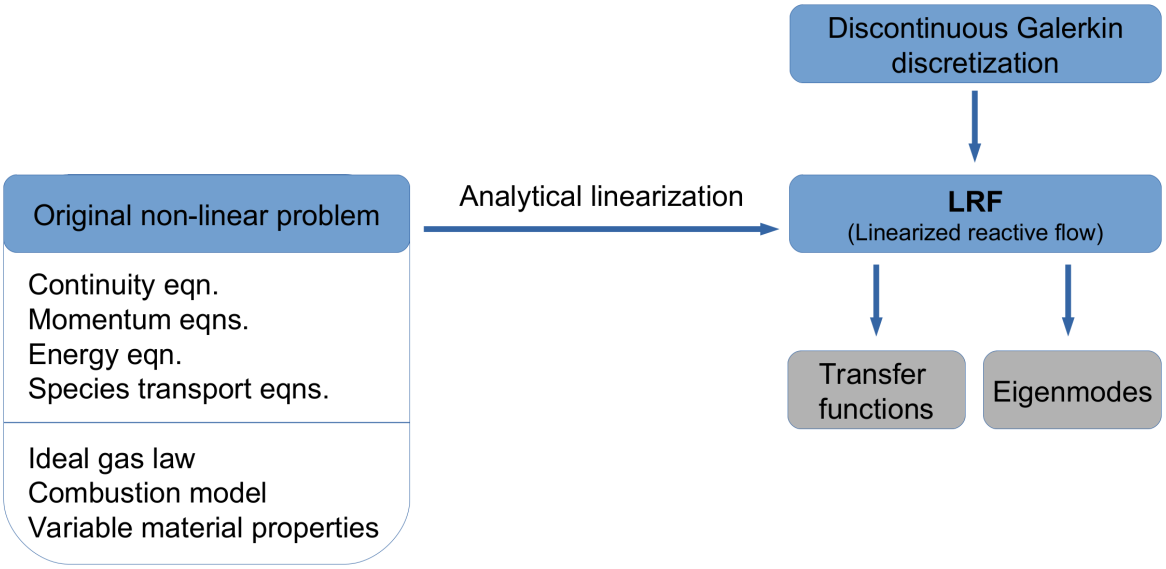

Figure 2.1: Schematic of the LRF approach and its features.

This chapter describes the LRF approach. Fig. 2.1 summarizes the LRF approach and its features. The non-linear governing equations are introduced (Section 2.1.1) and then, they are linearized (Section 2.1.2). The linearization of the combustion model is discussed in Section 2.1.3 followed by the turbulence treatment (Section 2.1.4) and the details on the numerical discretization of the LRF (Section 2.1.5).

Besides that, Section 2.1.6 compares the LRF, E-FLAME and ZS models with focus on the motion of acoustically non-compact flames at high frequencies.

2.1.1 Non-linear governing equations

At first, the non-linear governing equations should be defined. It is essential to linearize the very same governing equations that are used in the CFD solver for the computation of the mean fields. For instance, PAPER-LRF deploys an OpenFOAM solver with the inner energy equation

formulated for sensible enthalpy h. The set of reactive governing equations reads as

$$\frac{\partial \rho}{\partial t} + \frac{\partial \rho u_j}{\partial x_j} = 0, \tag{2.1}$$

$$\frac{\partial \rho u_i}{\partial t} + \frac{\partial \rho u_i u_j}{\partial x_j} = -\frac{\partial p}{\partial x_i} + \frac{\partial \tau_{ij}}{\partial x_j}, \tag{2.2}$$

$$\frac{\partial}{\partial t}\left(\rho h - p\right) + \frac{\partial \rho u_j h}{\partial x_j} = \frac{\partial}{\partial x_j}\left(\alpha \frac{\partial h}{\partial x_j}\right) + \dot{q}, \tag{2.3}$$

$$\frac{\partial \rho Y_k}{\partial t} + \frac{\partial \rho u_j Y_k}{\partial x_j} = \frac{\partial}{\partial x_j}\left(D \frac{\partial Y_k}{\partial x_j}\right) + \dot{w}_k. \tag{2.4}$$

Variables u_i and Y_k denote velocity component in the i-direction and mass fraction of the species k; $\partial/\partial t$ and $\partial/\partial x_i$ are temporal and spatial partial derivatives. The viscous term is neglected in equation for the sensible enthalpy h (2.3). The heat flux is approximated by $-\alpha\left(\partial h/\partial x_j\right)$ with thermal diffusivity α instead of Fourier's law. This heat-flux formulation is typical for OpenFOAM solvers and is deployed in PAPER-LRF. However, section 3.2 studies a turbulent auto-ignition flame with Ansys Fluent, where Fourier's law models the heat flux, so in that case $\frac{\partial}{\partial x_j}\left(\alpha \frac{\partial h}{\partial x_j}\right)$ is replaced by $\frac{\partial}{\partial x_j}\left(\kappa \frac{\partial T}{\partial x_j}\right)$ with thermal conductivity κ (W/(mK)).

The sensible enthalpy for the species k is calculated from JANAF polynomials with coefficients a_j:

$$h_k(T) = \int_{T_{ref}}^{T} c_{p,k} d\tilde{T} = R_k \sum_{j=1}^{5} a_j \frac{T^j - T_{\text{ref}}^j}{j}, \tag{2.5}$$

with the specific gas constant R_k for the species k. The sensible enthalpy of the mixture is computed using the species mass fractions: $h = \sum_k h_k Y_k$. The viscous stress tensor τ_{ij} reads:

$$\tau_{ij} = \mu\left(\frac{\partial u_i}{\partial x_j} + \frac{\partial u_j}{\partial x_i}\right) - \frac{2}{3}\mu \frac{\partial u_l}{\partial x_l}\delta_{ij}, \tag{2.6}$$

where δ_{ij} is the Kronecker delta. The ideal gas law links the pressure p, the density ρ, and the temperature T: $p = \rho R T$. The dynamic viscosity μ is given by Sutherland's law: $\mu = A_s T^{1/2}/\left(1 + T_S/T\right)$ with $A_s = 1.67212 \times 10^{-6}$ kg/(msK$^{1/2}$) and $T_S = 170.672$ K. To determine thermal diffusivity α, a constant Prandtl number $\mathrm{Pr} = \mu/\alpha = 0.71$ is assumed. Similarly, with unity Lewis number for all species, Schmidt number Sc and mass diffusivity D obey $\mathrm{Sc} = \mu/D = 0.71$. The reaction terms in the enthalpy equation $\dot{q}$ and species equations $\dot{w}_k$ are addressed in Section 2.1.3.

2.1.2 Linearized governing equations

Splitting field variables in Eqns. (2.1)–(2.4) into time-averaged and first-order fluctuating parts (indicated by the overline and the prime) $\phi = \overline{\phi} + \phi'$ yields the lineazied equations:

$$\frac{\partial \rho'}{\partial t} + \frac{\partial}{\partial x_j}\left(\overline{\rho} u_j' + \rho' \overline{u}_j\right) = 0, \tag{2.7}$$

$$\frac{\partial}{\partial t}\left(\overline{\rho} u_i' + \rho' \overline{u}_i\right) + \frac{\partial}{\partial x_j}\left(\overline{\rho u}_i u_j' + \overline{\rho} u_i' \overline{u}_j + \rho' \overline{u}_i \overline{u}_j\right) = -\frac{\partial p'}{\partial x_i} + \frac{\partial \tau_{ij}'}{\partial x_j}, \tag{2.8}$$

$$\frac{\partial}{\partial t}\left(\overline{\rho} h' + \rho' \overline{h} - p'\right) + \frac{\partial}{\partial x_j}\left(\overline{\rho u}_j h' + \overline{\rho} u_j' \overline{h} + \rho' \overline{u}_j \overline{h}\right) = \frac{\partial}{\partial x_j}\left(\overline{\alpha}\frac{\partial h'}{\partial x_j} + \alpha' \frac{\partial \overline{h}}{\partial x_j}\right) + \dot{q}', \tag{2.9}$$

$$\frac{\partial}{\partial t}\left(\overline{\rho} Y_k' + \rho' \overline{Y}_k\right) + \frac{\partial}{\partial x_j}\left(\overline{\rho u}_j Y_k' + \overline{\rho} u_j' \overline{Y}_k + \rho' \overline{u}_j \overline{Y}_k\right) = \frac{\partial}{\partial x_j}\left(\overline{D}\frac{\partial Y_k'}{\partial x_j} + D' \frac{\partial \overline{Y}_k}{\partial x_j}\right) + \dot{\mathfrak{w}}_k', \tag{2.10}$$

where the viscous stress tensor, dynamic viscosity, sensible enthalpy, and ideal gas law are linearized to

$$\tau_{ij}' = -\frac{2}{3}\delta_{ij}\left(\overline{\mu}\frac{\partial u_l'}{\partial x_l} + \mu' \frac{\partial \overline{u}_l}{\partial x_l}\right) + \overline{\mu}\left(\frac{\partial u_i'}{\partial x_j} + \frac{\partial u_j'}{\partial x_i}\right) + \mu'\left(\frac{\partial \overline{u}_i}{\partial x_j} + \frac{\partial \overline{u}_j}{\partial x_i}\right), \tag{2.11}$$

$$\mu' = \overline{\mu}\frac{\overline{T} + 3T_S}{2(\overline{T} + T_S)}\frac{T'}{\overline{T}}, \tag{2.12}$$

$$\tag{2.13}$$

$$h' = \overline{c}_p T' + \sum_k \overline{h}_k Y_k', \tag{2.14}$$

$$\frac{T'}{\overline{T}} = \frac{\rho'}{\overline{\rho}} - \frac{p'}{\overline{p}} \tag{2.15}$$

D' and α' are computed analogously. Note that the enthalpy equation cannot be reduced to the pressure equation because c_p is not constant, see Eqns. (2.5) and (2.14). The linearization of the reaction terms $\dot{q}'$ and $\dot{\mathfrak{w}}_k'$ is shown in Section 2.1.3.

The derived set of equations shows that LRF accounts for the mean-flow effects, allows propagation of acoustic, vorticity, and entropy waves, as well as a linear energy transfer between them. The linearized state variables are p', ρ', u_i' and Y_k', where the number of transported species depends on the reaction modeling (see Section 2.1.3). For the sake of compactness, we avoid rewriting the linearized Eqs. (2.7)–(2.10) in terms of the selected linearized variables, it can be done without essential difficulty using the expressions provided in Eqns (2.11)–(2.15).

In closing this section, it is emphasized that the first-order fluctuations of material properties are retained to make the linearized equations fully consistent with the original non-linear problem. PAPER-LRF shows that it is crucial to obtain the correct flame response of laminar flames.

2.1.3 Reaction term

This thesis pursues the approach of linearization of reaction kinetics. Alternatively, other approaches, such as the linearization of the G-equation [2, 3, 21, 98], are also feasible.

2.1.3.1 One-step irreversible reaction

Following [87], the progress rate of a typical one-step irreversible reaction $\mathscr{Q}$ for the methane-air combustion is defined as

$$\mathscr{Q} = A\rho^{a+b} \frac{Y_{O_2}^a Y_{CH_4}^b}{W_{O_2}^a W_{CH_4}^b} \exp\left(-\frac{E_a}{TR_{\text{univ}}}\right). \tag{2.16}$$

PAPER-LRF uses the reaction coefficients A, a, b from one-step Westbrook and Dryer [110] chemistry mechanism. Note that this mechanism is taken just for proof of concept, but it is entirely outdated and thus not recommended in general.

The methane/air consumption rates and the heat-release rate[1] are

$$\dot{\mathfrak{w}}_{\mathrm{CH_4}} = -W_{\mathrm{CH_4}}\mathscr{Q}, \tag{2.17}$$

$$\dot{\mathfrak{w}}_{\mathrm{O_2}} = -W_{\mathrm{O_2}}\mathscr{Q}, \tag{2.18}$$

$$\dot{q} = \Delta h^\circ \mathscr{Q}, \tag{2.19}$$

where $W_{\mathrm{CH_4}}$ and $W_{\mathrm{O_2}}$ are the molar masses of methane and air; Δh° is the standard enthalpy of reaction. The linearized consumption rate of species $k = \{\mathrm{CH_4}, \mathrm{O_2}\}$ reads

$$\dot{\mathfrak{w}}'_k = \overline{\dot{\mathfrak{w}}}_k \left((a+b)\frac{\rho'}{\overline{\rho}} + \frac{T_a T'}{\overline{T}^2} + a\frac{Y'_{\mathrm{O_2}}}{\overline{Y}_{\mathrm{O_2}}} + b\frac{Y'_{\mathrm{CH_4}}}{\overline{Y}_{\mathrm{CH_4}}} \right); \tag{2.20}$$

$\dot{q}'$ is computed in the same manner.

PAPER-LRF investigates a case of premixed combustion, so the equivalence ratio does not vary. It is enough to include a single species transport equation, for instance CH4, in the set of linearized governing equations (2.7)–(2.10). Then, the fluctuation of the air mass fraction is given by

$$Y'_{O_2} = (2W_{\mathrm{O_2}}/W_{\mathrm{CH_4}})Y'_{\mathrm{CH_4}}. \tag{2.21}$$

The mean mass fractions $\overline{Y}_{\mathrm{CH_4}}$ and $\overline{Y}_{\mathrm{O_2}}$ appear in the denominator of Eqn. (2.20), so they should be limited to some small numbers when they go to zero avoiding numerical problems.

This concept of the linearized one-step irreversible reaction can be easily extended to model additional perturbations in the equivalence ratio, as shown by M. Kühn in his term paper [61], supervised by the present author. The extension introduces an additional transport equation for $\mathrm{O_2}$ and modifies the linearized ideal gas law since the specific gas constant R depends on the equivalence-ratio fluctuations.

2.1.3.2 Multi-step reaction

PAPER-LRF applies a one-step mechanism for the sake of simplicity. However, one-step mechanisms are inaccurate, so the reaction is usually approximated using a multi-step chemical

[1] Note that PAPER-LRF uses a slightly different notation for the heat-release rate ($\mathsf{W/m^3}$) and species reaction rate ($\mathsf{kg/(sm^3)}$) – $\dot{\omega}_q$ and $\dot{\omega}_k$. This thesis uses the notation $\dot{q}$ and $\dot{\mathfrak{w}}$, respectively.

mechanism. The current state of the art refers to the application of a two-step reaction mechanism at least, such as 2S-CM2 [15]. The linearization of a multi-step reduced mechanism might be a tedious task, but it is still straightforward. The linearized 2S-CM2 mechanism was recently applied by Meindl et al. [68] in the framework of the LRF approach.

2.1.3.3 Tabulation of the progress variable

Instead of adding more and more steps to the reaction mechanism in order to achieve higher accuracy at the cost of increased complexity, it is also possible to use a tabulated chemistry approach. This approach is often used in turbulent combustion and is usually combined with the laminar flamelet concept [83], which applies to a regime where the chemical time-scales are shorter than the turbulent ones. In this regime, a turbulent flame can be approximated as an ensemble of laminar flamelets. Exploiting this concept, turbulent combustion models compute the thermochemical states of flamelets in a pre-processing step (before the CFD simulation) and store them in a look-up table in dependence of progress variable Y_c, mixture fraction, etc. [11, 18, 29]. A specialized chemical kinetics solver generates this look-up table. Depending on the combustion type and regime, the solver uses either perfectly stirred reactors for auto-ignition flames [19, 30, 62–64], one-dimensional propagating flamelets for (partially) premixed flames [18, 30, 36–38, 85], or counter-flow flamelets for premixed or diffusion flames [11, 54, 57, 58, 93, 106, 115].

The tabulated chemistry was coupled with the stochastic-fields approach to model the turbulent combustion of auto-ignition flames by Kulkarni et al. [62–64]. This methodology is applied in Section 3.2 for large-eddy simulations of an adiabatic premixed auto-ignition stabilized flame in a generic reheat combustor. For this case, the LRF solver is built by linearizing the same combustion model as in the LES to preserve consistency.

This section illustrates the details of the tabulation and linearization of the combustion look-up table. For the sake of simplicity, the heat loss effects are neglected in the reheat combustor under investigation, so the tabulation has only one dimension (progress variable Y_c). However, the linearization approach can be easily extended to account for several tabulation dimensions.

For the auto-ignition of a methane-air mixture [62], the progress variable Y_c is defined as

$$Y_c = Y_{CH_2O} + Y_{CO} + Y_{CO_2}. \tag{2.22}$$

The chemical look-up table provides the mass-specific source term $[\dot{\omega}_c]^{tab}_{Y_c}$ for the progress variable equation and the mass fractions for the transported species $[Y_k]^{tab}_{Y_c}$ in the LES. The square brackets with superscript ^{tab} in expression $[Y_k]^{tab}_{Y_c}$ refers to the tabulated quantity of a transported species in this case, and the subscript $_{Y_c}$ refers to the interpolation of the tabulated quantity at a given value of the progress variable. The reaction rate for the progress variable in the LES is split in density and the mass-specific source term for the progress variable, thereby the latter term comes from the look-up table:

$$\widetilde{\dot{\omega}}_c = \widetilde{\rho}\widetilde{\dot{\omega}}_c \approx \widetilde{\rho}\,[\dot{\omega}_c]^{tab}_{\widetilde{Y}_c}, \tag{2.23}$$

where $\widetilde{(\,)}$ denotes filtered LES fields. The reaction rates for the transported species in the LES

can be computed in the same way:

$$\widetilde{\dot{\mathfrak{w}}}_k = \widetilde{\rho}\widetilde{\dot{\omega}}_k \approx \widetilde{\rho}\,[\dot{\omega}_k]^{tab}_{\widetilde{Y}_c}. \tag{2.24}$$

However, the direct application of the term $[\dot{\omega}_k]^{tab}_{\widetilde{Y}_c}$ in LES produces high numerical errors according to [73, 82]. Hence, a reconstruction of the reaction rates using the tabulated mass fractions is applied:

$$\widetilde{\dot{\mathfrak{w}}}_k \approx \widetilde{\rho}\frac{[Y_k]^{tab}_{\widetilde{Y}_c} - \widetilde{Y}_k}{\Delta t_{LES}}, \tag{2.25}$$

where Δt_{LES} is the time-step size in the LES. The reaction term in the enthalpy equation is computed in a similar manner using the enthalpy of formation h°_k of each transported species:

$$\widetilde{\dot{q}} = \widetilde{\rho}\widetilde{\dot{\omega}}_q \approx -\widetilde{\rho}\frac{\sum_k \left([Y_k]^{tab}_{\widetilde{Y}_c} - \widetilde{Y}_k\right) h^\circ_k}{\Delta t_{LES}}. \tag{2.26}$$

Now to build a linear model, the tabulated combustion approach is linearized. The linearization of Eqn. (2.24) yields the linear fluctuation of the progress variable:

$$\dot{\mathfrak{w}}'_c = \overline{\dot{\omega}}_c\rho' + \overline{\rho}\dot{\omega}'_c \approx \overline{\dot{\omega}}_c\rho' + \overline{\rho}\left[\frac{d\dot{\omega}_c}{dY_c}\right]^{tab}_{\overline{Y}_c} Y'_c, \tag{2.27}$$

where $\overline{(\,)}$ denotes a time-averaged LES field. So $\dot{\mathfrak{w}}'_c$ depends on the fluctuations of the density and the progress variable, where $[d\dot{\omega}_c/dY_c]^{tab}$ comes from the combustion tabulation. Due to adiabatic fully-premixed combustion, there is only one tabulation dimension (Y_c), hence $[\dot{\omega}_c]^{tab}$ depends solely on Y_c. In a more complex case, there will be several partial derivatives of $[\dot{\omega}_c]^{tab}$ in Eqn. (2.27).

The linearized heat-release rate reads as

$$\dot{q}' = \overline{\dot{\omega}}_q\rho' + \overline{\rho}\dot{\omega}'_q \approx \overline{\dot{\omega}}_q\rho' + \overline{\rho}\left[\frac{d\dot{\omega}_q}{dY_c}\right]^{tab}_{\overline{Y}_c} Y'_c, \tag{2.28}$$

where $\dot{\omega}_q$ is the mass-specific heat-release rate (W/kg) and $\left[d\dot{\omega}_q/dY_c\right]^{tab}$ is its tabulated derivative with respect to the progress variable[2].

Applying the combustion tabulation to the LRF approach replaces the species transport equations (2.10) by a single transport equation for the progress variable with the source term given by Eqn. (2.27). The source term for the enthalpy equation (2.9) is given by Eqn. (2.28), respectively.

2.1.4 Turbulence modeling

There is currently no model that directly accounts for turbulence – combustion interactions in the linearized concept. These interactions are taken into account indirectly via mean fields since

[2] If the tabulation yields only $[\dot{\omega}_c]^{tab}$ and $[Y_k]^{tab}$, then $[d\dot{\omega}_c/dY_c]^{tab}$ and $\left[d\dot{\omega}_q/dY_c\right]^{tab}$ can be easily derived using finite differences and the knowledge of formation enthalpy of transported species.

they smear out shear layers and flame fronts. Additionally, turbulence contributes to the energy dissipation in the LRF by a turbulent viscosity that is added to the molecular viscosity [42]:

$$\mu_{eff} = \mu + \mu_{turb}. \tag{2.29}$$

The same approximation applies for the thermal conductivity $\kappa_{eff} = \kappa + \kappa_{turb}$ and the mass diffusivity $D_{eff} = D + D_{turb}$. In Section 3.2 that investigates a turbulent flame, the LRF solver takes the mean fields from the LES, so the turbulent viscosity in the LRF is set to the time-averaged subgrid-scale viscosity $\mu_{turb} = \overline{\mu}_{SGS}$. Similarly, $\kappa_{turb} = \overline{\kappa}_{SGS}$ and $D_{turb} = \overline{D}_{SGS}$.

2.1.5 Discretization

In PAPER-LRF and Section 3.2, the LRF equations are discretized using the discontinuous Galerkin finite-element method (DG-FEM) with a local Lax-Friedrichs flux formulation [23]. This method is chosen because it is an established method in CFD and is robust for convection-dominated problems [24]. DG-FEM was only recently adopted for a hybrid thermoacoustic solver [67]. The discretization with linear weighting functions for all linearized variables is implemented in the commercial software COMSOL Multiphysics. The mean fields are provided either by OpenFOAM simulations (PAPER-LRF), or Ansys Fluent (Section 3.2). The derivatives of the mean fields, such as $\partial\overline{u}_i/\partial x_j$, $\partial\overline{Y}_{\mathrm{CH_4}}/\partial x_j$, and $\partial\overline{h}/\partial x_j$, are computed by the LRF solver in COMSOL Multiphysic internally.

The LRF solver computes the flame response in the frequency domain. Alternatively, the flame response may be deduced from a step response or broadband excitation in the time domain [88, 105]. That will lower RAM requirements, but the computational time will significantly rise.

The eigenvalues are computed with an implicitly restarted Arnoldi algorithm [65], which is a default algorithm in COMSOL Multiphysics. Parallelization of computations is achieved using the direct parallel solver MUMPS [4].

2.1.6 Flame modeling of acoustically non-compact flames

This section compares the LRF, ZS, and E-FLAME models focusing on the motion of acoustically non-compact flames at high frequencies. The first model contains the linear flame dynamics inherited directly from the linearization of the non-linear governing equations. Whereas the two latter models describe only the linear flame dynamics, so these models should first be coupled with a linearized flow solver.

The ZS model was developed by Zellhuber and Schwing [114] for the local fluctuation of the heat-release rate (volume-specific), reads as

$$\dot{q}' = \overline{\dot{q}}\frac{\rho'}{\overline{\rho}} - \frac{\partial\overline{\dot{q}}}{\partial x_i}\Delta_i' + \overline{\dot{q}}\frac{\dot{\omega}_q'}{\overline{\dot{\omega}}_q}, \tag{2.30}$$

where Δ_i' is the acoustic displacement. The first term in Eqn. (2.30) is the density sensitivity. Assuming the isentropic flow, the density fluctuations can be replaced by the pressure fluctua-

tions:

$$p' = \overline{c}^2 \rho' \quad \longrightarrow \quad \frac{\rho'}{\overline{\rho}} = \frac{1}{\gamma}\frac{p'}{\overline{p}}. \tag{2.31}$$

Berger et al. [12, 13, 53, 95] qualify the density-sensitivity term as the flame compression (expansion). The second term in Eqn. (2.30) is the sensitivity to the acoustic flame displacement[3]. This term is derived in the original study using a concept of a moving frame that is quite cumbersome. The third term in Eqn. (2.30) is the fluctuation of the mass-specific reaction rate $\dot{\omega}'_q$, which comes from chemistry. Eqn. (2.30) cannot be coupled directly to a linear flow solver, since it includes the time integral of the fluctuating velocity field (Δ'_i). Taking time derivative solves the problem and yields an equation for the temporal evolution of the fluctuating local heat-release rate:

$$\frac{\partial \dot{q}'}{\partial t} = \frac{\overline{\dot{q}}}{\overline{\rho}}\frac{\partial \rho'}{\partial t} - \frac{\partial \overline{\dot{q}}}{\partial x_i}u'_i + \frac{\overline{\dot{q}}}{\overline{\dot{\omega}}_q}\frac{\partial \dot{\omega}'_q}{\partial t}. \tag{2.32}$$

Zellhuber and Schwing do not provide an explicit expression for ω'_q, so it is neglected, as it was done in all previous applications of the ZS model:

$$\frac{\partial \dot{q}'}{\partial t} = \frac{\overline{\dot{q}}}{\overline{\rho}}\frac{\partial \rho'}{\partial t} - \frac{\partial \overline{\dot{q}}}{\partial x_i}u'_i. \tag{2.33}$$

The above equation is used in the numerical realization of the ZS model in Section 3.2.

For a better comparison to the E-FLAME and LRF models, Eqn. (2.33) is rewritten using the relation $\dot{q} = \rho\dot{\omega}_q$, the linearized continuity equation with no mean flow $\partial\rho'/\partial t = -\partial(\overline{\rho}u'_i)/\partial x_i$, and then applying the chain rule:

$$\frac{\partial \dot{q}'}{\partial t} = -\overline{\dot{\omega}}_q\frac{\partial(\overline{\rho}u'_i)}{\partial x_i} - \frac{\partial \overline{\rho}\overline{\dot{\omega}}_q}{\partial x_i}u'_i = -\overline{\dot{\omega}}_q\overline{\rho}\frac{\partial u'_i}{\partial x_i} - \overline{\dot{\omega}}_q u'_i\frac{\partial \overline{\rho}}{\partial x_i} - \frac{\partial \overline{\rho}\overline{\dot{\omega}}_q}{\partial x_i}u'_i = -\frac{\partial(\overline{\dot{q}}u'_i)}{\partial x_i} - \overline{\dot{\omega}}_q u'_i\frac{\partial \overline{\rho}}{\partial x_i}. \tag{2.34}$$

Another concept – the Eulerian Flame Acoustic Motion Equation (E-FLAME) – was suggested by Méry [70, 71] to model the linear motion of a non-compact flame at high frequencies. Méry assumes that convective effects are negligible at high frequencies, and the flame strictly follows the acoustic velocity only. While moving, the flame does not produce a fluctuation of the global heat-release rate, so the E-FLAME is a conservation equation for the linearized heat-release rate:

$$\frac{\partial \dot{q}'}{\partial t} = -\frac{\partial(\overline{\dot{q}}u'_i)}{\partial x_i}. \tag{2.35}$$

Using the divergence theorem, it can be shown that $\int_\Omega \dot{q}'\,dV = 0$. Furthermore, as shown in [70], Eqn. (2.35) always yields a positive RI, so the flame motion always increases the growth rate of the acoustic energy. The E-FLAME model, as well as the ZS model, can be coupled to any linearized flow solver without the mean flow. Comparing Eqns. (2.34) and (2.35), one can see that the ZS and E-FLAME models differ by one term $-u'_i\overline{\dot{\omega}}_q\left(\partial\overline{\rho}/\partial x_i\right)$. Obviously, this term is non-negligible since the mean density changes across the flame. Due to this term, the ZS model

[3] Strictly following the work of Zellhuber et al. [114], the term $-\left(\partial\overline{\dot{q}}(x)/\partial x_i\right)\Delta'_i$ is valid for the acoustic displacement only, so the ZS model can be coupled only with a linearized flow solver neglecting the mean flow ($\overline{u} = 0$).

does not always yield a positive RI in contrast to the E-FLAME model, as it will be shown later in Section 3.2.3.

In the following, the LRF is compared to the ZS and E-FLAME models. A time-derivative of the linearized heat-release rate from the LRF model (2.28) yields:

$$\frac{\partial \dot{q}'}{\partial t} = \overline{\dot{\omega}}_q \frac{\partial \rho'}{\partial t} + \overline{\rho} \left[\frac{d\dot{\omega}_q}{dY_c} \right]_{\overline{Y}_c}^{tab} \frac{\partial Y_c'}{\partial t}. \tag{2.36}$$

The conservation equation for the progress variable without mean flow and diffusion reads as

$$\overline{\rho} \frac{\partial Y_c'}{\partial t} + \overline{\rho} u_i' \frac{\partial \overline{Y}_c}{\partial x_i} = \overline{\dot{\omega}}_c \rho' + \overline{\rho} \left[\frac{d\dot{\omega}_c}{dY_c} \right]_{\overline{Y}_c}^{tab} Y_c'. \tag{2.37}$$

Inserting Eqn. (2.37) into Eqn. (2.36), applying the linearized continuity equation and the substitution $\left[\frac{d\dot{\omega}_q}{dY_c} \right]_{\overline{Y}_c}^{tab} \frac{\partial \overline{Y}_c}{\partial x_i} = \frac{\partial \overline{\dot{\omega}}_q}{\partial x_i}$ yields

$$\begin{aligned} \frac{\partial \dot{q}'}{\partial t} &= -\overline{\dot{\omega}}_q \frac{\partial (\overline{\rho} u_i')}{\partial x_i} + \overline{\rho} \left[\frac{d\dot{\omega}_q}{dY_c} \right]_{\overline{Y}_c}^{tab} \left(-u_i' \frac{\partial \overline{Y}_c}{\partial x_i} + \overline{\dot{\omega}}_c \frac{\rho'}{\overline{\rho}} + \left[\frac{d\dot{\omega}_c}{dY_c} \right]_{\overline{Y}_c}^{tab} Y_c' \right) \\ &= -\frac{\partial (\overline{\dot{q}} u_i')}{\partial x_i} + \underbrace{\left(\overline{\dot{\omega}}_c \left[\frac{d\dot{\omega}_c}{dY_c} \right]_{\overline{Y}_c}^{tab} \rho' + \overline{\rho} \left[\frac{d\dot{\omega}_q}{dY_c} \right]_{\overline{Y}_c}^{tab} \left[\frac{d\dot{\omega}_c}{dY_c} \right]_{\overline{Y}_c}^{tab} Y_c' \right)}_{\left[\frac{d\dot{\omega}_c}{dY_c} \right]_{\overline{Y}_c}^{tab} \dot{\mathfrak{w}}_c'} \end{aligned} \tag{2.38}$$

The first term in the above equation is the convection of the heat-release rate, and the remaining part in the parenthesis is the source term that comes from the reaction-rate fluctuations of the progress variable $\dot{\mathfrak{w}}_c'$. Assuming no fluctuations of the reaction rate ($\dot{\mathfrak{w}}_c' = 0$) leads to the transport equation for the heat-release rate, i.e. to the pure flame motion[4]. So the LRF model reproduces exactly the E-FLAME model. In his work, Méry postulated the transport equation for the heat-release rate. This thesis derives this equation from the full set of linearized equations, shows all assumptions that should be made and encourages the application of E-FLAME model if $\dot{\mathfrak{w}}_c'$ cannot be modeled. Another significant result is the following: the above derivation suggests that the ZS model (with an arguable derivation using a moving frame) has a flaw. The ZS model obviously does not reproduce the pure flame motion because of the additional term $-u_i' \overline{\dot{\omega}}_q \left(\partial \overline{\rho} / \partial x_i \right)$, see Eqn. (2.34). Besides, if the tabulated approach was used to resolve the fluctuation of the mass-specific heat-release rate $\dot{\omega}_q'$ in Eqn. (2.32), then this would result in Eqn. (2.38), but again with the superfluous term $-u_i' \overline{\dot{\omega}}_q \left(\partial \overline{\rho} / \partial x_i \right)$.

2.2 Non-intrusive polynomial chaos expansion

2.2.1 Uncertainty quantification

The NIPCE is extensively documented and implemented in several open-source software packages [1, 5, 35]. This thesis briefly summarizes the methodology in the same way as in

[4] As shown in PAPER-LRF, the LRF model even captures the convected linear flame motion when the mean flow effects are included in the modeling, e.g. convected flame wrinkles)

Distribution	Probability density function	Polynomial	Support range
Normal	$\frac{1}{\sqrt{2\pi}} e^{-\xi_i^2/2}$	Hermite	$[-\infty, \infty]$
Uniform	$1/2$	Legendre	$[-1, 1]$
Beta	$\frac{(1-\xi_i)^\alpha (1+\xi_i)^\beta}{2^{\alpha+\beta+1} B(\alpha+1, \beta+1)}$	Jacobi	$[-1, 1]$
Exponential	$e^{-\xi_i}$	Laguerre	$[0, \infty]$
Gamma	$\frac{\xi_i^\alpha e^{-\xi_i}}{\Gamma(\alpha+1)}$	Generalized Laguerre	$[0, \infty]$

Table 2.1: Most common probability distribution types and corresponding optimal polynomial types [1].

PAPER-UQ-STABILITY and PAPER-UQ-FTF.

The NIPCE approximates an output quantity y as a truncated sum of multidimensional orthogonal polynomials Ψ_i of a number N of uncertain input parameters $\xi = [\xi_1, \xi_2, ..., \xi_N]$:

$$y \cong \sum_{i=0}^{P-1} \alpha_i \Psi_i(\xi), \tag{2.39}$$

where α_i are the weighting coefficients and P is the total number of expansion terms. The uncertain input parameters ξ are uncorrelated and standardized. If the uncertain input parameters are correlated, then they should be transformed into fewer independent variables. The multidimensional polynomials $\Psi_i(\xi)$ are constructed using a tensor-product expansion of one-dimensional polynomials $\psi(\xi_j)$, i.e. the are are permutations of one-dimensional polynomials in all parameter dimensions. In this case, the total number of expansion terms is constrained by the one-dimensional polynomial-order bounds p_j for the j-th uncertain input parameter:

$$P = \prod_{j=1}^{N} (p_j + 1). \tag{2.40}$$

The above-mentioned tensor-product expansion supports anisotropy. Hence, the polynomial-order bounds p_j can be chosen independently for each uncertain parameter ξ_j. PAPER-UQ-STABILITY and PAPER-UQ-FTF considered the same polynomial-order bounds for all uncertain input parameters, but it is not mandatory. For instance, starting with a linear polynomial ($p_j = 1$ for all uncertain parameters), the order of each input parameter can be increased iteratively one by one. This iterative process allows identifying the most dominant uncertain parameters and increasing only the polynomial order of these parameters.

The choice of the one-dimensional polynomial $\psi(\xi_j)$ depends on the probability distribution of the uncertain input parameter ξ_j. Each probability distribution type has its optimal polynomial type, as listed in [1]. Each ξ_j can follow its particular distribution. The most common one-dimensional orthogonal polynomials are listed in Tab. 2.1. Once the distribution type and p_j are chosen for each ξ_j, the corresponding one-dimensional polynomials $\psi(\xi_j)$ can be constructed up to the order p_j; then the multidimensional polynomials are the permutations of all one-dimensional polynomials in the entire parameter space ξ:

$$\Psi_{0,0,...,0}(\xi_1,\xi_2,...,\xi_N) = \psi_0(\xi_1)\,\psi_0(\xi_2)\cdot...\cdot\psi_0(\xi_N), \tag{2.41}$$

$$\Psi_{1,0,...,0}(\xi_1,\xi_2,...,\xi_N) = \psi_1(\xi_1)\,\psi_0(\xi_2)\cdot...\cdot\psi_0(\xi_N), \tag{2.42}$$

$$\Psi_{1,1,...,0}(\xi_1,\xi_2,...,\xi_N) = \psi_1(\xi_1)\,\psi_1(\xi_2)\cdot...\cdot\psi_0(\xi_N), \tag{2.43}$$

and so on.

The polynomials Ψ_i are orthogonal. Hence, the weighting coefficients α_i of the expansion, defined in Equation (2.39), are computed using a spectral projection

$$\alpha_i = \frac{\int\limits_{\Omega} y\Psi_i\rho(\xi)d\xi}{\int\limits_{\Omega}\Psi_i^2\rho(\xi)d\xi}, \tag{2.44}$$

where Ω is the uncertain input-parameter space. The joint probability density function $\rho(\xi)$ is computed from the one-dimensional probability density functions since the uncertain input parameters are uncorrelated. The integral in the denominator of Eqn. (2.44) is determined analytically. The integral in the nominator is computed by a Gauss quadrature, which requires p_j+1 quadrature points for an exact integration in each dimension. If we consider, for instance, a three-dimensional polynomial with $p_j = 3$, then $(3+1)^3 = 64$ integration points are required to determine all coefficients of the expansion. Note that the Gauss quadrature rules strictly define the integration points, and the points do not coincide for different polynomial orders. That makes reuse of already computed points impossible if the polynomial order increases. A nested quadrature rule can be used to bypass this limitation, but this topic is out of scope of this thesis.

The mean $E(y)$ and the variance $\mathrm{Var}(y)$ of the output quantity are defined as

$$E(y) = \int\limits_{\Omega} y\rho(\xi)d\xi, \tag{2.45}$$

$$\mathrm{Var}(y) = \int\limits_{\Omega}\big(y-E(y)\big)^2\rho(\xi)d\xi. \tag{2.46}$$

Due to the orthogonality condition, the mean and the variance are equal to the first two polynomial coefficients: $E(y) = \alpha_0$ and $\mathrm{Var}(y) = \alpha_1$.

Besides the analytical moments of y, the NIPCE allows to compute conditional expectations of the output quantity $E\big(y|\xi_i,\xi_j,...\big)$, which are used in the next section for a sensitivity analysis.

Furthermore, a probability density function (PDF) of the output quantity can be computed using a Monte Carlo simulation applied to the polynomial expansion.

For all UQ studies in PAPER-UQ-STABILITY and PAPER-UQ-FTF, the polynomial expansions are constructed using a MATLAB tool, developed by Češnovar in his term project [20], supervised by the present author.

2.2.2 Sensitivity analysis

Besides computing uncertainties and probabilities, the polynomial expansion of the output quantity makes possible an (approximate) analytical computation of local sensitivities, i.e. the

derivatives of the output quantity with respect to the input parameters:

$$\frac{\partial y}{\partial \xi_i} = \sum_{j=0}^{P-1} \alpha_j \frac{\partial \Psi_j(\xi)}{\partial \xi_i}. \tag{2.47}$$

These derivatives can be evaluated, for instance, at the means of the input parameters to make a global statement about the system sensitivity. Another way is to compute the mean and the variation of the derivatives. The latter approach is used in PAPER-UQ-STABILITY.

It is also possible to perform a derivative-free sensitivity analysis using variance-based sensitivity indices, so-called Sobol indices[101]. This approach provides a global sensitivity analysis and is followed in PAPER-UQ-FTF. Sobol indices are a very effective tool to determine the most dominant uncertain parameters. Sobol indices S_{ξ_i} and $S_{\xi_i \xi_{j\ldots}}$ quantify contributions from each input parameter and parameter interactions to the output variance:

$$S_i = \frac{\mathrm{Var}\left(E\left(y|\xi_i\right)\right)}{\mathrm{Var}\left(y\right)}, \tag{2.48}$$

$$S_{ij} = \frac{\mathrm{Var}\left(E\left(y|\xi_i,\xi_j\right)\right)}{\mathrm{Var}\left(y\right)} - S_i - S_j, \tag{2.49}$$

$$S_{ijk} = \frac{\mathrm{Var}\left(E\left(y|\xi_i,\xi_j,\xi_k\right)\right)}{\mathrm{Var}\left(y\right)} - S_i - S_j - S_{ij} - S_{ik} - S_{jk}, \tag{2.50}$$

where $E\left(y|...\right)$ is the conditional expectation. S_i is the individual contribution of parameter ξ_i, S_{ij} and S_{ijk} are the contributions of interactions between parameters (ξ_i, ξ_j) and (ξ_i, ξ_j, ξ_k). The sum of all Sobol indices yields unity:

$$\sum_{i=1}^{N} S_i + \sum_{i=1}^{N} \sum_{j>i}^{N} S_{ij} + ... + S_{1,2,...,N} = 1. \tag{2.51}$$

Finally, Fig. 2.2 shows an overview of all features of the NIPCE, presented in this chapter.

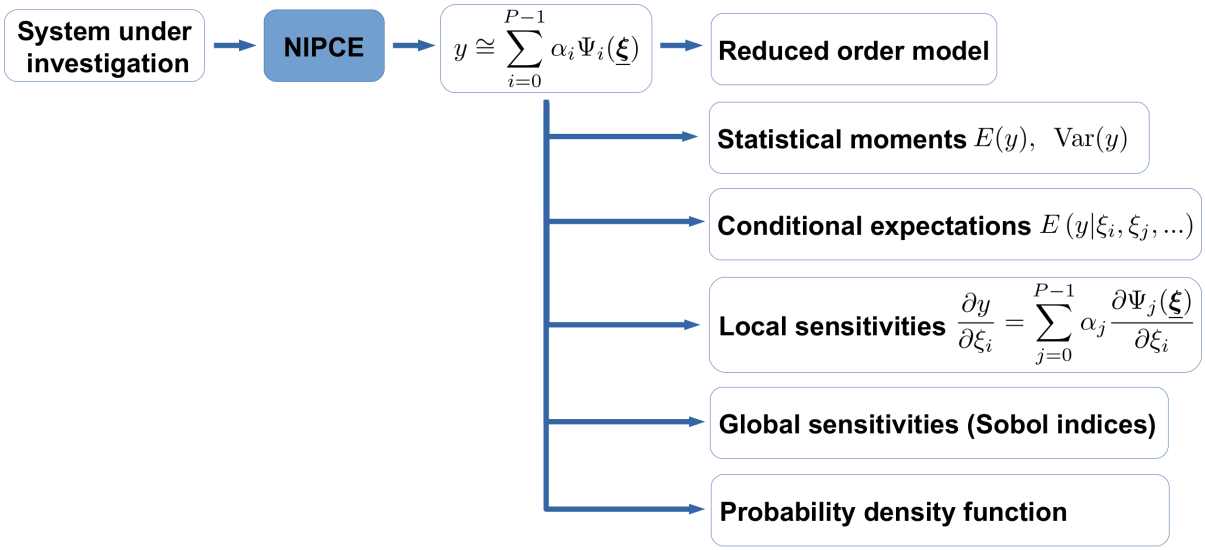

Figure 2.2: Overview of all features of the NIPCE presented in this thesis and the corresponding publications.

3 Applications of the LRF

This chapter of the thesis is devoted to the applications of the LRF approach. Section 3.1 describes the outcome of PAPER-LRF, which introduces the LRF approach to the thermoacoustic research community and investigates the stability and the flame response of a laminar flame in a low-frequency regime. In this case, the flame is acoustically compact.

Next, Section 3.2 applies LRF to a reheat combustor with a turbulent auto-ignition flame in a high-frequency regime when the flame is no more acoustically compact.

3.1 PAPER-LRF: Thermoacoustic analysis of a laminar premixed flame using a linearized reacting flow solver

Label: PAPER-LRF

Summary: This paper is the first work about the LRF that introduces the concept and validates it on a simple example of an attached and lifted laminar premixed flame. LRF includes the flow–flame–acoustics interaction by design since it linearizes the reaction term and does not require an external FTF. The FTF computed with the LRF solver agrees with the reference FTF identified from the CFD simulation with a broadband excitation. To achieve this quantitative agreement, it was crucial to retain first-order fluctuations of material properties, such as viscosity and thermal diffusivity. At the same time, the straightforward linearization of the reaction term fully suffices, and no sophisticated treatment of the strongly non-linear Arrhenius term is required. The LRF solver also computes eigenmodes of the laminar flames, i.e. the mode growth-rate, frequency, and shape. Results are compared to the established hybrid methods that couple FTFs with a low-order thermoacoustic network-model or with a linearized Navier-Stokes equations solver. All solvers capture the dominant thermoacoustic mode, but only the LRF resolves the local flow-flame interaction, revealing e.g. the onset of the flame movement and the convective propagation of distortions along the flame.

Contribution: The present author proposed and implemented the reaction linearization, then performed all corresponding simulations. M. Meindl developed the framework of the DG-FEM discretized Navier-Stokes equations. W. Polifke contributed a refinement of the LRF approach and a critical revision. All authors contributed to the rebuttal to the reviewers' comments; the present author implemented the comments into the manuscript.

Status: Presented at 37th International Symposium on Combustion, published in Proceedings of the Combustion Institute.

Review process: Peer-reviewed

Reference: A. Avdonin, M. Meindl, and W. Polifke. "Thermoacoustic Analysis of a Laminar Premixed Flame Using a Linearized Reacting Flow Solver." Proceedings of the Combustion Institute 37 (2019): 5307-14. https://doi.org/10.1016/j.proci.2018.06.142.

Comments: M. Kühn contributed to further developing the LRF approach in his term project [61], supervised by the present author. He showed how to incorporate equivalence-ratio perturbations in the LRF. Fig. 3.1 shows the flame response to equivalence-ratio perturbations imposed on the laminar flames, studied in PAPER-LRF. The LRF results (--) are somewhat different from the reference transfer function (—), especially at maxima of the transfer function, but the LRF captures the correct trend.

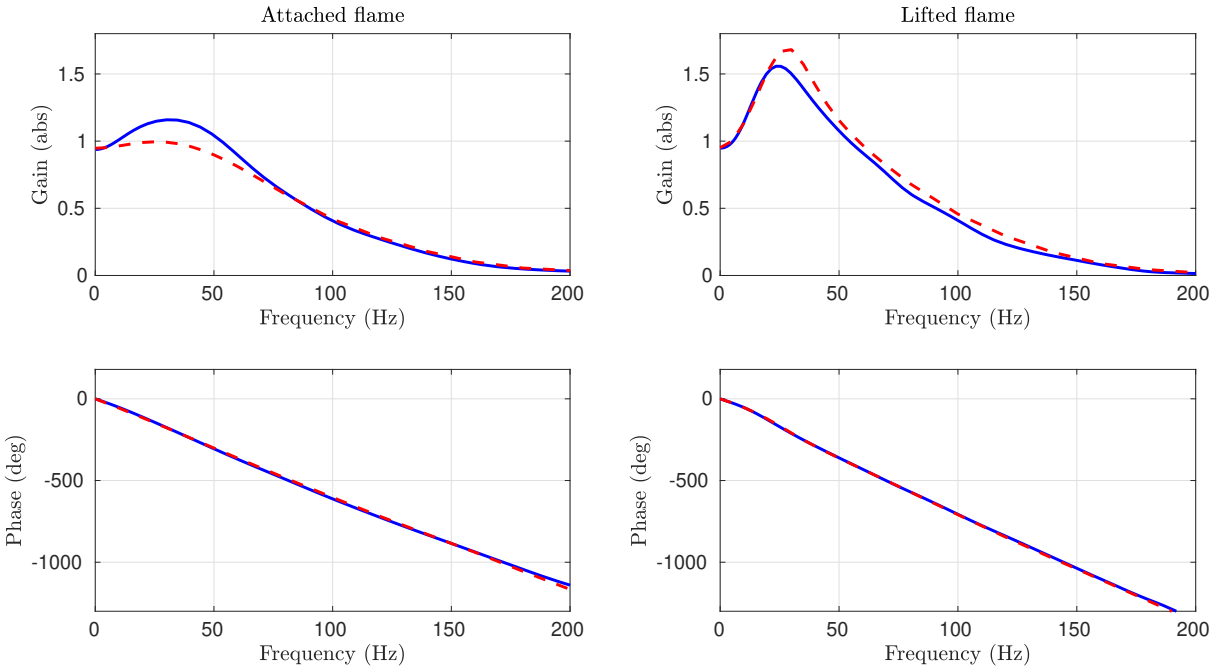

Figure 3.1: Frequency response of the attached (left) and lifted flame (right) to equivalence-ratio fluctuations identified using the CFD simulation (—) and computed using the LRF solver (--). Adopted from [61].

Recently, Meindl et al. [68] applied a two-step linearized reaction mechanism and showed the LRF approach exhibits no spurious entropy generation in contrast to a *hybrid method* coupled with a global FTF.

3.2 High-frequency response of a non-compact turbulent auto-ignition flame

3.2.1 Numerical setup

The next application of the LRF approach is a generic reheat combustor with a rectangular cross-section. The choice of a simple rectangular geometry suppresses a mode rotation and thus

facilitates the analysis. Furthermore, this geometry allows to apply periodic boundary conditions in the spanwise direction, so the case can be seen as quasi two-dimensional and the linear analysis can proceed in 2D. The geometry as well as the flame front are shown in Fig. 3.2.

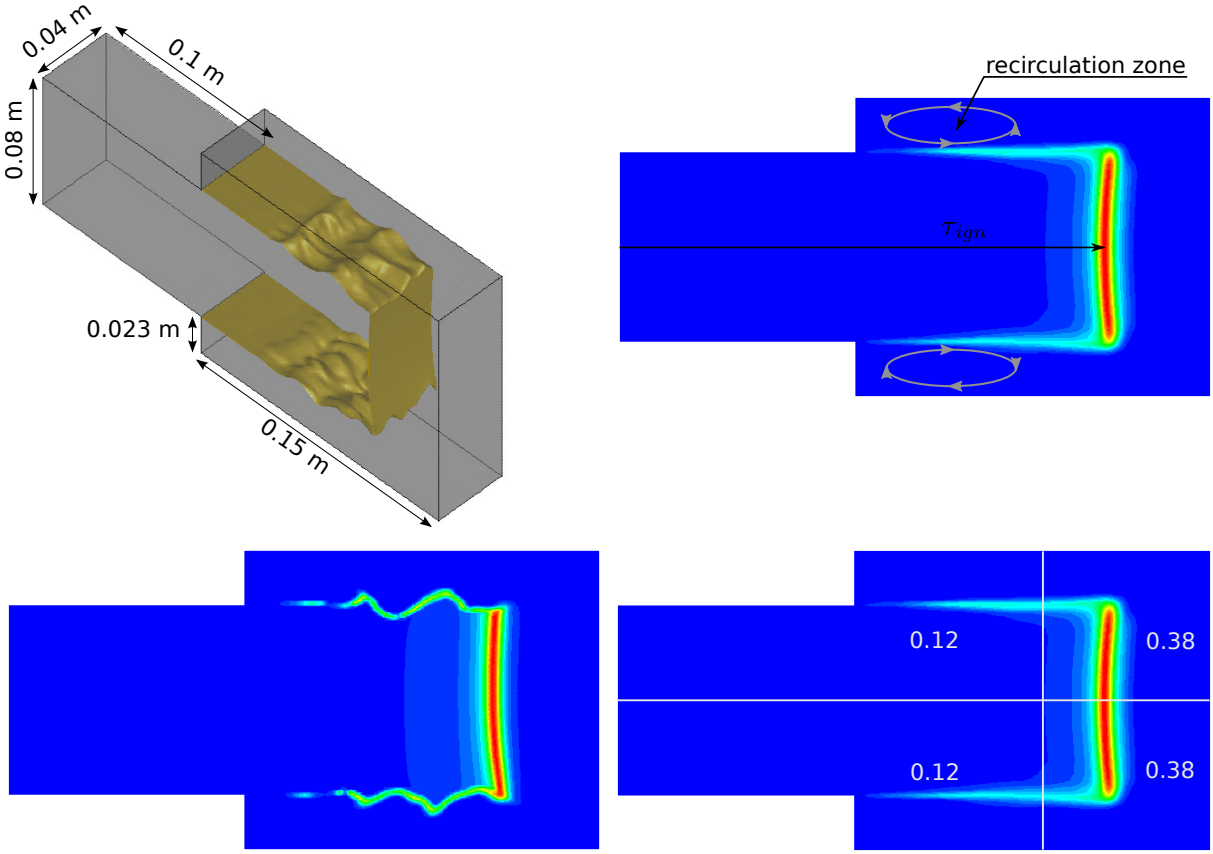

Figure 3.2: Top left: sketch of the reheat combustor with a snapshot of the flame front. Bottom left: instantaneous heat-release rate at the midplane (bottom left). Top right: time-averaged heat-release rate at the midplane. Bottom right: partition of the midplane in the top and bottom halves by a horizontal line and in the left and right quarters by a vertical line at $x = 0.18$ m, each zone is labeled by its relative contribution to the global heat-release rate.

Large-eddy simulations are performed in Ansys Fluent 18. Tab. 3.1 summarizes boundary conditions and material properties. The reheat combustor is fed by perfectly homogenous mixture of methane and first-stage combustion products. Because of the high inlet temperature and operating pressure, the mixture auto-ignites after $\tau_{ign} \approx 3.9$ ms at position 0.21 m downstream of the inlet, building a vertical flame front of length $l_{f\perp} \approx 0.08$ m in the core flow, stabilized by the auto-ignition (vertical reaction zone in Fig. 3.2, top right). The area jump in the combustor creates recirculation zones that stabilize the flame by shear-layers (horizontal reaction zones in Fig. 3.2, top right). The shear-layer stabilized flame has a length $l_{f\parallel} \approx 0.11$ m. Fig. 3.2 (bottom right) shows the heat-release-rate distribution over four zones at the midplane. The auto-ignition stabilized region contributes at most to the global heat release ($2 \cdot 0.38\%$). The inlet is laminar, so the turbulence is generated in the shear layer at the area jump and disrupts the flame, which can be seen in Fig. 3.2 (bottom left and right) that compares the instantaneous and time-averaged

Inlet temperature	1270.7 K
Inlet velocity	55 m/s
Composition at the inlet:	
Y_{CH_4}	0.01
Y_{O2}	0.145
Y_{CO_2}	0.0555
Y_{H_2O}	0.0455
Y_{N_2}	0.744
Outlet pressure	18×10^5 Pa
Heat capacity at constant pressure	1300 J/(kgK)
Average molar mass of the mixture	28.16 kg/kmol
Heat capacity ratio	1.29
Speed of sound at the inlet	697 m/s
Dynamic viscosity	1.72×10^{-5} kg/(ms)
Thermal conductivity	4.54×10^{-2} W/(mK)
(Turbulent) Schmidt number	0.71
Simulation time-step	5×10^{-6} s

Table 3.1: Boundary conditions, material and computational parameters for the reheat-combustor simulations.

flame positions. The walls are adiabatic with a no-slip boundary condition, except the top and bottom walls downstream of the area jump. These walls are used to create acoustic standing waves (see Section 3.2.2). In the case with no excitation, these walls and the outlet are made non-reflecting to ensure a stable configuration. Ansys Fluent models non-reflecting inlet and outlet boundaries using the characteristics of the Navier-Stokes equations [86], but there is no non-reflecting option for the walls in the solver, so they are modeled as a non-reflecting inlet with zero velocity. M. Bertsch extensively studied this approach and the application of impedance boundary conditions in Ansys Fluent in his term paper [14], supervised by the present author.

The material properties c_p, μ, D[1], and κ (see Tab. 3.1) are kept constant to avoid additional terms in the LRF coming from the linearization of these parameters.

The turbulence is modeled by the WALE model [77]. The turbulent auto-ignition flame is modeled using the approach of Kulkarni et al. [62, 63]: the reaction is tabulated (see Section 2.1.3.3) and the turbulence–chemistry interaction is taken into account by eight stochastic fields. The chemical look-up table is generated using perfectly stirred reactors in CANTERA [43] with Galway C3-41 mechanism [84]. The reactant mixture is perfectly premixed, and there are no heat losses at the walls, so the reaction is fully controlled by a single parameter – the progress variable Y_c. The adiabatic flame temperature is 1712 K, which corresponds to the speed of sound 809 m/s. The tabulation process does not account for pressure fluctuations, so the acoustic pressure affects the heat-release rate only via density fluctuations[2], see Eqns. (2.24)–(2.26).

The mesh of the reheat combustor for the LES is shown in Fig. 3.3. It has 850000 cells in total.

[1] The diffusion D is computed using the dynamic viscosity and the Schmidt number.

[2] To include the direct effects of pressure fluctuations on the mass-specific reaction rates, one can follow the approach suggested by Zellhuber et al. [113].

The fine inner zone ($x > 0.09$ m $\cap$ $x < 0.24$ m) consists of cubic cells with $\Delta h = 0.001$ m. The inlet and outlet zones have a two times coarser mesh with an additional stretching towards the inlet.

All linearized simulations are performed in COMSOL 5.3. Exploiting periodicity in the spanwise direction allows reducing the original 3D problem to a 2D plane problem. Fig. 3.4 shows the 2D mesh in COMSOL that consists of 26900 square elements with $\Delta h = 0.001$ m, so it has the same resolution as the inner zone in the LES. The time-averaged flow fields ($\overline{u}$, $\overline{p}$, $\overline{T}$, $\overline{\rho}$, $\overline{h}$, $\overline{Y}_c$, $\overline{\omega}_h$, $\overline{\omega}_c$, μ_{SGS}), required to run the LRF solver, are taken from the midplane of the LES with no excitation. The flow fields are time-averaged for 0.035 s (7000 time steps), which corresponds roughly to 8 flow-through times.

3.2.2 Excitation mechanism

The reheat combustor is excited transversely by acoustic waves at the top and bottom walls downstream of the area jump. These waves travel in the transverse direction across the flame, see Fig. 3.5. The incoming acoustic wave intensities I_{in} are defined in pressure units (Pa) in Ansys Fluent:

$$I_{in,top} = A_{exc} \cos\left(2\pi f t\right), \tag{3.1}$$

$$I_{in,bottom} = A_{exc} \cos\left(2\pi f t + \theta\right). \tag{3.2}$$

Thereby, the excitation is superimposed with the non-reflecting boundary conditions originally applied at the walls. The non-reflecting walls are required to avoid resonance of the excitation with the transverse modes. At the resonance (or close to it), the heat-release fluctuations no longer depend on the excitation, and the approach to assess the driving force fails. The excitation is performed with the amplitude $A_{exc} = 32 \times 10^3$ Pa either asymmetrically or symmetrically at discrete frequencies from 1000 Hz to 5000 Hz creating a standing wave. This amplitude is chosen to achieve a clear sinusoidal response of the heat-release rate with a high signal-to-noise ratio. Only at 1000 Hz the excitation amplitude is increased to $A_{exc,1000\ Hz} = 64 \cdot 10^3$ Pa for a better signal-to-noise ratio. The asymmetric or out-of-phase ($\theta = 180°$) excitation creates a standing wave, similar to the first transverse T1 mode with a pressure node and a velocity anti-node at the centerline, moving the flame up and down, see Fig. 3.5 (left) and Fig. 3.9. The symmetric or in-phase ($\theta = 0°$) excitation forces a pressure anti-node and a velocity node at the centerline (like the second transverse T2 mode), causing the flame pulsation, see Fig. 3.5 (right).

The transverse dimension of the flame ($l_{f\perp} \approx 0.08$ m) is comparable to the dimensions of the generated standing waves, therefore the flame is acoustically non-compact to the transverse excitation, and local consideration of the heat-release response is mandatory. This requirement motivates the application of the LRF solver.

The pressure $\widetilde{p}$ and local heat-release rate $\widetilde{\dot{q}}$ fields are sampled at a certain rate for each excitation frequency, see Table 3.2. Storing the time samples for each grid point will exceed the memory available, so only one characteristic plane parallel to the excitation (the midplane) is observed. The linear fluctuations of the pressure p' and the heat-release rate $\dot{q}'$ are extracted using a Fast Fourier Transformation. Then the local and the global Rayleigh indices *ri*, *RI* are

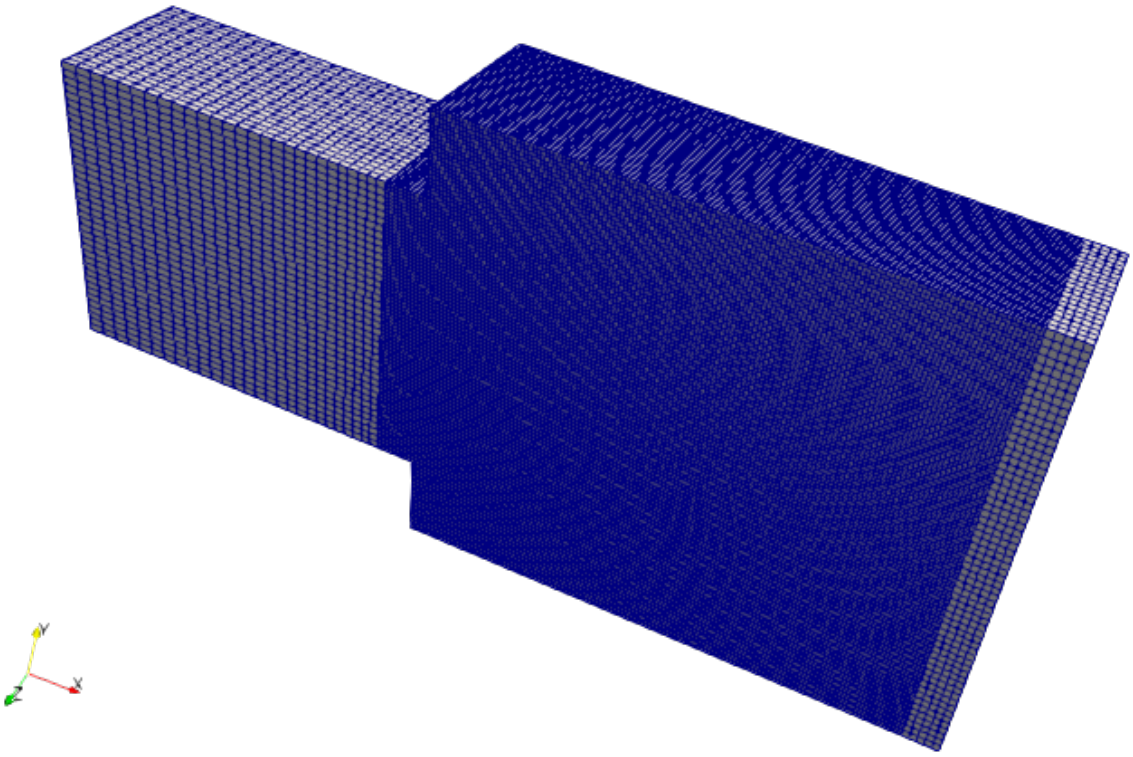

Figure 3.3: 3D mesh of the reheat combustor for the LES.

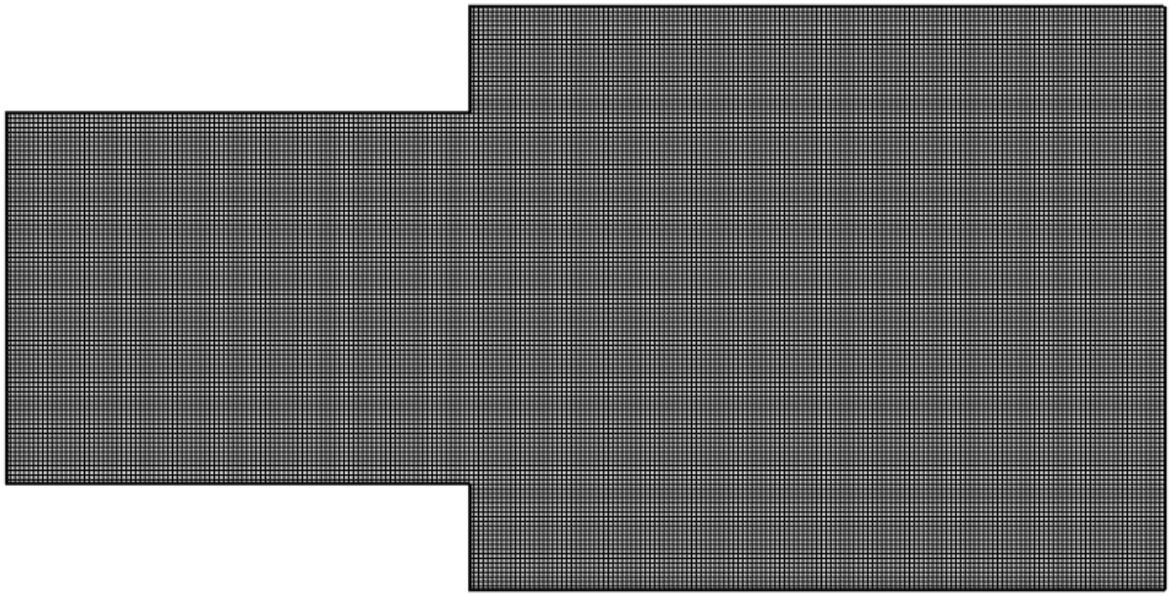

Figure 3.4: 2D mesh of the reheat combustor for the LRF simulations.

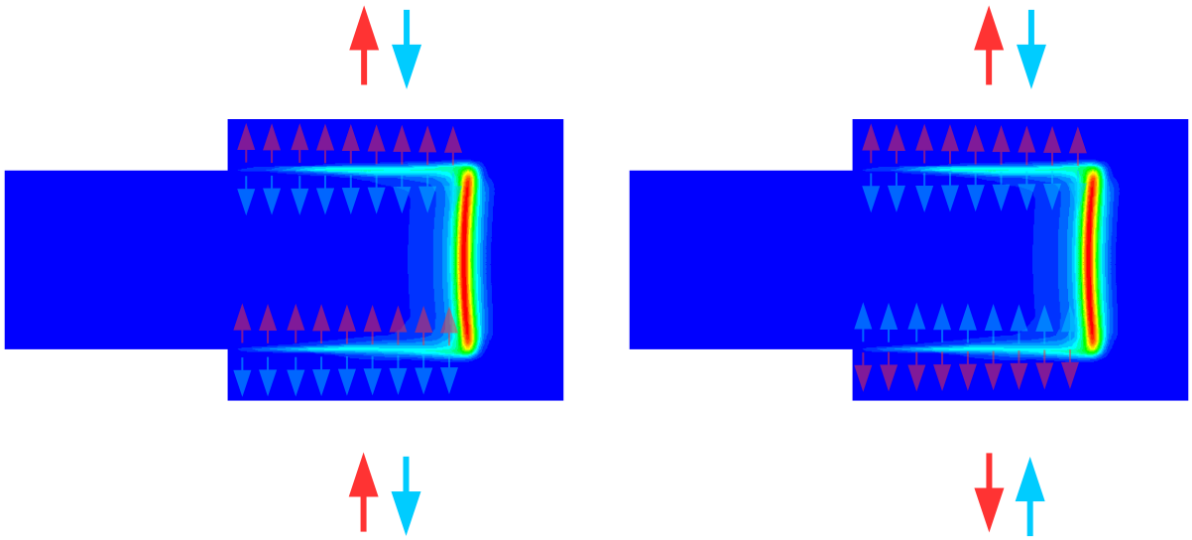

Figure 3.5: Asymmetric excitations move the flame up and down (left); symmetric excitations cause the flame pulsation (right). Red and blue arrows show the onset of the flame motion with the phase shift 180°.

Frequency (Hz)	Settling time (period)	Sampling time (period)	Samples rate (samples/period)
1000	20	5	20
1429	20	15	20
2000	20	10	20
2500	20	17	20
3030	20	10	22
3500	20	15	19
3922	20	19	17
4545	20	25	22
5000	20	30	20

Table 3.2: Temporal parameters for the excitation simulations.

calculated in the frequency domain:

$$RI_\Omega = \int_\Omega ri\, dV = \int_\Omega \frac{\overline{\gamma}-1}{\overline{\gamma p}} \frac{1}{2} \hat{p}\hat{q}^* dV = \int_{\Omega_i} \frac{\overline{\gamma}-1}{\overline{\gamma p}} \frac{1}{2} \|\hat{p}\| \|\hat{q}\| \cos(\theta) dV, \tag{3.3}$$

where $\hat{p}$ and $\hat{q}$ are the complex fluctuations of the pressure and the heat-release rate, * is the complex conjugate, $\|.\|$ denotes the magnitude, and θ is the phase difference between $\hat{p}$ and $\hat{q}$. All quantities in Eqn. 3.3 are defined locally and are, in general, not constant. But in this case, γ is constant and the mean pressure $\overline{p}$ is approximated by the constant outlet pressure $18 \cdot 10^5$ Pa. The latter approximation is justified as long the same definition of the Rayleigh index is used in both LES and linear computations. All linear computations are performed directly in the frequency domain. The Rayleigh index is normalized with the power of the incoming acoustic waves P_{in} to compare results obtained with different excitation amplitudes:

$$RI_{norm} = \frac{RI}{P_{in,top} + P_{in,bottom}}, \tag{3.4}$$

where

$$P_{in,top} = P_{in,bottom} = \frac{1}{T}\int_t \left[p' u_i' n_i\right]_{top} l_{top} dt = \frac{1}{T}\int_t \frac{I_{in,top}}{2}\frac{I_{in,top}}{2\overline{\rho}_{top}\overline{c}_{top}} l_{top} dt = \frac{A_{exc}^2 l_{top}}{8\overline{\rho}_{top}\overline{c}_{top}} \quad (3.5)$$

with $l_{top} = 0.15$ m, $\overline{\rho}_{top}\overline{c}_{top} \approx 2900$ kg/(m^{2}s); n is a unit normal vector to the surface.

3.2.3 Flame response

LES results

Fig. 3.6 shows the fluctuating pressure field that is forced by the excitation in the LES. Under the asymmetric excitation at frequencies lower than 4544 Hz, the pressure field is similar to the T1 mode with a node at the centerline. At higher frequencies, the excited pressure field looks like the T1 mode mixed with the first longitudinal mode. Under the symmetric excitation with the increasing frequency, the pressure field resembles the T2 mode mixed with the first longitudinal mode. Besides the similarity with acoustic eigenmodes, the pressure field shows peaks in the shear layer zones, that represent the vortex cores. The significance of these vortices decreases with increasing frequency for both excitation types.

Fig. 3.7 shows a more or less sinusoidal response of the heat-release rate to the asymmetric (left) and symmetric (right) excitations in the LES. The asymmetric excitation produces out-of-phase heat-release-rate fluctuations in the top and bottom halves of the combustor that cancel each other out and result in no net fluctuation over the entire combustor. In contrast, the symmetric excitation yields a non-zero global heat-release-rate fluctuation $\dot{Q}' \neq 0$.

Fig. 3.8 shows the RI computed for the top and bottom halves of the combustor (○). It is remarkable that the asymmetric excitation with $\dot{Q}' = 0$ yields a positive RI, but the symmetric excitation with $\dot{Q}' \neq 0$ yields a negative RI for frequencies between 2000 Hz and 4000 Hz. That means the symmetric excitation stabilizes the flame in that frequency range despite the non-zero global fluctuation in the heat-release rate. A possible reason for this behavior might be the T1 mode. According to a Helmholtz solver with a passive flame[3], the T1 mode occurs around 3000 Hz for a burner configuration with the reflecting walls, see Fig. 3.9. In the LES, the top and bottom walls downstream of the area jump are non-reflecting, so the T1 mode should not be present. Nevertheless, the walls might still be weakly reflecting, so a weak T1 mode might occur and disturb the symmetric excitation decreasing the RI. The occurrence of the T1 mode would also explain the maximum in RI around 3500 Hz for the asymmetric excitation.

Fig. 3.7 shows the RI, computed in the quarters of the midplane, previously defined in Fig. 3.3 (bottom right). This zonal approach separates the shear-layer (×) and auto-ignition (□) stabilized regions. Surprisingly, both flame regions contribute almost equally to the global RI[4], although the auto-ignition region shows a comparatively higher mean heat-release rate, see Fig. 3.3 (bottom right).

[3]The Helmholtz solver with the passive flame has no source terms related to the heat-release rate. Hence, the flame affects the acoustics passively only through the change in the mean fields across the flame, see for instance [79].

[4]If the chemistry tabulation would include pressure fluctuations, the situation could change.

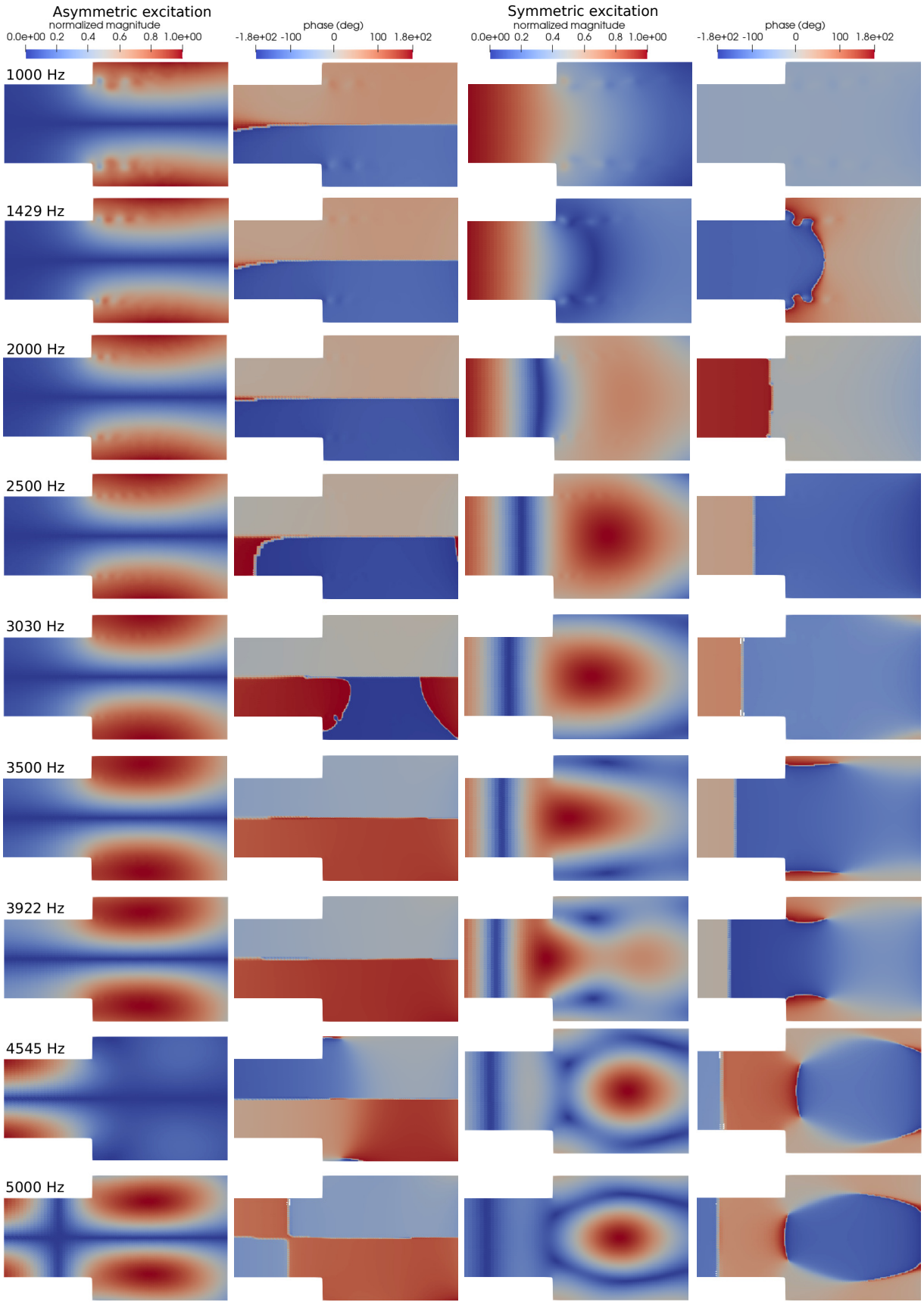

Figure 3.6: Pressure fluctuations extracted from the midplane of the excited LES.

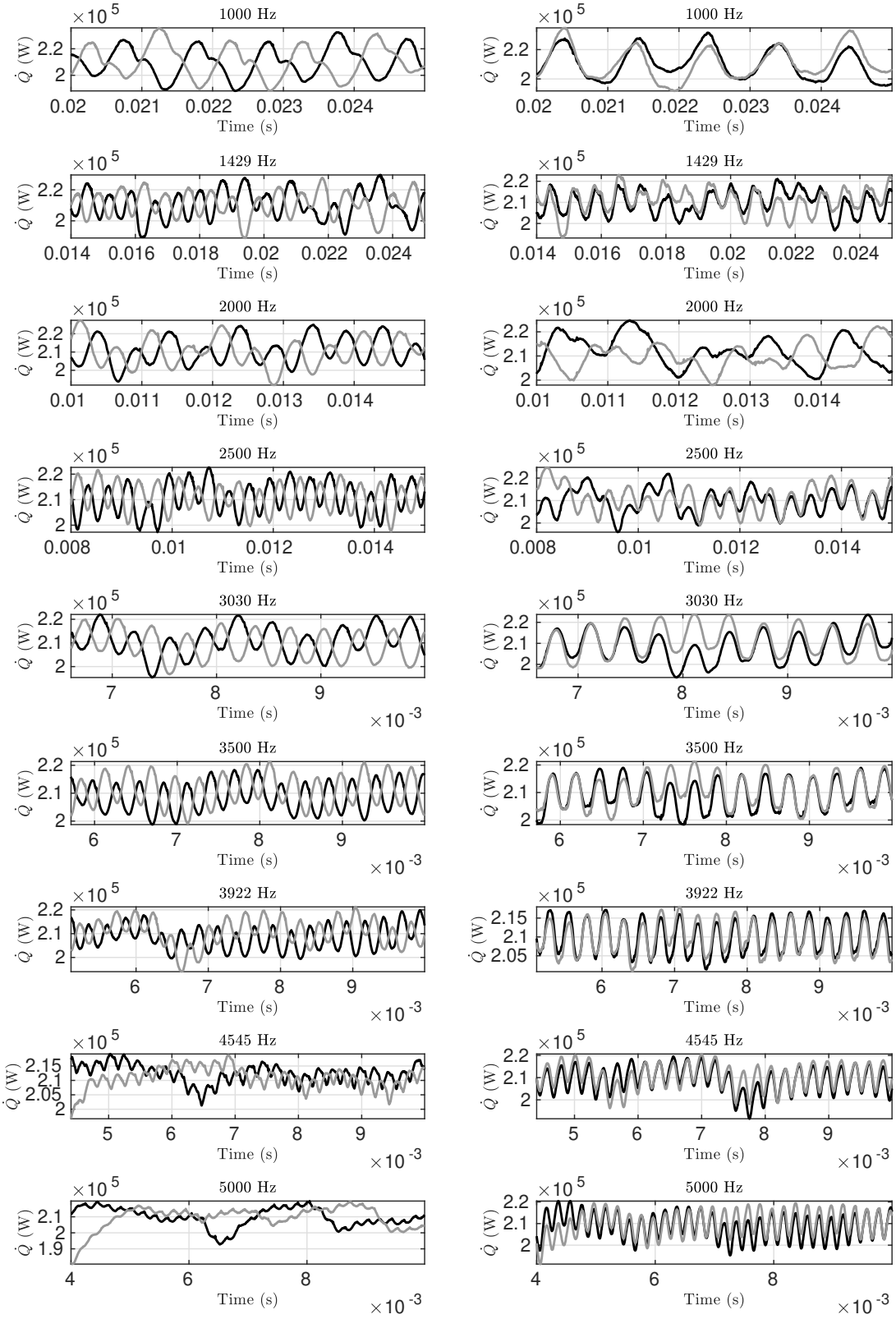

Figure 3.7: Response of the heat-release rate to the asymmetric (left) and symmetric (right) excitations in the LES. Black and gray lines show the heat-release rate integrated over the top and bottom halves of the combustor.

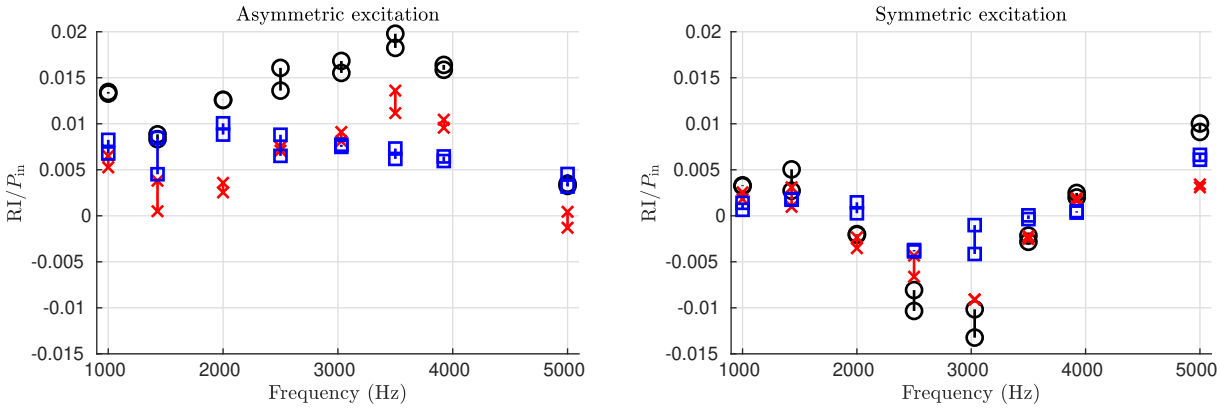

Figure 3.8: Normalized Rayleigh index computed for different zones in LES: the top and bottom halves (○), the left (×) and right quarters (□).

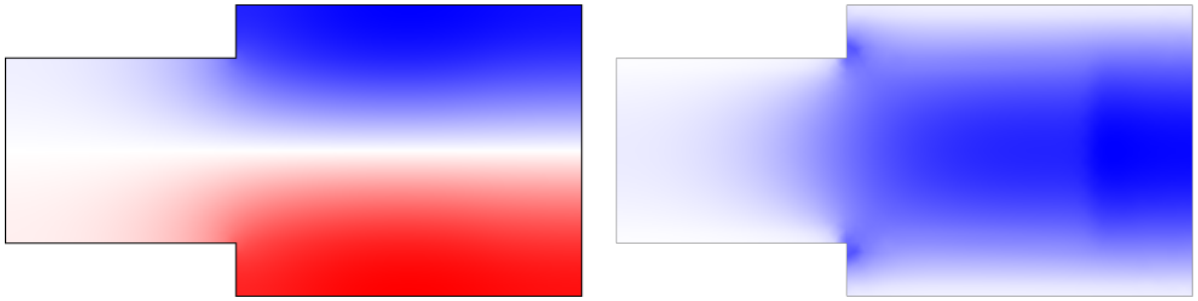

Figure 3.9: The real part of the pressure fluctuations (left) and the imaginary part of the transverse velocity fluctuations (right) of the T1 mode at 3029 Hz. Positive values are colored in red, negative values in blue. The T1 mode is computed in COMSOL using a Helmholtz solver with a passive flame for a burner configuration with reflecting walls.

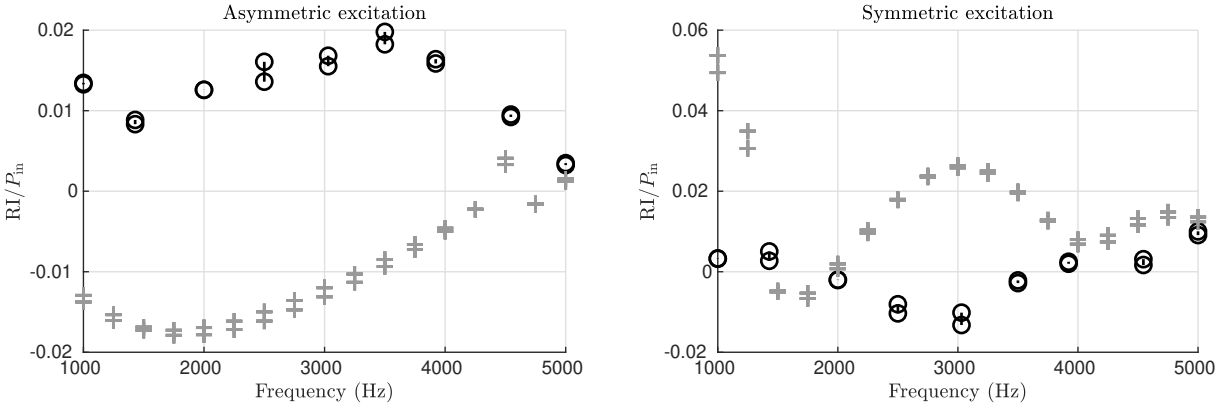

Figure 3.10: Normalized Rayleigh index in the top and bottom halves of the combustor midplane computed in the LES (○) and with the LRF neglecting convective effects (+).

The local distribution of the RI is shown in Fig. 3.11. The convected flame wrinkles in the shear-layers lead to an alteration of the RI along the flame sheet with a characteristic convective wavelength $\lambda_c \approx U_0 / f_{exc}$.

LRF results

Unfortunately, the straightforward application of the LRF model to the reheat combustor at high frequencies fails. The global *RI* for both excitations is positive and more than three orders of magnitude higher than in the LES. If the convective effects are neglected ($\overline{u} = 0$), then the magnitude of the *RI* becomes comparable to the LES results, but the trend is completely wrong, see Fig. 3.10. First of all, the current formulation of the LRF has a problem in the source term, amplified by the convection. A possible reason for that may be the application of the derivatives $[d\dot{\omega}_c / dY_c]^{tab}$ and $\left[d\dot{\omega}_q / dY_c\right]^{tab}$ from the look-up table, see Eqns. (2.27)–(2.28). The LRF approach has been validated in paper PAPER-LRF with the Arrhenius approach, but the linearized tabulation has never been applied. Hence, simpler test cases have to be examined to find out, where the LRF solver reaches its limits with the linearized tabulation. Maybe, a volume-integration or some kind of filtering can be applied to the problematic part of the combustion model in order to create a derivative-free formulation. Another reason for the LRF failure can lie in the nature of the flame under investigation. PAPER-LRF investigated a laminar flame that does not move without any excitation. However in the case of this reheat combustor, the flame is turbulent, i.e. the time-averaged fields do not match with the instantaneous fields and certainly do not fulfill the stationary Navier-Stokes equations. The time-averaged flame front is partially smeared out, so it is not clear if the linear flame dynamics can be captured well using the averaged fields. To answer this question, the LRF approach should be applied to different turbulent flame types. Such a deep additional investigation is not possible within this research. It requires one or several additional research projects. Instead, the mass-specific reaction term in the equation for the progress variable is set to zero ($\dot{w}'_c = 0$), and the convection is neglected ($\overline{u} = 0$), resulting in the E-FLAME model, see Section 2.1.6. The remaining part of this section is dedicated to the simplified LRF solver with the E-FLAME model (LRF_{EF}).

Fig. 3.12 shows the excited pressure fields computed with the LRF_{EF}. Since the mean flow is neglected, these pressure fields have a pure acoustic nature and are not disturbed by shear layers, as in the LES (see Fig. 3.6). Except for these differences in shear layers, the LES and LRF_{EF} results compare well.

Fig. 3.13 (top row) shows the fluctuations of the heat-release rate computed with the LRF_{EF} solver at 2500 Hz[5]. The change from a negative (blue color) to a positive (red color) value across the flame indicates the onset of the flame motion. The mean flow is neglected, so the flame is displaced by the acoustic velocity. The flame moves up and down for the asymmetric excitation and pulsates for the symmetric excitation. At the bottom of the same figure there is a local distribution of the RI. Although the RI changes across the flame, the integrated RI remains positive, as shown later in this section. Unfortunately, a direct comparison to the local RI distribution in the LES is difficult due to the convected flame wrinkles that are present in the LES (see Fig. 3.11). Hence, the global RI is inspected next.

A quantitative comparison of the RI between the LES and the simplified LRF solver with the

[5] Although the fluctuation of the heat-release rate and the distribution of the RI are shown only for one frequency, the character of the flame motion remains the same for all frequencies.

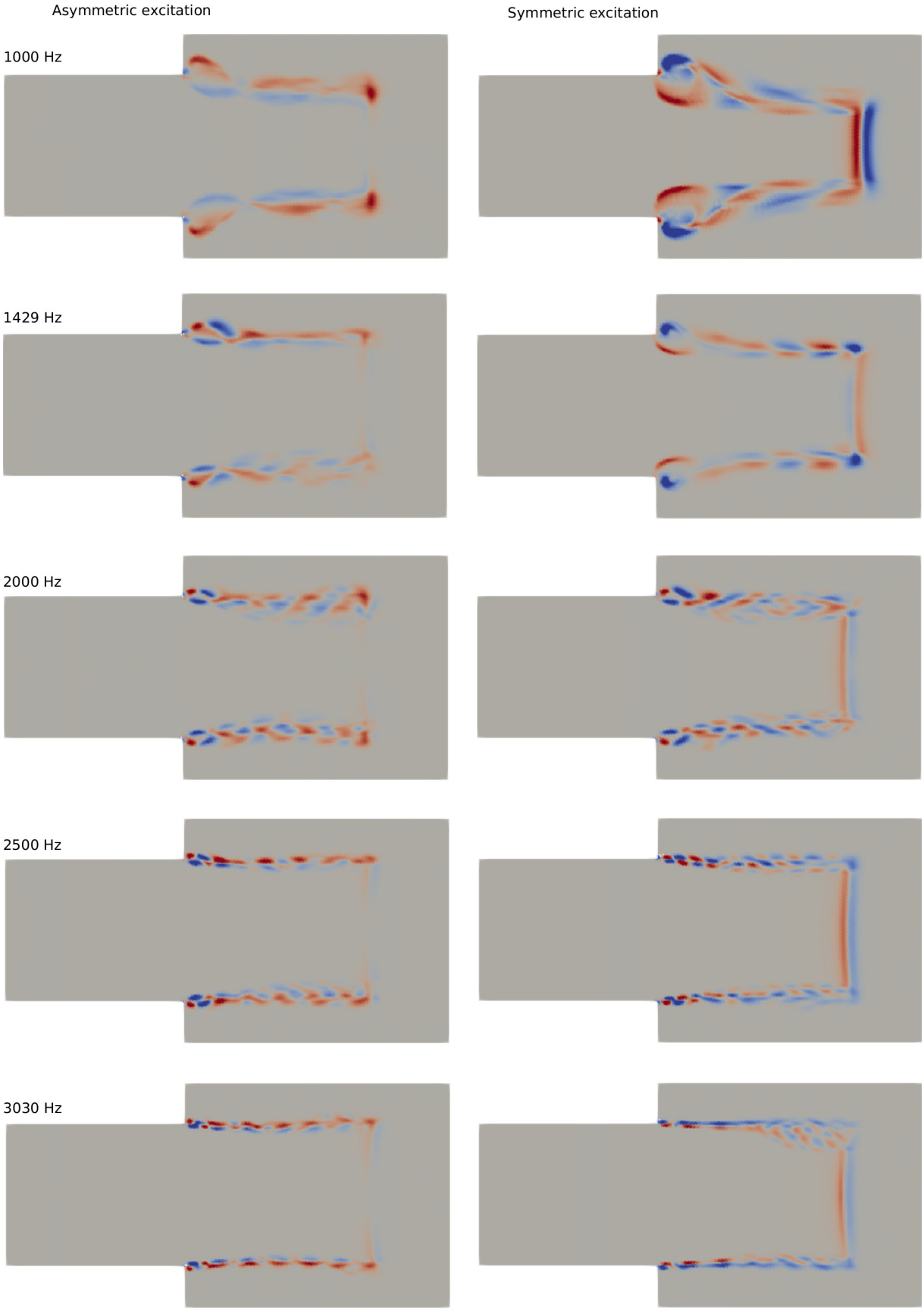
Asymmetric excitation
Symmetric excitation
1000 Hz
1429 Hz
2000 Hz
2500 Hz
3030 Hz

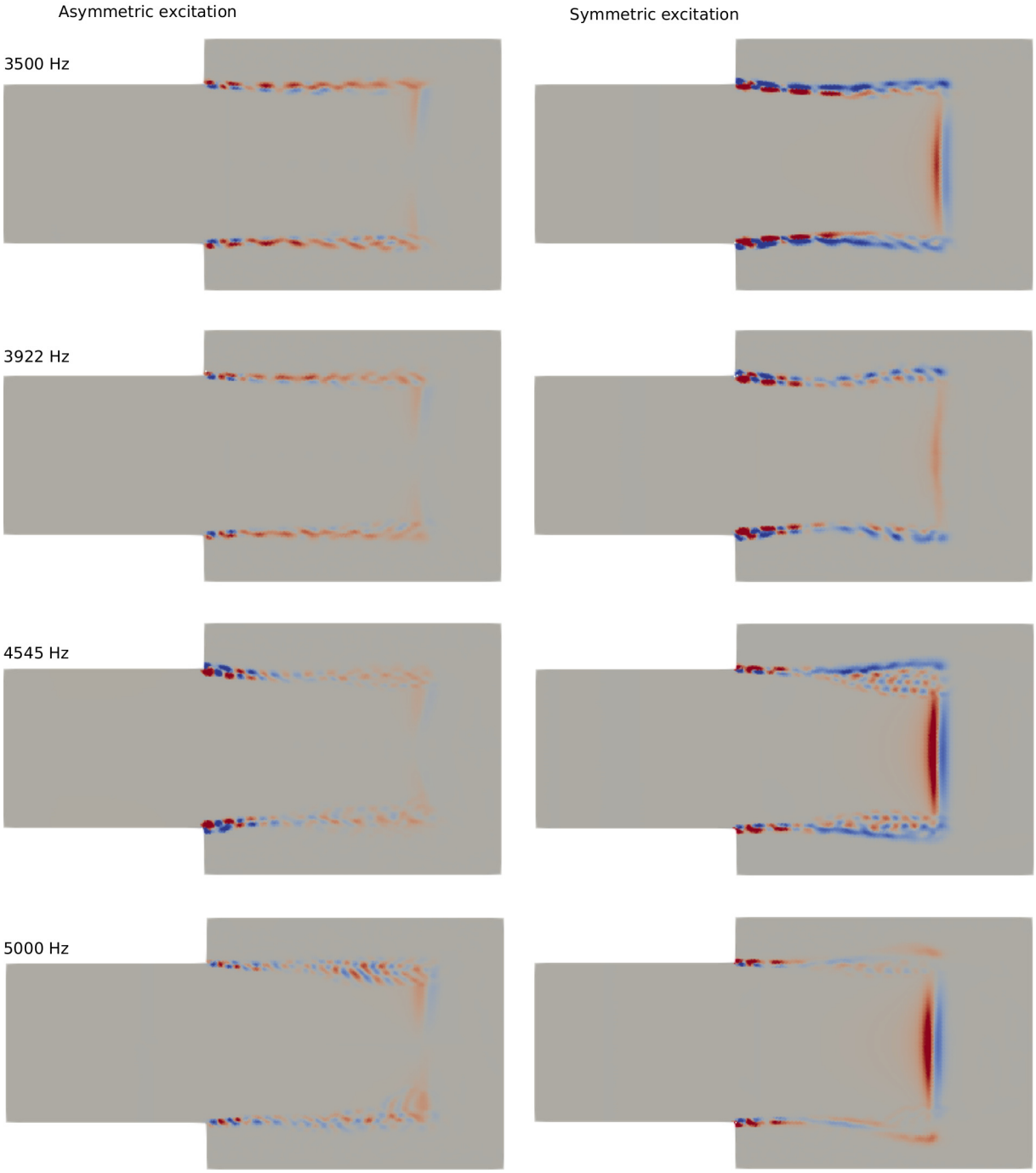

Figure 3.11: Local Rayleigh-index in the LES. Positive values are colored in red, negative values in blue.

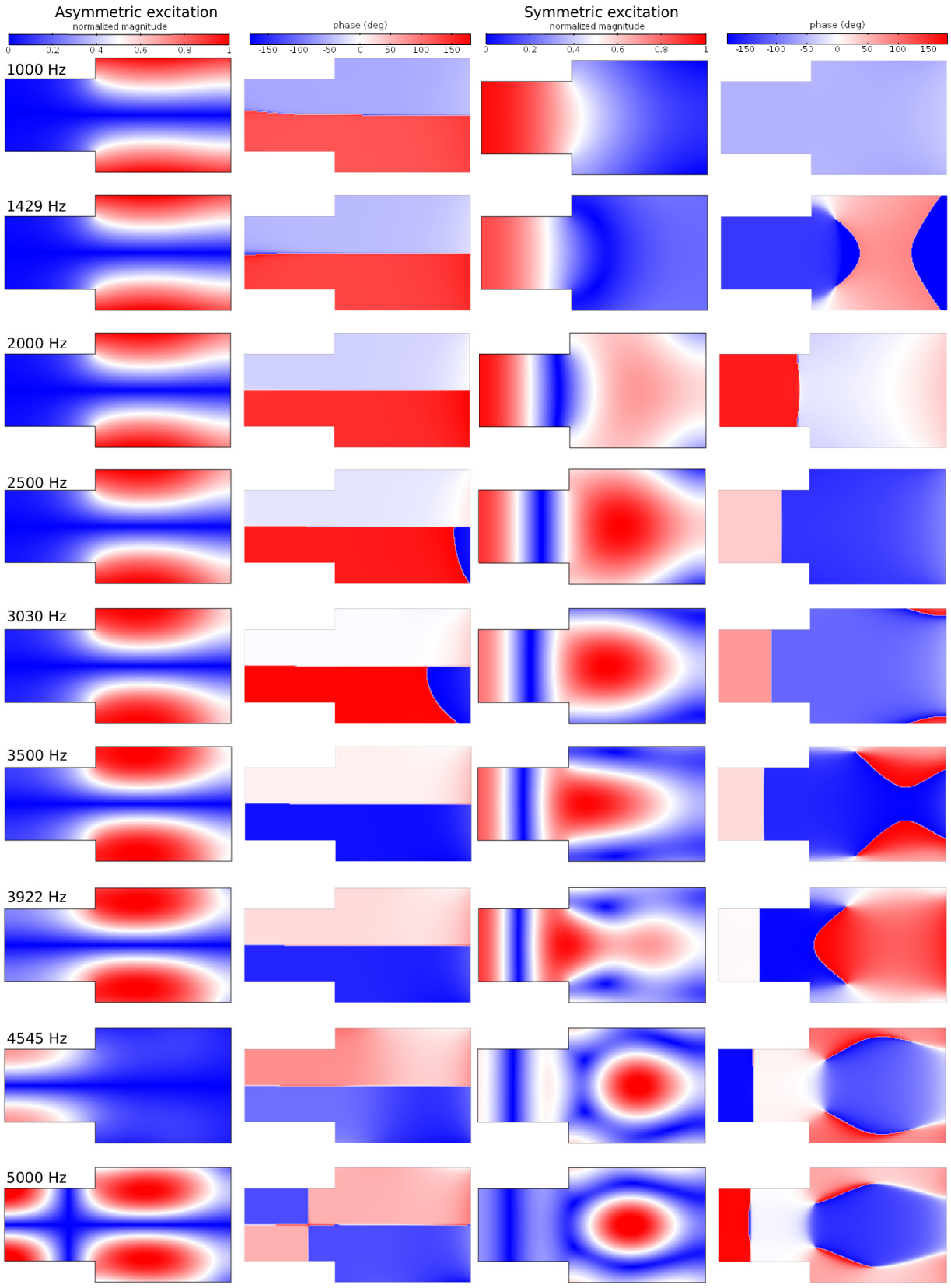

Figure 3.12: Pressure fluctuations computed with the LRF$_{EF}$.

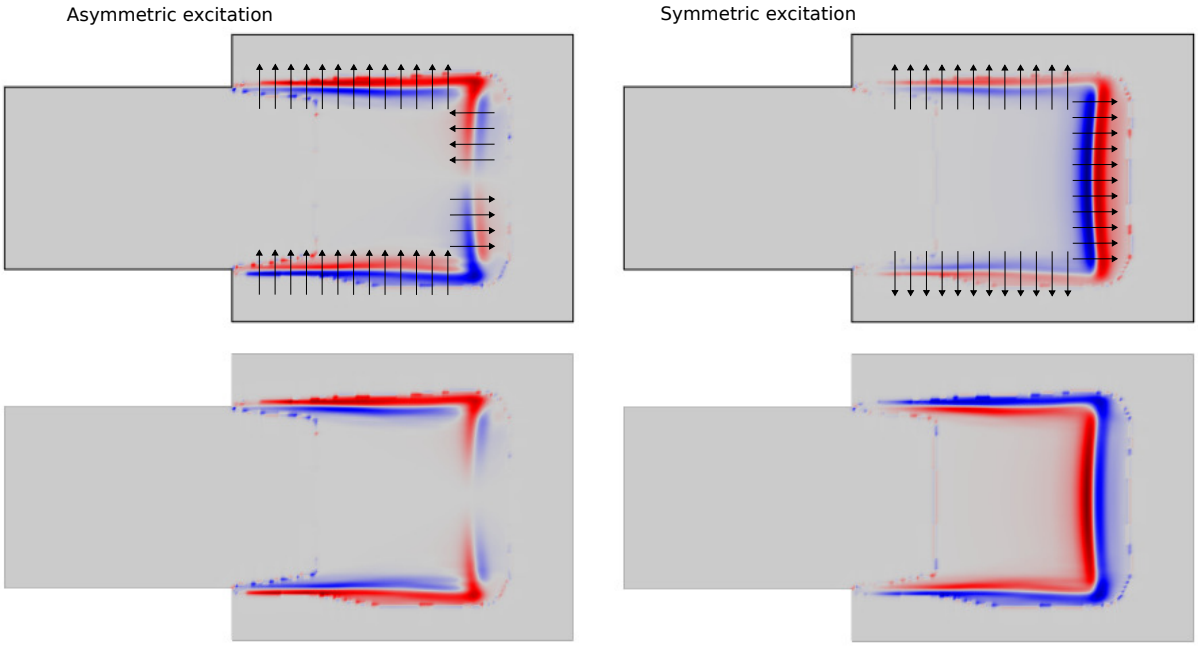

Figure 3.13: Real part of the fluctuating heat-release rate at the top and the RI distribution at the bottom computed with the LRF_{EF} at 2500 Hz. Positive values are colored in red, negative values in blue. Black arrows show the corresponding flame motion.

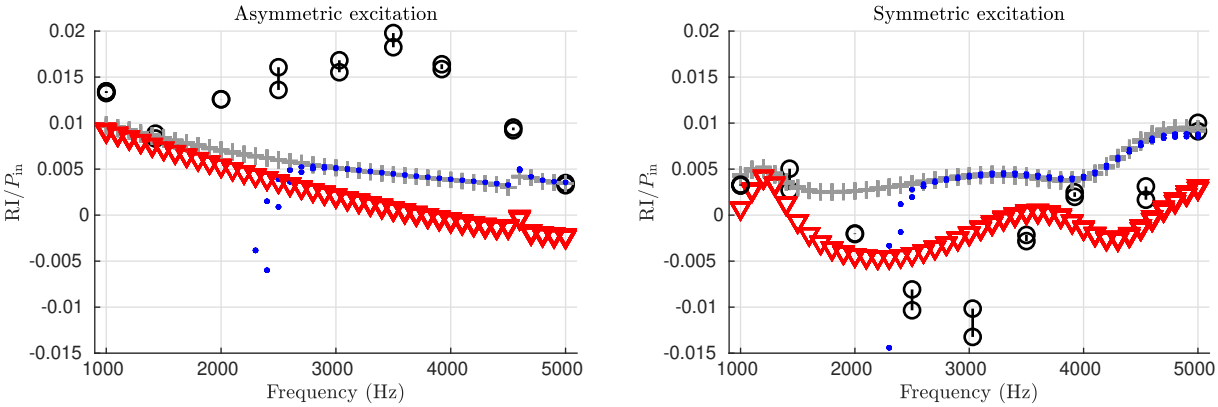

Figure 3.14: Normalized Rayleigh index in the top and bottom halves of the combustor mid-plane computed in the LES (○), with the LRF_{EF} (+), LRF_{ZS} (▽), and $\mathrm{LRF}_{EF,u}$ with the mean flow (·).

E-FLAME (LRF_{EF}) and ZS (LRF_{ZS}) models is shown in Fig. 3.14. The LRF_{EF} (+) always yields a positive RI, as mentioned in Section 2.1.6. It hits the LES results at frequencies below 2000 Hz and above 4500 Hz. Hence, the assumption of no fluctuation of the mass-specific reaction rate ($\dot{\mathfrak{w}}'_c = 0$) is appropriate in this frequency range. Nevertheless, the LRF_{EF} can not reproduce the peaks in RI around 3500 Hz (asymmetric excitation) and 3000 Hz (symmetric excitations). This behavior might be due to a weak T1 mode present in the LES, but nearly perfectly damped in the linear solver. Another reason might be a lack of a proper model for $\dot{\mathfrak{w}}'_c$. It appears that the LRF_{ZS} (▽) outperforms the LRF_{EF} at some frequencies for the symmetric excitation, but overall it is inferior to the LRF_{EF}. Furthermore, the LRF_{ZS} shows a negative RI for the asymmetric excitation at high frequencies, which is completely wrong. Fig. 3.14 shows

an additional data set that belongs to the $\mathrm{LRF}_{EF,u}$ that accounts for the convective effects $(\cdot)$. Strictly speaking, the E-FLAME is not valid with non-zero mean flow. However, this artificial model can show at which frequencies the velocity fluctuations lose their convective properties and become dominated solely by acoustics, so the mean flow can be safely neglected. This happens at frequencies higher than 2500 Hz when both LRF_{EF} and $\mathrm{LRF}_{EF,u}$ yield the same results.

A further investigation of the LRF_{EF} shows that the assumption of an isentropic flow (neglecting viscosity and heat conduction) does not change the resulting RI. The viscous energy dissipation and the heat transfer are negligible at high frequencies, in contrast to the low-frequency regime (see PAPER-LRF). Hence, the linearized flow equations can be simplified to the Helmholtz equation[6] that drastically reduces the degrees of freedom:

$$\frac{1}{\overline{\gamma p}}\frac{\partial^2 p'}{\partial t^2} - \frac{\partial}{\partial x_i}\left(\frac{1}{\overline{\rho}}\frac{\partial p'}{\partial x_i}\right) = \frac{\overline{\gamma}-1}{\overline{\gamma p}}\frac{\partial \dot{\omega}'_q}{\partial t}. \tag{3.6}$$

3.2.4 Conclusion and Outlook

Three linear flame models are applied to study the high-frequency flame response in a generic reheat combustor: the LRF solver, the linear flow solver with the SZ and E-FLAME models. The auto-ignition flame is transversely excited in the LES (reference data) and in the linear simulations. The energy, supplied to the system by the excitation, is estimated using the Rayleigh index. The LRF results do not agree at all with the LES results. The current formulation of the LRF has a problem in the source term for the progress variable, more precisely in the derivative $[d\dot{\omega}_c/dY_c]^{tab}$ and $\left[d\dot{\omega}_q/dY_c\right]^{tab}$. The LRF approach has been validated in paper PAPER-LRF with the Arrhenius approach, but the linearized tabulation has never been applied before, especially for d̈ifficultc̈ases such as turbulent auto-ignition flames. Some strategies to fix the problem will be provided as outlook in the end of this section.

Considering the SZ and E-FLAME models, both models show the correct trend but fit the LES results only partially. The E-FLAME shows somewhat better results than the SZ model. Even though the straightforward application of the LRF to a high-frequency response of the auto-ignition flame failed, a significant result is achieved. The E-FLAME is analytically verified within the *linearized reactive flow* concept, giving more credit to the E-FLAME model than to the SZ model. The latter model has an arguable derivation using a moving frame. Therefore it is suggested to use the E-FLAME to obtain the first stability estimates, until the LRF is not adjusted to handle auto-ignition turbulent flames in the high-frequency regime. For more precise stability analysis, the large-eddy simulations are still required.

To adopt the LRF for high the auto-ignition flames at high-frequencies, a deep revision of the method is required. The problem is identified down to derivatives $[d\dot{\omega}_c/dY_c]^{tab}$ and $\left[d\dot{\omega}_q/dY_c\right]^{tab}$. Maybe, a volume-integration or some kind of filtering can be applied in order to create a derivative-free formulation. Another reason for the LRF failure can lie in the nature of the auto-ignition flame: the linearization might simply not work for this type of flames. To prove this hypothesis a more academic setup should be investigated. Furthermore, the LRF

[6] The same simplification applies to the LRF_{ZS} as well.

approach should be applied to turbulent aerodynamically-stabilized flames. One can start with the BRS burner [60, 105]. Recently, the present author accurately predicted the low-frequency flame dynamics for this burner using the tabulated chemistry approach [8]. The high-frequency instabilities of a swirl-Stabilized flame can be investigated in the test rig of Schwing and Sattelmayer [96].

There is also one important technical aspect of the LRF-solver that has to be improved in the future. The LRF solver has been applied only to quasi-two-dimensional problems because switching to 3D requires more computational resources (computation time and RAM). Hence to study 3D problems, an appropriate iterative solver with low RAM requirements has to be found. Gargouri has done preliminary work in this direction in his Bachelor's thesis [39], supervised by the present author.

4 Applications of the NIPCE

4.1 PAPER-UQ-STABILITY: Uncertainty quantification and sensitivity analysis of thermoacoustic stability with non-intrusive polynomial chaos expansion

Label: PAPER-UQ-STABILITY

Summary: This paper successfully demonstrates the application of the NIPCE to UQ and sensitivity analysis in thermoacoustics. It shows how to propagate uncertainties in the operating conditions to the growth rate of the most dominant mode. The NIPCE is validated against a Monte Carlo simulation. The NIPCE is able to predict the analytical moments of the growth-rate uncertainty and construct the probability density function of the growth rate. The knowledge of the PDF allows computing probabilities, for instance, the probability of instability. Moreover, the sensitivity analysis is performed using a derivative-based approach to identify the most dominant uncertain parameters.

The other important aspect, shown in this paper, is the NIPCE applicability to expensive CFD computations. The NIPCE is fully capable of solving such problems in reasonable time, but only if the number of uncertain parameters remains small.

Contribution: The present author introduced the concept of the paper and performed all corresponding computations. W. Polifke and C. Silva refined the concept of the paper and contributed a critical revision. S. Jeansch contributed the setup for the CFD simulations and the thermoacoustic network model. M. Češnovar developed a MATLAB tool to compute the NIPCE. The present author and W. Polifke wrote the rebuttal to the reviewers' comments and implemented the comments into the manuscript.

Status: Published in Combustion and Flame journal.

Review process: Peer-reviewed

Reference: A. Avdonin, S. Jaensch, C. F. Silva, M. Češnovar, and W. Polifke. "Uncertainty Quantification and Sensitivity Analysis of Thermoacoustic Stability with Non-Intrusive Polynomial Chaos Expansion." Combustion and Flame 189 (March 2018): 300-310. https://doi.org/10.1016/j.combustflame.2017.11.001.

4.2 PAPER-UQ-FTF: Quantification of the impact of uncertainties in operating conditions on the flame transfer function with non-intrusive polynomial chaos expansion

Label: PAPER-UQ-FTF

Summary: This paper continues the study, performed in PAPER-UQ-STABILITY, and investigates a more complex case with several correlated outputs. The NIPCE propagates the uncertainties from the operating conditions to the flame transfer function that is identified in terms of the finite impulse response and consists of a set of correlated coefficients. PAPER-UQ-FTF neglects the uncertainties in the FIR coming from the identification procedure. How to account both, uncertainties from the operating conditions and the identification process, should be addressed in future studies.

Besides the UQ, this paper introduces a derivative-free sensitivity analysis using Sobol indices that suits better to identify the most dominant uncertain parameters than the derivative-based method from PAPER-UQ-STABILITY.

Contribution: The present author developed the concept of the paper and performed all corresponding computations. W. Polifke refined the concept and contributed a critical revision of the paper. The present author and W. Polifke wrote the rebuttal to the reviewers' comments and implemented the comments into the manuscript.

Status: Presented at ASME Turbo Expo 2018 Turbomachinery Technical Conference and Exposition, published in proceedings of ASME and in The Journal of Engineering for Gas Turbines and Power.

Review process: Peer-reviewed

References: 1) A. Avdonin, and W. Polifke. "Quantification of the Impact of Uncertainties in Operating Conditions on the Flame Transfer Function with Non-Intrusive Polynomial Chaos Expansion." In Proceedings of ASME Turbo Expo 2018: Turbomachinery Technical Conference and Exposition. GT2018-75476. Lillestrom, Norway: ASME, 2018.

2) A. Avdonin, and W. Polifke. "Quantification of the Impact of Uncertainties in Operating Conditions on the Flame Transfer Function with Non-Intrusive Polynomial Chaos Expansion." J. Eng. Gas Turbines and Power, GTP-18-1364, 141, no. 1 (2019): 011020. https://doi.org/10.1115/1.4040745.

5 Contextualization and discussion of publications

Local modeling of the flame response

PAPER-LRF suggests the *linearized reactive flow* approach for the local flame modeling. This approach inherits the linear flame dynamics by design and creates a linear relationship between multiple plausible inputs and multiple outputs. The LRF shows a massive potential on an example of a laminar flame at low frequencies: it captures the convective disturbance of the flame front, solves for eigenmodes, computes the flame response to perturbations of the velocity or equivalence ratio. The current state of the art in linear stability analysis at low frequencies is applying low-order thermoacoustic network models [31, 33, 88]. This method is fast but not very accurate. To increase the modeling accuracy, it is recommended to use the linearized Navier-Stokes equations [67]. Anyway, both methods require coupling with the external global FTF, measured in an experiment or identified from a CFD simulation with a broadband excitation [41, 88, 105]. Running an unsteady CFD simulation for the FTF identification is computationally expensive. When the validation of the LRF succeeds for industry-relevant flames such as turbulent propagating/diffusion flames, the LRF might be applied for the linear thermoacoustic stability analysis at low frequencies, skipping the step of the FTF identification. That will make the linear stability analysis drastically faster. Now, the application of the LRF is still limited to fundamental studies of laminar flames, e.g. entropy generation [68].

At high frequencies, there is no established technique to predict linear thermoacoustic stability behavior. The brute-force approach is a CFD simulation of the combustion system, e. g. LES that directly resolves the flow field oscillations. However, LES is so computationally expensive that any parametric study is unfeasible. Another way is applying a linear solver such as the Helmholtz solver coupled with a local flame transfer function. The Helmholtz solver requires the mean fields, so a single LES is still needed. The most straightforward local flame transfer function is a $n-\tau$ model with azimuthal reference velocity [40]. This approach is not convenient since there is no analytical/empirical way to estimate the parameters n and τ. Hence, they have to be approximated from the LES of a self-excited oscillation, and, most probably, they depend on the type of the eigenmode and the load point of the combustor. There are two other local modeling approaches for high frequencies: the *Zellhuber-Schwing* model [12, 13, 53, 96, 114] and the *Eulerian Flame Acoustic Motion Equation* [70]. Both models capture the linear flame motion, but they do not take into account fluctuations in chemical consumption rates. This drawback motivates the application of the LRF approach, since it inherits the complete linearized flame dynamics by design. Unfortunately, the straightforward application of the LRF, as it is, to a complex problem – transverse oscillations of a turbulent auto-ignition flame – failed. The results did not agree at all with the CFD results. Nevertheless, a significant result is achieved: the E-FLAME is analytically verified within the *linearized reactive flow* concept.

This work encourages the application of the E-FLAME to model the local flame response at high frequencies, as long as the source term of the progress variable in the LRF is not adjusted to handle auto-ignition turbulent flames in the high-frequency regime. A Helmholtz solver with the E-FLAME can make the first stability estimates, but large-eddy simulations are still required for more precise statements.

Uncertainty quantification and sensitivity analysis of the flame response

There are two publications, PAPER-UQ-STABILITY and PAPER-UQ-FTF, that cover the application of the NIPCE for UQ and sensitivity analysis of flames in a low-frequency regime. The main focus of both publications is schematically shown in a typical workflow of a low-frequency thermoacoustic analysis, see Fig. 5.1. PAPER-UQ-STABILITY answers the general

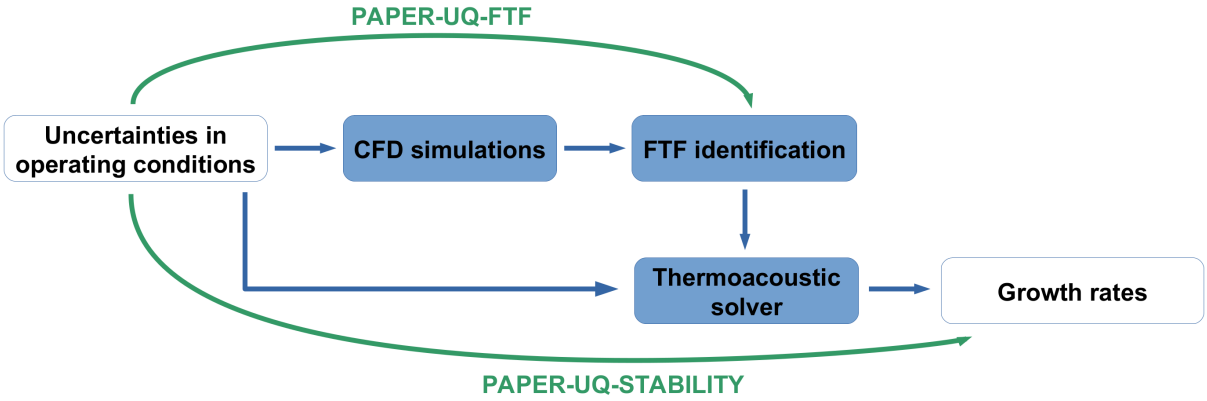

Figure 5.1: Applications of the NIPCE on an example of a typical workflow of a low-frequency thermoacoustic analysis.

question how to propagate uncertainties from operating conditions to the final quantity of interest (the growth rate of the dominant thermoacoustic mode) and introduces the basics of sensitivity analysis. Whereas the second paper solves more challenging tasks: it considers multiple correlated outputs and performs sensitivity analysis using Sobol indices on an example of uncertainty in the flame transfer function. Finally, both papers indicate that instead of doing a single CFD simulation and waiving the UQ, it is worth doing several CFD simulations and estimating the uncertainty of a quantity of interest using the NIPCE. Due to time constraints, uncertainty quantification and sensitivity analysis are not performed for high-frequency instabilities in this thesis. When switching to high frequencies, the proposed NIPCE workflow remains the same, so there will be no novelty therein.

The most common methods for UQ in thermoacoustics, besides the Monte Carlo simulation, are the active subspace [9, 25, 44] and adjoint method [69, 100]. The active subspace reduces the number of uncertain parameters to few active variables. Then the combustor is approximated by a low-order surrogate model. The adjoint method uses direct and adjoint eigenvectors to construct a truncated Taylor expansion of the combustor. NIPCE is not a competitor to the methods mentioned above but rather a complementary tool to solve problems where neither active subspace nor adjoints are feasible. For instance, if access to solver state-matrices is impossible, then the adjoint method cannot be employed. On the contrary, NIPCE can easily be applied here, since it treats the solver as a black box. If a single system evaluation is so expensive that the random sampling required to identify the active subspace is impractical, then NIPCE

with Gauss quadrature still solves the problem since the method requires only a few quadrature points. Just keep in mind the main constraint of the method – the number of uncertain parameters should be low (less than five).

There might be one competitor to the NIPCE in the future – the Gaussian process introduced recently to the thermoacoustic community [46–48] that also treats the system under investigation as a black box. It uses a machine learning technique to predict the output, so the samples are chosen intelligently, probably resulting in a smaller sample number to get converged statistics than using the NIPCE. Furthermore, the Gaussian process exploits correlations between low- and high-accuracy data to enhance its learning efficiency [49]. However, the Gaussian process has not been applied to truly computationally expensive cases, where a Monte Carlo validation is no longer possible. When such studies appear, it will be clear which method is superior, the NIPCE or the Gaussian process.

Besides the NIPCE with all its benefits, this thesis reveals a very useful method for sensitivity analysis – the Sobol indices that represent a formal way to quantify the contribution of each uncertain input parameter to the output uncertainty. It is a promising approach that has never been used before in thermoacoustics and will find acknowledgment in the coming years. For instance, the Sobol indices can be adopted for the Gaussian process.

Supervised Students

Student	Research
Tarek Benaziz	Master's thesis Adjoint sensitivity analysis of a 1D laminar flame [10] 01.12.2014-31.05.2015
Matic Češnovar	Term project Implementation of an uncertainty quantification tool in MATLAB [20] 23.5.2016-23.10.2016
Michael Bertsch	Term project Evaluation of impedance boundary conditions in ANSYS Fluent [14] 01.04.2017-30.09.2017
Alireza Javareshkian	Master's thesis Investigation of premixed turbulent flame dynamics by means of LES with stochastic fields and tabulated chemistry [55] 01.04.2017-30.09.2017
Tobias Bienieck	Master's thesis Comparative LES Study of Partially Premixed Sandia Flames Based on Alternative Progress Variable Definitions in the Context of the Flamelet/Progress Variable Combustion Model [16] 24.04.17-24.10.2017
Fares Gargouri	Bachelor's thesis Application of iterative solvers in themoacoustics [39] 01.05.2017-31.10.2017
Maximilian Kühn	Term project Linearized reactive flow with equivalence ratio perturbations [61] 15.05.2017-14.11.2017

Reproduction of Papers

This chapter reproduces the papers PAPER-LRF, PAPER-UQ-STABILITY, and PAPER-UQ-FTF.

During the work on the project COOREFLEX-Turbo 2.1.2c, the present author extended the combustion modeling approach of Kulkarni et al. [62–64] to a premixed, aerodynamically-stabilized flame and validated its flame dynamics against the experimental results. The results were presented by W. Polifke at ASME Turbo Expo 2020 Turbomachinery Technical Conference and Exposition and published in proceedings of ASME [7] and in The Journal of Engineering for Gas Turbines and Power [8]. Some of the project time was also spent investigating Basis Pursuit Denoising (BPDN) – a regression technique that minimizes the number of the input parameters. Initially, it was intended to use BPDN to identify the local flame response at high frequencies, but the time constraints did not allow pursuing this approach. Therefore, BPDN is out of the scope of this thesis. Nevertheless, a preliminary study of the laminar flame response to low-frequency excitations was performed by the present author and published in Report COOREFLEX-Turbo 2.1.2c [6]. The latter two publications have only limited relevance for the topic of the present thesis, so they are not reproduced in the following.

Available online at www.sciencedirect.com

ScienceDirect

Proceedings of the Combustion Institute 37 (2019) 5307–5314

Proceedings of the Combustion Institute

www.elsevier.com/locate/proci

Thermoacoustic analysis of a laminar premixed flame using a linearized reactive flow solver

Alexander Avdonin*, Max Meindl, Wolfgang Polifke

Technical University of Munich, D-85747 Garching, Germany

Received 1 December 2017; accepted 18 June 2018
Available online 2 July 2018

Abstract

In this paper, the dynamics and thermoacoustic stability of a laminar premixed flame are analyzed using a linearized reactive flow (LRF) solver. The LRF solver is based on linearized compressible Navier-Stokes and reacting species transport equations and thereby includes a model for the dynamic response of the flame to flow perturbations in an inherent manner. The equations are discretized using the discontinuous Galerkin finite element method. By way of example, thermoacoustic characteristics of attached and lifted laminar premixed flames are investigated. First, the respective flame transfer functions (FTFs) are computed in the frequency domain with the LRF solver. The results are in agreement with reference FTFs identified from CFD time-series. Secondly, the LRF solver is employed for thermoacoustic stability analysis, i.e. computation of shape, frequency, and growth rate of eigenmodes. Results are compared to established hybrid methods that couple FTFs with a low-order thermoacoustic network-model or a linearized Navier-Stokes equations solver. All solvers capture the dominant thermoacoustic mode, but only the LRF resolves local flow-flame interaction, revealing e.g. the onset of the flame movement and the propagation of distortions along the flame.

Keywords: Thermoacoustics; Combustion dynamics; Discontinuous Galerkin finite element method; Linearized reacting flow; Linearized Arrhenius equation

1. Introduction

Modern, low-emission gas turbines are prone to thermoacoustic instabilities, which originate from a feedback between unsteady heat release and acoustics. It is essential to study thermoacoustic coupling mechanisms and to develop reliable tools for thermoacoustic analysis.

Prediction of thermoacoustic instabilities by means of high-fidelity simulations of the compressible reacting flow requires very considerable computational resources. Large-Eddy Simulation (LES) of a gas turbine combustor, say, may be unaffordable for industrial purposes. To reduce the problem size, a variety of modeling assumptions may be invoked to formulate *hybrid approaches*, which typically couple a model for the

* Corresponding author.
E-mail address: avdonin@tfd.mw.tum.de (A. Avdonin).

https://doi.org/10.1016/j.proci.2018.06.142

propagation and dissipation of acoustic waves with a flame transfer function (FTF). The FTF describes a flow-flame interaction and relates fluctuations of the global heat release rate to velocity fluctuations at a reference point upstream of the flame. Flame transfer functions can be derived analytically or obtained from experiments or CFD simulations, see for instance [1–3].

Thermoacoustic network-models (TNMs) represent a very popular, low-order hybrid approach. A TNM represents a combustor as a conjunction of elements, such as ducts and area jumps. Acoustic waves propagate through the resulting network of elements. The heat release fluctuations are modeled using an FTF and produce acoustic perturbations according to the linearized Rankine–Hugoniot jump conditions [4].

Due to increasing computing power and improved numerical algorithms, it has become possible to resolve the acoustic field in a combustor in two or three dimensions with the Helmholtz [5], the linearized Euler [6] or the *linearized Navier–Stokes equations* (LNSE) [7,8]. The spatial resolution of the mean and fluctuating flow field variables allows to investigate complex geometries and can yield an accurate prediction of dissipative effects. These approaches should also be categorized as hybrid models, as the flow-flame interaction is represented by an FTF.

Despite increased efforts to scrutinize nonlinear aspects of combustion dynamics [9], linear analysis remains extremely useful and important for fundamental studies of flow-flame-interaction mechanisms, for sensitivity or uncertainty analysis, for optimization, and for industrial application. This motivates the quest for more efficient, more accurate and more widely applicable methods for linear thermoacoustic stability analysis.

In this paper, we suggest an approach with an inherent description of the flame dynamics. Specifically, we analytically linearize the Navier-Stokes and reacting species transport equations to obtain *linearized reactive flow* (LRF) equations. With such a monolithic formulation, the linear flame dynamics is by design inherited from the governing equations; an external FTF is not required. The LRF equations are discretized using the discontinuous Galerkin finite element method. The LRF solver requires a CFD simulation to obtain mean fields, but no additional unsteady CFD simulations are needed to identify the FTF.

The works by van Kampen et al. [10] on the response of a premixed flame to fluctuations of equivalence ratio and by Blanchard et al. [11] on the effects of flow disturbances on the flame (and vice versa) may be regarded as precursors of the LRF approach. Those studies employ a numerical linearization of the governing equations and compute the flame transfer functions by simulating the step response in the time domain. In contrast, the LRF equations are derived analytically and the solver operates in the frequency domain, which allows to compute the FTF as well as thermoacoustic eigenmodes with high accuracy and efficiency.

The present paper introduces the LRF solver and verifies results by comparison with established hybrid approaches. By way of example, we study the flame dynamics and the dominant thermoacoustic eigenmodes of attached as well as lifted, compact, laminar, premixed flames. The full potential of the method - e.g. for non-compact flames - shall be exploited in further studies.

The paper is structured as follows: in the next section, we introduce the LRF and the two hybrid approaches, TNM and LNSE. Afterwards, we compare the FTFs computed by the LRF solver and deduced from CFD simulations, respectively, for two flame configurations. Then we compute and compare the dominant thermoacoustic eigenmodes. The paper closes with conclusions and an outlook for further investigations.

2. Linearized reacting flow

2.1. Nonlinear governing equations

Both the OpenFOAM solver , which computes the mean flow fields and the reference FTF, and the LRF solver are based on the nonlinear reactive flow equations:

$$\frac{\partial \rho}{\partial t} + \frac{\partial \rho u_j}{\partial x_j} = 0, \tag{1}$$

$$\frac{\partial \rho u_i}{\partial t} + \frac{\partial \rho u_i u_j}{\partial x_j} = -\frac{\partial p}{\partial x_i} + \frac{\partial \tau_{ij}}{\partial x_j}, \tag{2}$$

$$\frac{\partial}{\partial t}(\rho h - p) + \frac{\partial \rho u_j h}{\partial x_j} = \frac{\partial}{\partial x_j}\left(\alpha \frac{\partial h}{\partial x_j}\right) + \dot{\omega}_T, \tag{3}$$

$$\frac{\partial \rho Y_k}{\partial t} + \frac{\partial \rho u_j Y_k}{\partial x_j} = \frac{\partial}{\partial x_j}\left(D \frac{\partial Y_k}{\partial x_j}\right) + \dot{\omega}_i. \tag{4}$$

Variables ρ, u_i, and Y_k denote density, velocity component in the i-direction, and mass fraction of the species k. The viscous term is neglected in the conservation equation (3) for the sensible enthalpy h. The heat flux is approximated by $-\alpha\left(\partial h/\partial x_j\right)$ instead of Fourier's law[1], which is commonly done when the energy equation is written in terms of the sensible enthalpy. The sensible enthalpy for the species k is calculated from JANAF polynomials with coefficients a_j:

$$h_k(T) = \int_{T_{ref}}^{T} c_{p,k} d\tilde{T} = R_k \sum_{j=1}^{5} a_j \frac{T^j - T_{\text{ref}}^j}{j}, \tag{5}$$

[1] In this study we follow the OpenFOAM definitions of the thermal and mass diffusivities, α and D, with SI units kg/(ms).

with the specific gas constant R_k for the species k. The sensible enthalpy of the mixture is computed using the species mass fractions: $h = \sum_k h_k Y_k$. The viscous stress tensor τ_{ij} reads:

$$\tau_{ij} = \mu\left(\frac{\partial u_i}{\partial x_j} + \frac{\partial u_j}{\partial x_i}\right) - \frac{2}{3}\mu\frac{\partial u_l}{\partial x_l}\delta_{ij}, \tag{6}$$

where δ_{ij} is the Kronecker delta. The pressure p, the density ρ, and the temperature T are linked by the ideal gas law: $p = \rho RT$. The dynamic viscosity μ is given by Sutherland's law: $\mu = A_s T^{1/2}/(1 + T_S/T)$ with $A_s = 1.67212 \cdot 10^{-6}$ kg/(msK$^{1/2}$) and $T_S = 170.672$ K. To determine thermal diffusivity α a constant Prandtl number $\mathrm{Pr} = \mu/\alpha = 0.71$ is assumed. Similarly, with unity Lewis number for all species, Schmidt number Sc and mass diffusivity D[2] obey $\mathrm{Sc} = \mu/D = 0.71$.

We model the methane-air combustion using a one-step Westbrook and Dryer [12] chemistry mechanism with a progress rate $\mathcal{Q}$:

$$\mathcal{Q} = A\rho^{a+b}\frac{Y_{O_2}^a Y_{CH_4}^b}{W_{O_2}^a W_{CH_4}^b}\exp\left(-\frac{E_a}{TR_{\mathrm{univ}}}\right), \tag{7}$$

with $A = 6.7 \times 10^{12}$ cgs units, $E_a = 48.4$ kcal/mol, $R_{\mathrm{univ}} = 1.987 \times 10^3$ kcal/(molK), $a = 1.3$ and $b = 0.2$.

The methane consumption rate is $\dot{\omega}_{\mathrm{CH_4}} = -W_{\mathrm{CH_4}}\mathcal{Q}$ and the heat release rate is $\dot{\omega}_T = \Delta h^\circ \mathcal{Q}$, where $W_{\mathrm{CH_4}}$ is the molar mass of methane and Δh° is the standard enthalpy of reaction.

2.2. Linearized governing equations

We split field variables into time-averaged and fluctuating parts, indicated by the overline and the prime, respectively. Linearization of equations (1)–(4) yields:

$$\frac{\partial \rho'}{\partial t} + \frac{\partial}{\partial x_j}\left(\overline{\rho}u_j' + \rho'\overline{u}_j\right) = 0, \tag{8}$$

$$\frac{\partial}{\partial t}\left(\overline{\rho}u_i' + \rho'\overline{u}_i\right) + \frac{\partial}{\partial x_j}\left(\overline{\rho}\overline{u}_i u_j' + \overline{\rho}u_i'\overline{u}_j + \rho'\overline{u}_i\overline{u}_j\right) = -\frac{\partial p'}{\partial x_i} + \frac{\partial \tau_{ij}'}{\partial x_j}, \tag{9}$$

$$\frac{\partial}{\partial t}\left(\overline{\rho}h' + \rho'\overline{h} - p'\right) + \frac{\partial}{\partial x_j}\left(\overline{\rho}\overline{u}_j h' + \overline{\rho}u_j'\overline{h} + \rho'\overline{u}_j\overline{h}\right) = \frac{\partial}{\partial x_j}\left(\overline{\alpha}\frac{\partial h'}{\partial x_j} + \alpha'\frac{\partial \overline{h}}{\partial x_j}\right) + \dot{\omega}_T', \tag{10}$$

$$\frac{\partial}{\partial t}\left(\overline{\rho}Y_k' + \rho'\overline{Y}_k\right) + \frac{\partial}{\partial x_j}\left(\overline{\rho}\overline{u}_j Y_k' + \overline{\rho}u_j'\overline{Y}_k + \rho'\overline{u}_j\overline{Y}_k\right) = \frac{\partial}{\partial x_j}\left(\overline{D}\frac{\partial Y_k'}{\partial x_j} + D'\frac{\partial \overline{Y}_k}{\partial x_j}\right) + \dot{\omega}_k'. \tag{11}$$

Note that the enthalpy equation cannot be reduced to the pressure equation because c_p is not constant, see Eq. (5). Furthermore,

$$\tau_{ij}' = -\frac{2}{3}\delta_{ij}\left(\overline{\mu}\frac{\partial u_l'}{\partial x_l} + \mu'\frac{\partial \overline{u}_l}{\partial x_l}\right) + \overline{\mu}\left(\frac{\partial u_i'}{\partial x_j} + \frac{\partial u_j'}{\partial x_i}\right) + \mu'\left(\frac{\partial \overline{u}_i}{\partial x_j} + \frac{\partial \overline{u}_j}{\partial x_i}\right),$$

$$\mu' = \overline{\mu}\frac{\overline{T} + 3T_S}{2(\overline{T} + T_S)}\frac{T'}{\overline{T}}, \quad h' = \overline{c}_p T' + \sum_k \overline{h}_k Y_k',$$

$$\frac{T'}{\overline{T}} = \frac{p'}{\overline{p}} - \frac{\rho'}{\overline{\rho}},$$

$$\dot{\omega}_k' = \overline{\dot{\omega}}_k\left((a+b)\frac{\rho'}{\overline{\rho}} + \frac{T_a T'}{\overline{T}^2} + a\frac{Y_{O_2}'}{\overline{Y}_{O_2}} + b\frac{Y_{CH_4}'}{\overline{Y}_{CH_4}}\right),$$

D', α' and $\dot{\omega}_T'$ are computed in an analogous manner. Fuel mass fraction $\overline{Y}_{\mathrm{CH_4}}$ appears in the denominator of the equation for $\dot{\omega}_k'$, which can lead to numerical problems. Its value is thus limited to $\overline{Y}_{\mathrm{CH_4}} \geq \max(\overline{Y}_{\mathrm{CH_4}}) \times 10^{-4}$.

In this study, we consider premixed flames with the global one-step reaction. Thus, it suffices to transport a single species or a single progress variable. We choose to transport $Y_{\mathrm{CH_4}}'$; hence the mass-fraction of oxygen required for the computation of the reaction progress is given by $Y_{O_2}' = (2W_{O_2}/W_{\mathrm{CH_4}})Y_{\mathrm{CH_4}}'$. The remaining linearized field variables are p', ρ', and u_i'. For the sake of compactness, we avoid rewriting the linearized Eqs. (8)–(11) in terms of the selected linearized variables, it can be done without essential difficulty using the expressions provided above.

In closing this section we point out that in order to make the linearized equations fully consistent with the original nonlinear problem, first-order fluctuations of flow variables as well as material properties are retained. Note that the latter was crucial to achieve quantitative agreement with established methods (see below). Somewhat surprisingly, no sophisticated treatment of the strongly nonlinear Arrhenius term was required.

2.3. Discretization

The linearized reacting flow equations are discretized using the discontinuous Galerkin finite element method with a local Lax-Friedrichs flux formulation [13]. This method, which has proven to be robust for convectively-dominated problems, is an established method in CFD [14] and was adopted only recently for a hybrid thermoacoustic solver [8]. The discretization with linear ansatz functions

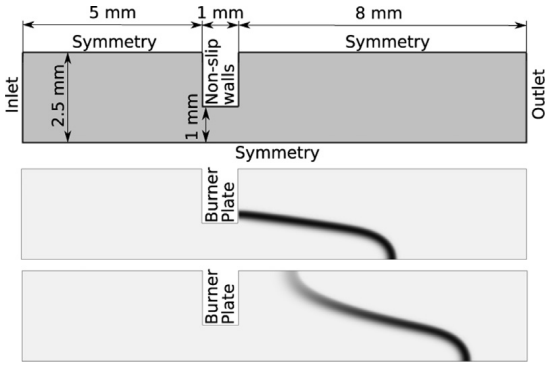

Fig. 1. Computational domain (top), mean heat release rate of the attached flame (middle) and of the lifted flame (bottom).

for all linearized variables is implemented in the commercial software COMSOL Multiphysics. The mean fields are provided by OpenFOAM simulations. The derivatives of the mean fields, such as $\partial\overline{u}_i/\partial x_j$, $\partial\overline{Y}_{CH_4}/\partial x_j$, and $\partial\overline{h}/\partial x_j$, are computed by the LRF solver internally.

In this study, the LRF solver computes the flame response in the frequency domain:

$$\hat{\dot{Q}} = \mathbf{C}(i\omega\mathbf{E} - \mathbf{A})^{-1}\mathbf{B}\hat{u}_{\text{ref}}, \tag{12}$$

where **A, B, C** and **E** are the system, input, output and mass matrices. Alternatively, the flame response may be deduced from a step response or broadband excitation in the time domain [3,15]. We solve for eigenvalues with an implicitly restarted Arnoldi algorithm [16]. All computations are performed with the direct parallel solver MUMPS [17].

3. Hybrid thermoacoustic models

The FTFs predicted by the LRF approach shall be verified by comparison with FTFs identified from CFD time-series, see Section 4.1 and [3,15]. Moreover, frequency and growth rate of the dominant thermoacoustic mode predicted by the LRF approach shall be compared to established hybrid approaches, which couple a model for the propagation and dissipation of acoustic waves with an FTF. In this section, the acoustic models are briefly described.

3.1. Thermoacoustic network-model

To represent the configurations under investigation (see Fig. 1), thermoacoustic network-models are built from simple elements such as ducts and sudden changes in cross-sectional area. The flame is assumed to be acoustically compact, so fluctuations of the global heat release rate $\dot{Q}'$ fully describe the flame dynamics and are related to the velocity fluctuations u'_{ref} at a reference point upstream of the flame through an FTF:

$$\frac{\hat{\dot{Q}}}{\overline{\dot{Q}}} = F(\omega)\frac{\hat{u}_{\text{ref}}}{\overline{u}_{\text{ref}}}, \tag{13}$$

where the circumflex denotes the complex fluctuation amplitude at frequency ω. The FTF is then coupled to the TNMs via linearized Rankine–Hugoniot jump conditions [4]. The network models are set up with the open source tool taX [18,19], which is based on a state-space formulation. The TNMs comprise no more than one thousand degrees of freedom; hence eigenvalues are computed within seconds. In the configuration investigated, the ducts are very short, so the corresponding viscous losses are negligible. Furthermore, loss coefficients at area jumps are not applied since semi-empirical approximations for the acoustic losses involve a high degree of uncertainty. Therefore, the reader should keep in mind that growth rates computed with the TNMs represent a worst-case result.

3.2. Linearized Navier–Stokes coupled with FTF

The hybrid model based on the linearized Navier-Stokes equations employs the same equations and discretization as the LRF, but without the transport equation for the fuel mass-fraction and the corresponding linearized reaction rate in the enthalpy equation. Instead, the unsteady heat release is represented by an FTF. The LNSE uses the same FTF as the TNM but additionally resolves the spatial extent of the flame. Thus, the fluctuating heat release rate results in a spatially distributed source term $\dot{\omega}'_T$. Following [5,8], we assume a distribution proportional to the local *mean* heat release rate:

$$\hat{\dot{\omega}}_T(\vec{x}) = \overline{\dot{\omega}}_T(\vec{x})F(\omega)\frac{\hat{u}_{\text{ref}}}{\overline{u}_{\text{ref}}}. \tag{14}$$

Using this formulation, the local fluctuations of the heat release rate are synchronized throughout the entire domain. This should be adequate for an acoustically compact flame, although it ignores any phase lag between the flame response at the root and the tip, say, and the consequential possibility of destructive interference.

Both the TNM and the LNSE models employed in this study employ a state-space formulation. The FTF is also converted to the state space representation and coupled with the acoustic system matrices, which yields a linear eigenvalue problem [8,19].

Note that the LNSE solver requires roughly 10% to 30% less computational resources than the LRF solver on the same mesh due to the reduced number of variables.

4. Investigation of a laminar premixed flame

4.1. Numerical setup

By way of example, we investigate a generic, laminar premixed flame that is stabilized on a slit as shown in Fig. 1 (top). Exploiting the symmetry along and across the slits reduces the simulation domain to one-half of the flame in two dimensions. If the burner plate is adiabatic, then the flame attaches to it, see Fig. 1 (middle). Setting a constant surface temperature $T_W = 375$ K at the burner plate results in a lifted flame as shown in Fig. 1 (bottom). The remaining flow parameters are identical for both configurations: the inlet velocity is 0.3 m/s, the equivalence ratio equals 0.8, the inlet temperature is 293 K, and the outlet pressure is 101325 Pa.

The CFD solver employs standard boundary conditions: isothermal inlet with fixed velocity and mixture, outlet with fixed static pressure, non-slip walls at the burner plate, symmetry at the top and bottom of the computational domain. A structured mesh with 53600 square cells of size of $\Delta x = 25\,\mu$m resolves the flame with 16 cells.

The LRF and LNSE solvers use corresponding linearized boundary conditions. Two meshes are used: a fine mesh that is identical to the CFD mesh, and a coarser mesh with $\Delta x = 40$ μm and 21100 cells (10 cells across the flame).

A flame transfer function as required for hybrid models is identified as a finite impulse response from time-series data generated by OpenFOAM simulations. A broadband velocity excitation with an amplitude of $0.05\overline{u}_{\text{inlet}}$ is imposed at the inlet. To ensure a robust simulation and reduce noise, a weakly compressible version of the reactive OpenFOAM solver is employed [20]. The CFL number is 0.1, and the simulation time is 0.15 s, which is sufficient for the accurate identification of the FTF in this study. The identification methodology is discussed in detail by Tay-Wo-Chong et al. [3] and Polifke [15]. The computation of the FTF is quite time consuming, since it requires a long time series for the identification process – typically 0.15 s to 0.3 s, which entails compute times of several days.

OpenFOAM simulations without excitation provide the flow parameters of the burnt and unburnt gas for the TNM as well as the mean fields for the LNSE and LRF. In these simulations, the CFL number was decreased to 0.01 to better resolve the chemical time scale and thus obtain a better flame-front resolution.

4.2. Flame transfer function

We use the inlet velocity of the computational domain as the reference velocity for the flame transfer functions, see Eq. (13).

The FTFs of the attached (left) and lifted (right) flames were identified from the OpenFOAM time-series with more than 95% accuracy, see Fig. 2. Due to a very high identification accuracy, the confidence intervals are negligibly small and therefore omitted. Both flames show a low-pass behavior. The lifted flame exhibits an excess gain at around 65 Hz, followed by a very rapid decline, such that its response is close to zero for frequencies above 200 Hz.

Figure 2 also shows the flame frequency responses computed by the LRF solver with two different meshes. For both the attached and lifted flames, the LRF solver yields similar results for mesh sizes $\Delta x = 40\,\mu$m and $25\,\mu$m, indicating discretization independence. Further reduction of the mesh size preserving the FTF quality is possible by coarsening the regions further away from the flame and the corners of the burner plate. In the following, we focus on results obtained on the fine mesh ($\Delta x = 25$ μm), which corresponds to the CFD mesh.

The LRF solver predicts the phase of the frequency response well. The gain of the frequency response is perfectly predicted for the attached flame and overestimated by up to 10% for the lifted flame. These results are achieved at significantly lower computational cost than running a transient CFD simulation for the FTF identification: 6 CPUh and 22 GB RAM for the computation of 16 frequency responses vs. 300 CPUh and 2Gb RAM for the CFD simulation on the same mesh. To reduce the RAM requirements, an iterative solver may be used – typically at the cost of longer computational time.

4.3. Thermoacoustic eigenmodes

In this section, we investigate the thermoacoustic eigenmodes and eigenvalues – i.e. frequencies and growth rates – of the two flame configurations. The simulation domain is very small (14 mm), such that acoustic cavity-modes can be found only at very high frequencies in the kHz range. Thus, we set the inlet and outlet boundaries to be nonreflecting and concentrate on intrinsic thermoacoustic (ITA) eigenmodes, which may be unstable for nonreflecting boundaries provided that the flame response is sufficiently strong [21,22]. Alternatively, impedance boundary conditions formulated as state space systems could be used, as suggested by Jaensch et al. [23]. The frequencies of ITA modes in an anechoic environment can be approximately determined by the "π criterion" [21]: *ITA modes may occur whenever the phase of the FTF is close to an odd multiple of* π. Inspecting Fig. 2, we see that ITA frequencies should be around 170 Hz for the attached flame and 100 Hz for the lifted flame.

Now, we compare predictions of the LRF solver with the two hybrid approaches described in Section 3. The TNM (○) and LNSE (▽) share the same FTF identified from CFD time-series as described in the previous subsection. All models predict the unstable thermoacoustic modes and yield

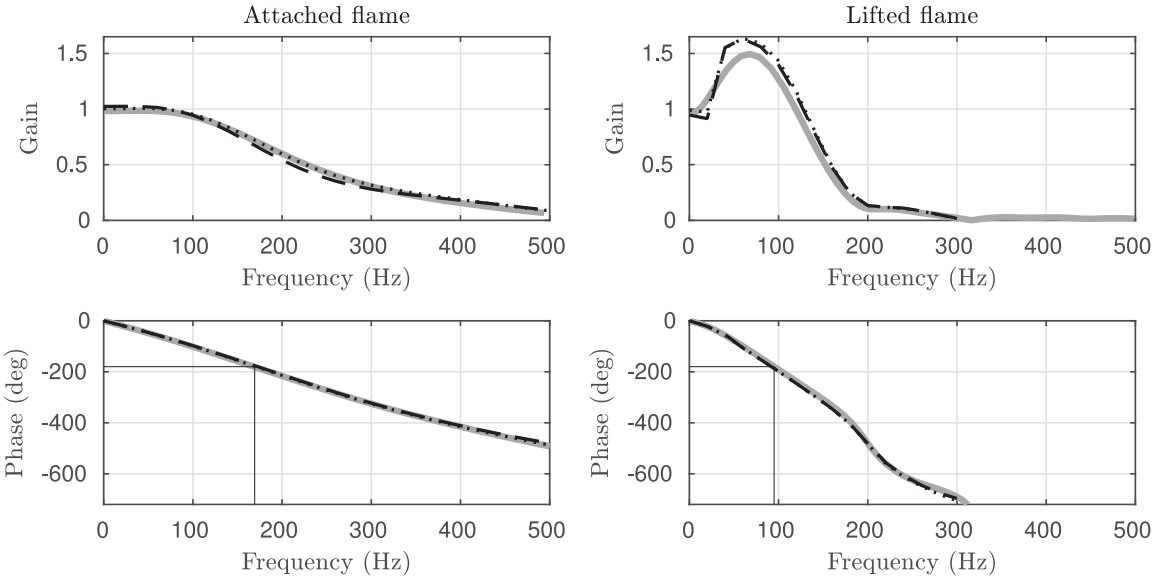

Fig. 2. Frequency response of the attached flame (left) and the lifted flame (right) identified using CFD time-series (—) and computed using the LRF solver with mesh sizes $\Delta x = 40$ µm (– –) and 25 µm (....). Thin black lines (—) visualize the π criterion for ITA modes.

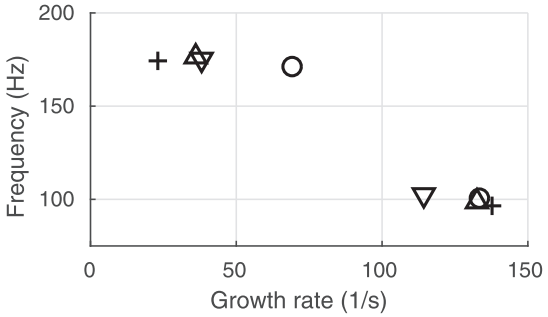

Fig. 3. Dominant thermoacoustic eigenvalues of the attached flame ($\approx$ 170 Hz) and the lifted flame ($\approx$ 100 Hz) predicted with LRF (+), LNSE with FTF_{LRF} ($\triangle$), LNSE ($\bigtriangledown$) and TNM ($\circ$) with FTF identified from CFD time-series.

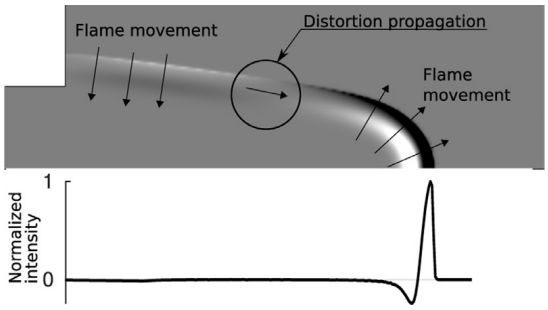

Fig. 4. Unstable eigenmode of the attached flame at 170 Hz: positive real part of the fluctuating heat release rate in black and negative in white at the top, its streamwise distribution at the bottom.

eigenfrequencies similar to the ones suggested by the π criterion.

The LRF solver requires most computational resources for the eigenvalue computation (0.4 CPUh and 22 GB RAM). The LNSE solver requires slightly less computational resources (0.4 CPUh and 18 GB RAM). The TNM solver computes eigenvalues within seconds due to the small number of degrees of freedom. Keep in mind, however, that even though the hybrid solvers are less costly than the LRF solver, they require to determine or measure an external FTF with considerable effort.

The LNSE as well as the LRF account for mean flow effects and allow for a linear energy transfer between acoustics, vorticity, and entropy waves. That results in a more accurate prediction of acoustic dissipation than using TNM and, typically, in smaller growth rates. The TNM ($\circ$) provides higher growth rates than the LNSE ($\bigtriangledown$), since the TNM neglects acoustic losses other than those associated with the nonreflecting in- and outlets.

The growth rates computed by the LRF (+) differ from those computed by the LNSE ($\bigtriangledown$). We offer two reasons for this discrepancy. Firstly, LRF slightly over-predicts the FTF gain of the lifted flame at its eigenfrequency, which should translate into an increase in growth rate [21].

Secondly, there are important differences in the modeling of flow-flame interactions by the LRF and LNSE. The LRF locally resolves the flow-flame interaction. This is demonstrated, for

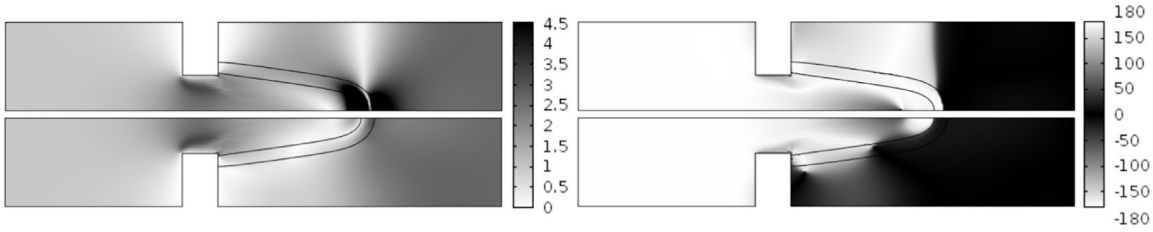

Fig. 5. Unstable eigenmode of the attached flame at 170 Hz: magnitude (left) and phase (right) of the fluctuating streamwise velocity normalized at the inlet for the LRF (top) and LNSE (bottom) models. Black lines indicate the mean flame position.

instance, for the attached flame[2] in Fig. 4. The figure shows the unstable mode at 170 Hz in terms of the real part of the fluctuating heat release rate. Only the flame tip yields a significant contribution to the global fluctuation of the heat release rate, since the local fluctuations upstream of the flame tip cancel out. The local fluctuations in heat release rate change from negative (white color) to positive (black) across the flame indicating the onset of the flame movement towards the burnt mixture (or vice versa). Furthermore, the LRF captures a distortion, initiated at the flame root and propagated downstream along the flame, changing the direction of the flame movement[3]

In contrast, the LNSE does not explicitly resolve the spatio-temporal evolution of flame movement and distortion along the length of the flame. Instead, the heat release rate fluctuation is synchronized along the length of the flame and is proportional to the mean heat release rate. Consequently, the fluctuating velocity fields that result from unsteady heat release differ for the LRF and LNSE formulations (see Fig. 5), which should contribute to the differences in predicted growth rates.

To facilitate further analysis, we introduce one additional model. We couple the LNSE with the flame transfer function that is computed using the linearized reactive flow solver[4] This new model is abbreviated as $\mathrm{LNSE_{LRF}}$. The LRF and $\mathrm{LNSE_{LRF}}$ share the same FTF, so these two models cannot show any discrepancies in their growth-rate predictions related to the gain of the FTF, but only related to the differences in the flow-flame modeling.

For the lifted flame, the growth rates provided by the LRF (+) and $\mathrm{LNSE_{LRF}}$ ($\triangle$) are in a much better agreement than those provided by the LRF (+) and LNSE ($\bigtriangledown$). Hence, the discrepancy between the LRF and LNSE originates mostly from the gain of the FTF at the eigenfrequency, which was overpredicted by the LRF.

For the attached flame, the gain of the FTF is perfectly captured by the LRF. Hence, the difference between the growth rates computed by the LRF (+) and LNSE ($\bigtriangledown$) is attributed solely to the differences in the flow-flame modeling.

5. Conclusion and outlook

This paper introduces a linearized reactive flow solver to analyze the flame dynamics of attached and lifted laminar premixed flames as well as their thermoacoustic stability. The LRF captures the dynamics of both flames quite well: the phase of the flame frequency response is accurately predicted, while its gain is very well predicted for the attached flame and only slightly overestimated for the lifted flame. The LRF solver also correctly predicts the dominant thermoacoustic modes and resolves the spatio-temporal evolution of the mode shapes, making explicit the local fluctuations of heat release, the onset of the flame movement, and the convective propagation of flame distortion. For the simplistic test cases considered here with compact, velocity-sensitive, premixed flames, established thermoacoustic models such as TNM and LNSE also capture the eigenmodes in terms of frequency and growth rate quite well, but they do not resolve local flow-flame interaction due to their coupling with a global FTF.

The LRF is a very promising approach because of its monolithic formulation with an inherent flow-flame-acoustic interaction. Admittedly, it is computationally more expensive than the LNSE approach due to one additional variable and possibly higher resolution in the flame region. On the other hand, the LRF approach does not require an external FTF, so an unsteady CFD simulation for the identification of the FTF is not required. The local flow-flame interaction resolved by the LRF is particularly important for the investigation of non-compact flames and/or non-plane acoustics, i.e. at higher frequencies, where a standard FTF that relates upstream velocity to overall heat release is inadequate [24–26]. Moreover,

[2] The detached flame shows a similar onset of movement.

[3] An animation of the propagating flame distortion is provided in supplementary materials.

[4] The $\mathrm{FTF_{LRF}}$ is fitted as a rational polynomial to a sampled frequency response and is valid over the entire frequency range.

configurations where fluctuations in equivalence ratio, pressure or temperature perturb the heat release require corresponding MISO or MIMO (multiple-input, single/multiple-output) formulations of hybrid models. In such cases, it is strictly speaking necessary to identify several flame transfer functions and couple them to an acoustic model, which can quickly become expensive and cumbersome. Conversely, LRF makes possible increased flexibility in the analysis of such systems: any combination of fluctuating variables may be chosen as "input" or "output", the respective transfer behavior or sensitivities may be studied in a MIMO framework with very favorable computational costs.

Future studies should extend the approach to turbulent, technically premixed flames at high frequencies and exploit advantages or identify limitations of the method.

Acknowledgments

The authors gratefully acknowledge funding provided by the German Federal Ministry for Economics and Energy (FKZ 03ET7021U) and GE Power. The investigations were conducted in the framework of the joint research program of AG Turbo (COOREFLEX-turbo 2.1.2c). The authors gratefully acknowledge the computational and data resources provided by the Leibniz Supercomputing Centre. We also thank Felix Schily for helping with the setup of network models in taX and Alp Albayrak for fruitful discussions about the LRF.

Supplementary material

Supplementary material associated with this article can be found, in the online version, at 10.1016/j.proci.2018.06.142

References

[1] L. Crocco, *J. Am. Rock. Soc.* (1951) 163–178.
[2] K. T. Kim, H. J. Lee, J. G. Lee, B. D. Quay, D. Santavicca (2009) 799–810. doi:10.1115/GT2009-60026.
[3] L. Tay-Wo-Chong, S. Bomberg, A. Ulhaq, T. Komarek, W. Polifke, *J. Eng. Gas Turbines Power* 134 (2) (2012) 021502–1–8, doi:10.1115/1.4004183.
[4] B.T. Chu, in: 4th Symposium (International) on Combustion, volume 4, Combustion Institute, Cambridge, Massachusetts, USA, 1953, pp. 603–612, doi:10.1016/S0082-0784(53)80081-0.
[5] F. Nicoud, L. Benoit, C. Sensiau, T. Poinsot, *AIAA J.* 45 (2) (2007) 426–441, doi:10.2514/1.24933.
[6] M. Zahn, M. Betz, M. Schulze, C. Hirsch, T. Sattelmayer (2017) V04AT04A081. doi:10.1115/GT2017-64238.
[7] J. Gikadi, T. Sattelmayer, A. Peschiulli, in: ASME Turbo Expo 2012: Turbine Technical Conference and Exposition, American Society of Mechanical Engineers, 2012, pp. 1203–1211.
[8] M. Meindl, A. Albayrak, W. Polifke, submitted to *J. Comput. Phys.* (2018).
[9] M.P. Juniper, R.I. Sujith, *Ann. Rev. Fluid Mech.* 50 (1) (2018) 661–689, doi:10.1146/annurev-fluid-122316-045125.
[10] J.F. van Kampen, J.B.W. Kok, T.H. van der Meer, *Int. J. Numer. Methods Fluids* 54 (9) (2007) 1131–1149, doi:10.1002/fld.1424.
[11] M. Blanchard, T. Schuller, D. Sipp, P.J. Schmid, *Phys. Fluids* 27 (4) (2015) 043602, doi:10.1063/1.4918672.
[12] C.K. Westbrook, F.L. Dryer, *Combust. Sci. Technol.* 27 (1–2) (1981) 31–43, doi:10.1080/00102208108946970.
[13] B. Cockburn, S.-Y. Lin, C.-W. Shu, *J. Comput. Phys.* 84 (1) (1989) 90–113, doi:10.1016/0021-9991(89)90183-6.
[14] B. Cockburn, G.E. Karniadakis, C.-W. Shu, in: Lecture Notes in Computational Science and Engineering, Springer, Berlin, Heidelberg, 2000, pp. 3–50, doi:10.1007/978-3-642-59721-3_1.
[15] W. Polifke, *Ann. Nuclear Energy* 67C (2014) 109–128, doi:10.1016/j.anucene.2013.10.037.
[16] R. Lehoucq, D. Sorensen, *SIAM J. Matrix Anal. Appl.* 17 (4) (1996) 789–821, doi:10.1137/S0895479895281484.
[17] P. R. Amestoy, I. S. Duff, J.-Y. L'Excellent, J. Koster, in: T. Sørevik, F. Manne, A. H. Gebremedhin, R. Moe (Eds.), Applied Parallel Computing. New Paradigms for HPC in Industry and Academia, number 1947 in Lecture Notes in Computer Science, Springer Berlin Heidelberg, 2000, pp. 121–130. doi:10.1007/3-540-70734-416.
[18] T. Emmert, S. Jaensch, C. Sovardi, W. Polifke, in: 7th Forum Acusticum, DEGA, Krakow, 2014.
[19] T. Emmert, M. Meindl, S. Jaensch, W. Polifke, *Acta Acust. United Acust.* 102 (5) (2016) 824–833, doi:10.3813/AAA.918997.
[20] S. Jaensch, M. Merk, E.A. Gopalakrishnan, et al., *Proc. Combust. Inst.* 36 (3) (2017) 3827–3834, doi:10.1016/j.proci.2016.08.006.
[21] M. Hoeijmakers, V. Kornilov, I. Lopez Arteaga, P. de Goey, H. Nijmeijer, *Combust. Flame* 161 (11) (2014) 2860–2867, doi:10.1016/j.combustflame.2014.05.009.
[22] C.F. Silva, T. Emmert, S. Jaensch, W. Polifke, *Combust. Flame* 162 (9) (2015) 3370–3378, doi:10.1016/j.combustflame.2015.06.003.
[23] S. Jaensch, C. Sovardi, W. Polifke, *J. Comput. Phys.* 314 (2016) 145–159, doi:10.1016/j.jcp.2016.03.010.
[24] M. Zellhuber, J. Schwing, B. Schuermans, T. Sattelmayer, W. Polifke, *Int. J. Spray Combust. Dyn.* 6 (2014) 1–34, doi:10.1260/1756-8277.6.1.1.
[25] T. Hummel, F. Berger, M. Hertweck, B. Schuermans, T. Sattelmayer, *J. Eng. Gas Turbines Power* 139 (7) (2017) 071502–071502–10, doi:10.1115/1.4035592.
[26] Y. Méry, *Combust. Flame* 192 (2018) 410–425, doi:10.1016/j.combustflame.2018.02.007.

Combustion and Flame 189 (2018) 300–310

Contents lists available at ScienceDirect

Combustion and Flame

journal homepage: www.elsevier.com/locate/combustflame

Uncertainty quantification and sensitivity analysis of thermoacoustic stability with non-intrusive polynomial chaos expansion

Alexander Avdonin*, Stefan Jaensch, Camilo F. Silva, Matic Češnovar, Wolfgang Polifke

Technische Universität München, Garching D-85747, Germany

ARTICLE INFO

Article history:
Received 13 July 2017
Revised 16 August 2017
Accepted 1 November 2017

Keywords:
Uncertainty quantification
Sensitivity analysis
Thermoacoustic instability
Thermoacoustics
Combustion dynamics
Polynomial chaos expansion

ABSTRACT

In this paper, non-intrusive polynomial chaos expansion (NIPCE) is used for forward uncertainty quantification and sensitivity analysis of thermoacoustic stability of two premixed flame configurations. The first configuration is a turbulent swirl combustor, modeled by the Helmholtz equation with an $n-\tau$ flame model. Uncertain input parameters are the gain and the time delay of the flame, as well as the magnitude and the phase of the outlet reflection coefficient. NIPCE is successfully validated against Monte Carlo simulation. It is observed that the first order expansion suffices to yield accurate results. The second configuration under investigation is a low order network model of a laminar slit burner, with the flame transfer function identified from weakly compressible CFD simulations of laminar reacting flow. Firstly the uncertainty and sensitivity of the growth rate due to three uncertain input parameters of the CFD model – i.e., flow velocity, burner plate temperature and equivalence ratio – are analyzed. A Monte Carlo simulation is no longer possible due to the computational cost of the CFD simulations. Secondly, two additional uncertain parameters are taken into account, i.e., the respective magnitudes of inlet and outlet reflection coefficients. This extension of the analysis does not entail a considerable increase in computational cost, since the additional parameters are included only in the low order network model. In both cases, the second order expansion is sufficient to model the uncertainties in growth rate.

1. Introduction

Thermoacoustics deals with a coupling between acoustics and heat release. This coupling may lead to a self-induced instability with excessive fluctuations in pressure, velocity, and temperature. Such instabilities occur, e.g., in gas turbines or rocket engines, where they can lead to a catastrophic system failure. To guarantee safety margins and normal operating conditions, the thermoacoustic behavior of a combustor should be studied. Indeed, a comprehensive thermoacoustic stability analysis is an important part of combustor design.

In computational analysis, boundary and operating conditions as well as model parameters of a system model are in general not known exactly, but instead are uncertain. Uncertainties propagate through the system model and affect the prediction of quantities of interest, making them uncertain. Forward *uncertainty quantification* (UQ) strives to characterize in a quantitative manner the impact of uncertain input or model parameters on the reliability of model predictions. An important aspect of the study of uncertainties is *sensitivity analysis*, which investigates the influence of each uncertain parameter on a quantity of interest. Sensitivity analysis helps to identify the most important uncertain parameters, which should be accounted for. Due to the fast development of data-driven methodologies in recent years, UQ and sensitivity analysis are becoming important topics in all engineering fields [1–5].

The main task of UQ in linear thermoacoustics stability analysis is to investigate how uncertainties in geometry, operating and boundary conditions as well as modeling parameters affect the growth rates of the thermoacoustics eigenmodes. Despite the fact that thermoacoustic systems are in general very sensitive to such uncertainties, until now only a small number of studies have been devoted to this topic, which shall be reviewed briefly in the following.

The most common and straightforward UQ method is Monte Carlo simulation [6]. The method numerically generates random samples of uncertain input parameters. For each sample, the quantity of interest is computed. The ensemble of obtained results is assumed to faithfully represent the variability of the quantity of interest. Monte Carlo simulation requires a large number of samples and is feasible only for system models with fast evaluation. If a single evaluation is computationally expensive, more sophisticated UQ methods are required. Fundamentally, there are two strategies to

* Corresponding author.
E-mail address: avdonin@tfd.mw.tum.de (A. Avdonin).

https://doi.org/10.1016/j.combustflame.2017.11.001
0010-2180/

overcome a high computational cost: (1) simplify the original system model to reduce the evaluation time, or (2) lower the number of samples required to achieve converged statistics. An example of the latter approach are smart sampling techniques, such as Latin hypercube sampling [7].

Bauerheim et al. [8] investigated a simplistic model of an annular combustor with 19 burners using a Helmholtz equation coupled with $n-\tau$ flame models. The uncertain input parameters were gain n and time lag τ of each single flame, resulting in a total of 38 uncertain parameters. The authors applied an active subspace approach [9] that reduced the 38 input parameters to three active variables. Fifty samples, i.e., model evaluations, were required to identify the active variables. Linear, quadratic and cubic reduced order algebraic models were fitted, using a few dozen samples. Finally, a Monte Carlo simulation was performed on the reduced order models to quantify the risk factor, i.e., the probability of an unstable state. The quadratic and cubic models showed accurate results in comparison to the original model. The active subspace approach is well suited for problems with a large number of uncertain parameters, since it eliminates the curse of dimensionality. However, in order to firstly identify active variables, and secondly fit a surrogate model, the method requires several tens or even hundreds of system evaluations.

Ndiaye et al. [10] also coupled a Helmholtz equation solver with an $n-\tau$ flame model in order to assess the thermoacoustic stability of a single premixed swirled burner. Again gain n and time lag τ were considered as uncertain parameters. Relying on a multiple linear regression technique, a bilinear algebraic surrogate model was tuned to reproduce growth rates of the dominant thermoacoustic mode, as predicted by the full model under variation of the uncertain parameters. Then the surrogate model was used to compute the risk factor with a Monte Carlo approach. The authors carefully assessed the number of full model evaluations required to tune the surrogate model and conclude that ten full model evaluations suffice to accurately estimate the risk factor.

Silva et al. [11,12] investigated the same swirled burner as Ndiaye et al. [10], considering four uncertain parameters, i.e., gain n and time lag τ of the flame model as well as magnitude and phase of the outlet reflection coefficient. Direct and adjoint eigenvectors were used to construct a first and second order expansions of the nonlinear eigenvalue problem around a reference eigenvalue. Using these expansions, deviations from the reference eigenvalue were computed at reduced computational cost. The results of the second order expansion were in good agreement with the ones obtained by solving the nonlinear eigenvalue problem. Recently, the same burner was investigated by Mensah et al. [13]. The authors used a flame transfer function fitted from the experiment instead of a n–τ flame model. The uncertainty in the flame transfer function was modeled with two parameters, relative error in gain and absolute error in phase, which were assumed to be constant in the entire frequency range. Magri et al. [14] used the adjoint approach in combination with the active subspace approach to compute the risk factor of the annular combustor investigated previously by Bauerheim et al. [8].

With the adjoint method one can easily build a reduced order model and compute sensitivities. One should keep in mind, however, that the accuracy of results will decrease with increasing variances in the input uncertainties, since the adjoint method constructs an expansion around a single reference point. Furthermore, the commonly used matrix-based method requires access to the state matrices, which may require substantial effort, or may – e.g., for a commercial CFD solvers – not be possible at all. In that case one could use matrix-free methods, as proposed by Waugh et al. [15].

In the present study, non-intrusive polynomial chaos expansion (NIPCE) is used for UQ in linear thermoacoustic stability analysis. The polynomial chaos expansion approximates uncertain output as a polynomial function of uncertain input parameters and provides statistical moments of the output. The advantage of the non-intrusive variant of the method is the treatment of an investigated system as a “black box”, so the method can be applied to any system model without any special code modifications. Another advantage is that NIPCE provides a polynomial approximation of the output quantity, which can be used as a reduced order model, or for sensitivity analysis.

NIPCE has hitherto not been used in thermoacoustics – except for the analysis of Nair et al. [16], which is discussed below – but it has been applied frequently in computational fluid dynamics [3] and also in simulations of reacting flows [17]. There are several possibilities for constructing the NIPCE: Hosder et al. [18–20] used linear regression, Reagan et al. [1,21] used the Latin hypercube sampling technique, Tritschler et al. [22] used the Gauss quadrature. We choose the Gauss quadrature, since it synchronizes the expansion order with the number of quadrature points. Hence, a large number of system evaluations leads to a higher expansion order.

Nair et al. [16] explored the use of NIPCE to quantify the uncertainty of subcritical Hopf bifurcations predicted by a simplistic model of a Rijke tube. However, a subcritical bifurcation represents a special challenge, since it exhibits a discontinuity, which with standard polynomials cannot represent well. Indeed, NIPCE was originally developed for continuous uncertainties, thus we use this method for continuous problems. Instead of NIPCE, Nair and co-workers eventually employed a sampling technique based on equal probabilities to compute the failure probability for several input parameter values. Then they reconstructed the response in the entire parameter space by an interpolation technique that captures discontinuities. The UQ was then performed by a Monte Carlo simulation of the interpolated model.

We have discussed briefly the use of active subspace and adjoints for UQ in thermoacoustics. NIPCE should not be seen as a competitor to the above mentioned methods, but rather as a complementary tool to solve problems, where neither active subspace nor adjoints are feasible. For instance, if access to solver state matrices is not feasible, then the adjoint approach cannot be employed, unless the matrix-free methods are used. On the contrary, NIPCE can easily be applied in that case, since it treats the solver as a “black box”. If a single system evaluation is so expensive that the random sampling required for identification of active variables is impractical, then NIPCE with Gauss quadrature may still solve the problem, since the method requires only a few quadrature points. On the other hand, the application of the NIPCE with standard polynomials is constrained to continuous uncertainties, and the number of uncertain parameters should not exceed roughly ten. For discontinuous or steep functions one may try NIPCE with Haar polynomials [23] or the above-mentioned method proposed by Nair et al. [16].

In this study, we employ NIPCE to perform UQ and sensitivity analysis for thermoacoustic systems. Moreover, it is shown that probability density functions of the sensitivities are suitable for analysis of systems with multiple uncertain input parameters. The paper is structured as follows: in the next section, the fundamentals of the NIPCE method are described briefly. Then the NIPCE is validated against a Monte Carlo simulation for a simplified combustor, which is modeled by the Helmholtz equation with the n–τ flame model. The uncertain parameters are the gain n and the time delay τ, as well as the magnitude and phase of an outlet reflection coefficient. Afterward, a thermoacoustic network model is investigated using NIPCE. The network model includes flame transfer functions identified from CFD simulations. In this case, validation against the Monte Carlo simulation is no longer possible, since a single CFD simulation for the flame identification takes several

Table 1
Most common probability distribution types and corresponding optimal polynomial types [24].

Distribution	Probability density function	Polynomial	Support range
Normal	$\frac{1}{\sqrt{2\pi}}e^{-\xi^2/2}$	Hermite	$[-\infty, \infty]$
Uniform	1/2	Legendre	$[-1, 1]$
Beta	$\frac{(1-\xi)^\alpha(1+\xi)^\beta}{2^{\alpha+\beta+1}B(\alpha+1,\beta+1)}$	Jacobi	$[-1, 1]$
Exponential	$e^{-\xi}$	Laguerre	$[0, \infty]$
Gamma	$\frac{\xi^\alpha e^{-\xi}}{\Gamma(\alpha+1)}$	Generalized Laguerre	$[0, \infty]$

hours. Therefore this is a typical application case for NIPCE. The uncertain input parameters are the flow velocity, the burner plate temperature, and the equivalence ratio. In the next part of this study, we show that the uncertainty analysis can be extended by additional uncertain parameters without significant computational effort, provided that these parameters are included only in the network model and independent of the other uncertain parameters, in particular the flame transfer function. In the present study, two additional uncertain parameters, i.e., the magnitude of the inlet and outlet reflection coefficients, are introduced. A summary of results concludes the paper.

2. Uncertainty quantification methodology

This section introduces the concept of non-intrusive polynomial chaos expansion (NIPCE). For detailed information about the method, the reader is referred to Adams et al. [24] or Eldred et al. [25]. NIPCE approximates an output quantity y as a truncated sum of multidimensional orthogonal polynomials Ψ_i of uncertain input parameters $\boldsymbol{\xi} = [\xi_1, \xi_2, \ldots, \xi_N]$:

$$y \cong \sum_{i=0}^{P-1} \alpha_i \Psi_i(\boldsymbol{\xi}), \tag{1}$$

where α_i are the weighting coefficients and P is the total number of expansion terms. The uncertain input parameters $\xi_1, \xi_2, \ldots, \xi_N$ are standardized and uncorrelated. If the original uncertain input parameters are correlated, then they should be transformed to independent standard random variables. The multidimensional polynomials $\Psi_i(\boldsymbol{\xi})$ are constructed using a tensor-product expansion of one-dimensional polynomials $\psi(\xi_j)$, i.e., the multidimensional polynomials are permutations of one-dimensional polynomials in all parameter dimensions. In this case, the total number of expansion terms P is constrained by one-dimensional polynomial order bounds p_j for the jth uncertain input parameter

$$P = \prod_{j=1}^{N} (p_j + 1). \tag{2}$$

Note that the tensor-product expansion supports anisotropy. Hence, the polynomial order bounds p_j can be chosen independently for each uncertain parameter ξ_j. Nevertheless, in this paper we consider the same polynomial order bounds for all uncertain input parameters $p = p_1 = p_2 = \ldots = p_j$. For brevity, we also define the NIPCE order equal to the one-dimensional polynomial order bound p, although the effective order of the NIPCE is Np due to the tensor-product expansion of the one-dimensional polynomials.

The choice of the one-dimensional polynomial $\psi(\xi_j)$ depends on the probability distribution of the uncertain input parameter ξ_j. Note that each ξ_j can follow a different distribution. Each probability distribution type has its own optimal polynomial type [24]. The most common one-dimensional orthogonal polynomials are listed in Table 1. In this work the uncertain input parameters are assumed uniformly distributed, thus the Legendre polynomials are chosen for the NIPCE. The first three Legendre polynomials are:

$$\psi_0(\xi_1) = 1, \tag{3}$$

$$\psi_1(\xi_1) = \xi_1, \tag{4}$$

$$\psi_2(\xi_1) = \frac{1}{2}(3\xi_1^2 - 1). \tag{5}$$

Hence, the multidimensional Legendre polynomials for a two-dimensional case with $p = 2$ are:

$$\Psi_0(\xi_1, \xi_2) = \psi_0(\xi_1)\psi_0(\xi_2), \tag{6}$$

$$\Psi_1(\xi_1, \xi_2) = \psi_1(\xi_1)\psi_0(\xi_2), \tag{7}$$

$$\Psi_2(\xi_1, \xi_2) = \psi_0(\xi_1)\psi_1(\xi_2), \tag{8}$$

$$\Psi_3(\xi_1, \xi_2) = \psi_1(\xi_1)\psi_1(\xi_2), \tag{9}$$

$$\Psi_4(\xi_1, \xi_2) = \psi_2(\xi_1)\psi_0(\xi_2), \tag{10}$$

$$\Psi_5(\xi_1, \xi_2) = \psi_2(\xi_1)\psi_1(\xi_2), \tag{11}$$

$$\Psi_6(\xi_1, \xi_2) = \psi_0(\xi_1)\psi_2(\xi_2), \tag{12}$$

$$\Psi_7(\xi_1, \xi_2) = \psi_1(\xi_1)\psi_2(\xi_2), \tag{13}$$

$$\Psi_8(\xi_1, \xi_2) = \psi_2(\xi_1)\psi_2(\xi_2). \tag{14}$$

Note that the effective order of the NIPCE, constructed with the multidimensional polynomials from above, is four. But since $p = 2$, the NIPCE is of the second order according to our definition.

The polynomials Ψ_i are orthogonal, hence the weighting coefficients α_i of the expansion, defined in Eq. (1), are computed using a spectral projection

$$\alpha_i = \frac{\langle y, \Psi_i \rangle}{\langle \Psi_i^2 \rangle} = \frac{\int_\Omega y \Psi_i \rho(\boldsymbol{\xi}) d\boldsymbol{\xi}}{\int_\Omega \Psi_i^2 \rho(\boldsymbol{\xi}) d\boldsymbol{\xi}}, \tag{15}$$

where $\langle , \rangle$ denotes the inner product and Ω is the uncertain input parameter space. The joint probability density function $\rho(\boldsymbol{\xi})$ is computed from one-dimensional probability density functions, since the uncertain input parameters are uncorrelated. The one-dimensional probability density functions for different distribution types are given in Table 1. The inner products of multidimensional polynomials $\langle \Psi_i^2 \rangle$ are computed analytically, and the inner products of the output quantity and the polynomial $\langle y, \Psi_i \rangle$ are computed by a Gauss quadrature, that is synchronized to the polynomial order. Gauss quadrature with k points integrates exactly all polynomials of degree $2k - 1$ or less. Since y and Ψ_i are multiplied in Eq. (15), the highest order of the integrand is then $2p_j$ in jth parameter dimension. This requires $p_j + 1$ quadrature points for exact integration in each dimension.

When the coefficients α_i are determined, mean μ and variance σ^2 of the output quantity can be computed as follows:

$$\mu \cong \sum_{i=0}^{N-1} \alpha_i \langle \Psi_i(\boldsymbol{\xi}) \rangle = \alpha_0, \tag{16}$$

$$\sigma^2 \cong \sum_{i=0}^{N-1} \alpha_i^2 \langle \Psi_i(\boldsymbol{\xi})^2 \rangle. \tag{17}$$

Note that in addition to the statistical moments, the NIPCE provides a polynomial approximation for the output quantity (see Eq. (1)), which can be used as a reduced order model or for sensitivity analysis with the derivatives of y given by

$$\frac{\partial y}{\partial \xi_i} = \sum_{j=0}^{P} \alpha_j \frac{\partial \Psi_j(\boldsymbol{\xi})}{\partial \xi_i}. \tag{18}$$

Summarizing all the steps, the UQ analysis using the NIPCE is performed as follows:

1. Specify a probability distribution for the uncertain input parameters.
2. Choose a suitable polynomial type according to the probability distribution of the uncertain input parameters.
3. Choose the polynomial order bound p_j for each uncertain input parameter ξ_j.
4. According to the quadrature rules, evaluate the system at the predefined uncertain parameter values.
5. Compute the polynomial weighting coefficients α_i, see Eq. (15).
6. Compute mean and variance of the uncertain output quantity, see (Eqs. (16), (17)).
7. Construct the NIPCE and compute the output for any set of input parameters, see Eq. (1).
8. Compute sensitivities, see Eq. (18).

3. Validation case

In this section, NIPCE is validated against Monte Carlo simulation. For that purpose, a simplistic model problem is chosen, with a low evaluation time of several seconds for the full model. We consider four uncertain input parameters: the gain and the time delay of the flame transfer function, the magnitude and the phase of an outlet reflection coefficient. Then the growth rate of a thermoacoustic system is computed using a Helmholtz solver.

3.1. Setup

The validation case is taken from the work of Silva et al. [12]. The authors numerically investigated the uncertainty of the growth rate of thermoacoustic instability in a turbulent swirled combustor EM2C laboratory [26–28]. The inhomogeneous Helmholtz equation is solved for eigenvalues with the ansatz function e^{st} for the fluctuation:

$$s^2\hat{p} - \nabla \cdot \left(\bar{c}^2 \nabla \hat{p}\right) = s(\bar{\gamma} - 1)\hat{q}, \tag{19}$$

where p, $\dot{q}$, c and γ denote the pressure, local heat release rate, mean speed of sound and heat capacity ratio. Overline indicates the time averaged quantity and circumflex indicates a complex amplitude field. The Laplace variable $s = \varsigma + i2\pi f$ consists of the growth rate ς (s^{-1}) and frequency $f(Hz)$. The local heat release rate is modeled with a simple $n-\tau$ model [29,30]:

$$\frac{\hat{\dot{q}}}{\bar{\dot{q}}} = n e^{-s\tau} \frac{\hat{u}_{ref}}{\bar{u}_{ref}}, \tag{20}$$

where n is a gain of the flame transfer function, τ is a characteristic time delay and u_{ref} is an acoustic velocity at a reference position.

We investigate the swirled combustor in configuration C4 (Fig. 1). Following Silva et al. [12] we consider four uncertain input parameters: the gain n and the time delay τ of the flame transfer function, the magnitude $|R_{out}|$ and the phase $\angle R_{out}$ of the outlet reflection coefficient. The uncertainty parameters are assumed to be uniformly distributed and are listed in Table 2 together with the operating conditions. The speed of sound is computed with the ideal gas assumption.

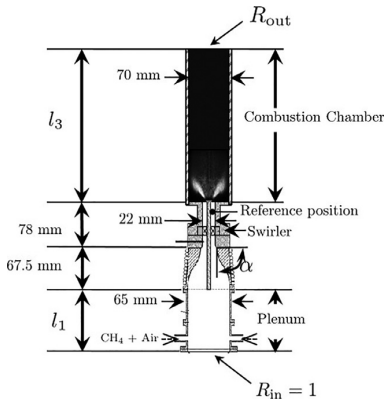

Fig. 1. Turbulent swirled combustor in configuration C4 ($l_1 = 0.096$ m, $l_3 = 0.4$ m, $\alpha = 90^\circ$). Adapted from Palies et al. [26].

Table 2
Uncertain input parameters and operating conditions.

n	$1.5 \pm 10\%$
τ	$4.73 \pm 10\%$ ms
$\lvert R_{out}\rvert$	$0.6 \pm 10\%$
$\angle R_{out}$	$\pi \pm 10\%$ rad
$\bar{u}_{ref}$	4.16 m/s
$\bar{\gamma}$	1.4
Equivalence ratio	0.8
Specific gas constant	287 J/(kgK)
Temperature upstream of the flame	300 K
Temperature downstream of the flame	1600 K
Total heat release rate	3.03 kW
Operating pressure	101, 325 Pa

Table 3
Mean and standard deviation of the growth rate. MC denotes Monte Carlo simulation.

	NIPCE			MC
p	1	2	3	
μ (s^{-1})	109.63	109.64	109.67	109.70
σ (s^{-1})	17.95	17.88	17.91	17.87
Samples	16	81	256	10^5

Due to the $n-\tau$ flame model, the eigenvalue problem is nonlinear. Nevertheless, the Helmholtz solver is quite efficient, such that one simulation takes only a few seconds. Thus it is feasible for this test case to validate NIPCE results with Monte Carlo simulation.

3.2. Results

The NIPCEs with $p = 1$, $p = 2$, and $p = 3$ are computed, which require 16, 81 and 256 Helmholtz solver simulations, respectively. The validation data is generated by the Monte Carlo simulation with 10^5 random samples to guarantee stochastic convergence. The statistical moments of the growth rate are shown in Table 3. All polynomial expansions yield results in good agreement with the Monte Carlo results.

Additionally, the probability density function (PDF) of the growth rate is computed by a Monte Carlo simulation applied on the polynomial expansion. The results are compared to the Monte Carlo simulation of the Helmholtz solver in Fig. 2. Note that a single evaluation of the NIPCE requires several scalar mathematical operations, while the Helmholtz solver performs several matrix inversions to converge. Thus the PDF computation with the NIPCE is much faster than with the Helmholtz solver. Figure 2 suggests that the NIPCE with $p = 1$ already reproduces the PDF well. It should

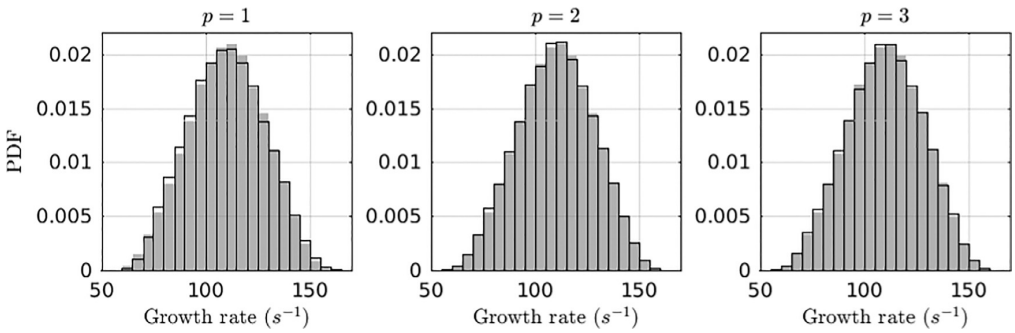

Fig. 2. PDF of the growth rate with 10^5 samples, p is the NIPCE order, the bin size is $5\,s^{-1}$. The transparent bins with black edges are the NIPCE results, the grey bins are the results produced by the Helmholtz solver.

be mentioned that in the work of Silva et al. only the second order expansion, computed with adjoints, was in quantitative agreement with the reference PDF (see Fig. 7(c) in [12]). The reason why NIPCE with $p = 1$ performs better than a first order Taylor expansion of the Helmholtz solver using adjoints lies in the different modeling procedures. In general, Taylor expansion makes an approximation around one reference point and it includes derivatives which are valid only for that reference point. Therefore it is a local approximation. NIPCE, in contrast, follows a more global modeling strategy, which takes information from several quadrature points to build a polynomial. Furthermore, NIPCE with $p = 1$ implies that the highest order for each parameter is one, while the highest order of the polynomial expansion is four due to a tensor product of one-dimensional polynomials (see Section 2).

Given the PDF of the growth rate, we can compute the risk factor [31], i..e the probability that the system is unstable:

$$RF = \int_0^\infty PDF(\varsigma)d\varsigma. \tag{21}$$

According to Silva et al. [12] the combustor in this configuration experiences the damping rate $DR = 125\ s^{-1}$, which was not accounted for in the Helmholtz solver.[1] Thus the risk factor corrected by the damping rate is

$$RF_{DR} = \int_{DR}^\infty PDF(\varsigma)d\varsigma. \tag{22}$$

The risk factor of the combustor is 21.10%, whereas the polynomial expansions yield 21.08%, 21.01% and 21.06% for $p = 1$, $p = 2$ and $p = 3$, respectively. Since the PDF is well reproduced by the polynomial expansions (see Fig. 2), the risk factor is also well approximated. The reader should be cautioned, however, that such good agreement may not be achievable if the risk factor is low, because in that case its value is governed by the tail of the PDF.

The derivatives with respect to uncertain input parameters are computed according to Eq. (18). The NIPCE sensitivities at the mean values of the uncertain input parameters are validated against the derivatives computed with finite differences in Table 4. All expansion orders approximate the derivatives well. For this configuration, it is sufficient to use the first order NIPCE.

4. UQ of intrinsic thermoacoustic instability

In this section, the thermoacoustic stability of the Kornilov flame [32] is analyzed with NIPCE. For this configuration, instability may occur due to a positive feedback between fluctuations of heat release rate and flow velocity upstream of the flame, even

[1] In general, the damping rate is highly uncertain and could be also considered as an uncertain parameter.

Table 4
Sensitivities computed at the mean values of the uncertain input parameters. FD denotes the finite difference method.

	NIPCE			FD
p	1	2	3	
$\partial\varsigma/\partial n$ (s^{-1})	39.68	39.56	39.73	39.61
$\partial\varsigma/\partial\tau$ (s^{-2})	75.69	75.21	75.47	74.83
$\partial\varsigma/\partial\lvert R_{out}\rvert$ (s^{-1})	56.02	54.85	56.31	54.80
$\partial\varsigma/\partial(\angle R_{out})$ (s^{-1})	38010	37925	38682	38127

without significant reflection of acoustic waves from the up- or downstream boundaries [33,34]. The intrinsic thermoacoustic feedback mechanism is extensively discussed in references [35–37].

Stability analysis is performed using a thermoacoustic network model with flame transfer functions identified from CFD simulations. We consider uncertainties in operating and thermal conditions in CFD simulations, which result in uncertainties in the flame transfer function and, consequently, in the growth rate.

This test case, like the next one presented in Section 5, is a typical application case for NIPCE. Monte Carlo simulation cannot be applied due to expensive CFD simulations. Application of the adjoint approach for the current CFD solver is not feasible. Application of the active subspace is not justified, since there are only three uncertain parameters. In addition, the active subspace requires random samples to identify active variables and to fit a low order model, but the sampling is again problematic, because of the computational cost of the CFD simulations. Therefore, NIPCE is the method of choice to solve this type of problem with reasonable computational effort.

4.1. Setup

The experimental and numerical setups are shown in Fig. 3. The experiment represents a laminar slit burner fed by a methane/air mixture. For a CFD simulation, we take one-half of a single flame in two dimensions, as it is done in the most of the numerical works on a Kornilov flame [32,38,39].

The only one uncertainty, reported in the experiment, is the burner plate temperature, which is between 373 and 423 K, but with unknown distribution. Given the lack of detailed knowledge we decide for a rather generic study and add two other uncertain operating parameter to the burner plate temperature. For the UQ study we increase the uncertainty in the burner plate temperature by an additional 50 K, resulting in $T = 398 \pm 50$ K. We also introduce uncertainties in the inlet velocity $u = 0.4 \pm 0.02$ m/s and in the equivalence ratio $\phi = 0.8 \pm 0.1$. We choose uniform distribution for all three parameters, because it is the least biased estimate which maximizes the entropy for given uncertainty bounds [40].

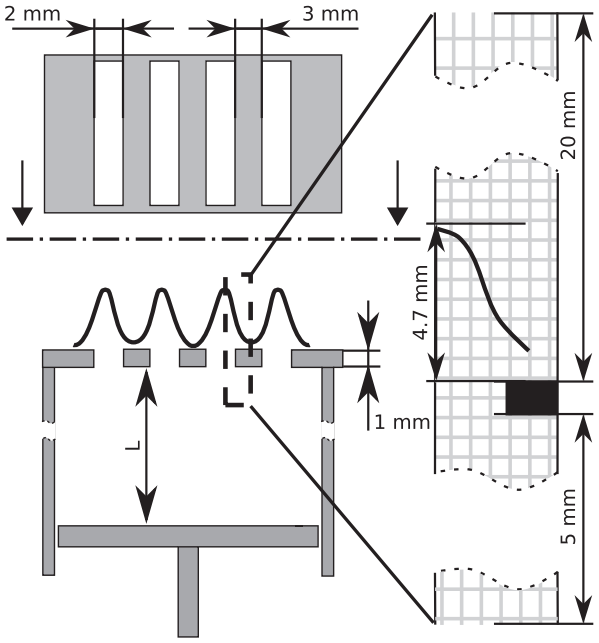

Fig. 3. Left: sketch of the experimental test rig. Right: truncated CFD domain.

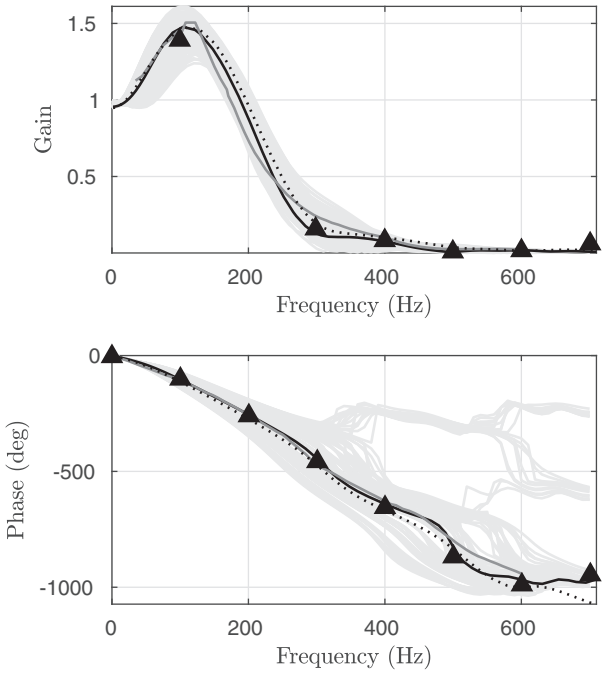

Fig. 4. Flame frequency response for $u = 0.4$ m/s, $T = 373$ K, and $\phi = 0.8$: weakly compressible OpenFOAM simulation (black line), experiment of Kornilov et al. [32] (dark grey line), DNS of Silva et al. with upstream excitation [37] (dotted line), DNS of Duchaine et al. [38] (triangles). The set of the flame transfer functions, used in the thermoacoustic network model, is shown in light grey.

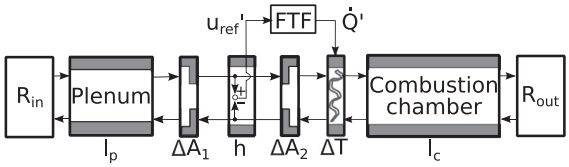

Fig. 5. Scheme of the network model.

The inlet temperature and the outlet pressure are kept constant: $T_{in} = 293$ K and $p_{out} = 101,325$ Pa. The chemistry is modeled using the two-step reaction mechanism 2S-CM2 [38]. A structured two-dimensional mesh consists of 65,700 cells with 18 cells across the reaction zone. To compute the flame transfer function, we use a weakly compressible low Mach number solver implemented in OpenFOAM [39]. This solver does not resolve acoustics, since density depends only on temperature and not on pressure. Hence, the thermoacoustic feedback is suppressed, and the flame does not experience thermoacoustic instability in the CFD simulation. This property of the weakly compressible solver is beneficial for the computation of the flame transfer function.

4.2. Identification of the flame transfer function

The flame transfer function is obtained from CFD simulation data by estimating the finite impulse response of the global heat release rate $\dot{Q}'$ to a velocity perturbation upstream of the flame u'_{ref}. A broadband velocity excitation is applied at the inlet, therefore a single simulation is sufficient to generate the time series data needed for the identification of flame dynamics. The Matlab system identification toolbox is used in the present study, for further details on the application of system identification to the study of flame dynamics, the reader is referred to Tay-Wo-Chong et al. [41], or the review of Polifke [42]. The flow time is set to 0.25 s, which is sufficient to identify the flame transfer function. One CFD run takes around 24 h on a 28-core Intel Xeon E5-2697 machine running at 2.6 GHz.

In Fig. 4 the flame frequency response identified from a weakly compressible OpenFOAM simulation is compared against experimental data as well as numerical studies carried out by other authors. It is evident that the OpenFOAM solver is able to capture the flame dynamics and reproduces well the frequency response. Furthermore, the figure shows the frequency responses of a set of flame transfer functions, which reflect the effect of the uncertainties in burner plate temperature, inflow velocity and equivalence ratio on the flame dynamics. Clearly, there is considerable sensitivity of gain and phase[2] to changes in these three model parameters. Nevertheless, all identified flame transfer functions are smooth without bifurcations. This set of transfer functions forms the basis of thermoacoustic stability and uncertainty analysis, which will be presented below.

4.3. Thermoacoustic network model

The instability is studied with a thermoacoustic network model shown in Fig. 5. The network model is built with the in-house tool taX [43,44]. The interconnections between the network elements are established by up- and downstream acoustic waves f and g:

$$f = \frac{1}{2}\left(\frac{p'}{\bar{\rho}\bar{c}} + u'\right), \tag{23}$$

$$g = \frac{1}{2}\left(\frac{p'}{\bar{\rho}\bar{c}} - u'\right). \tag{24}$$

[2] The importance of the very large variations in phase at frequencies above 300 Hz should not be overestimated. In this frequency range, the gain is very low and indeed approaches zero, such that the phase is ill-defined. If one plots the flame frequency response in terms of its real and imaginary parts, variations at high frequencies tend to zero (not shown).

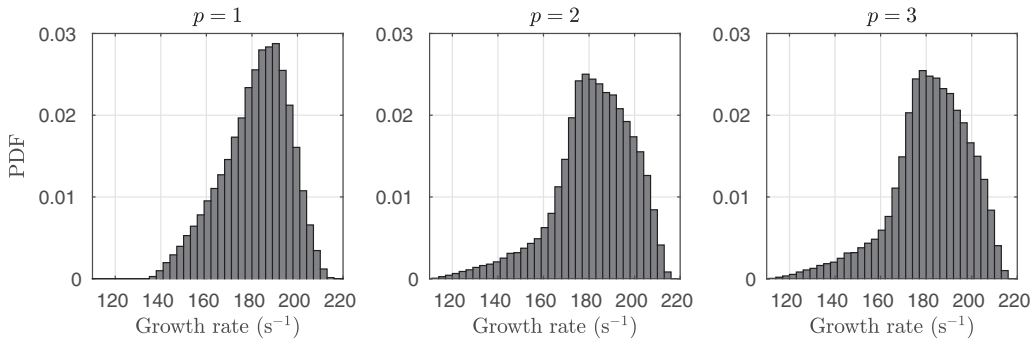

Fig. 6. PDF of the growth rate with 10^5 samples, p is the NIPCE order, the bin size is $3\,s^{-1}$.

Table 5
Mean and standard deviation of the growth rate. The last column indicates the number of simulations needed to construct the NIPCE.

p	μ (s^{-1})	σ (s^{-1})	Samples
1	181.65	14.70	8
2	182.02	17.34	27
3	182.02	17.09	64

We consider a plenum with $l_p = 0.05\,m$, a burner plate and a combustion chamber with $l_c = 0.2\,m$. The burner plate is modeled by an area contraction of 0.4, a duct with $h = 1\,mm$ and an area expansion of 2.5. The flame is placed directly after the area expansion and is modeled with a linearized Rankine–Hugoniot jump conditions combined with the flame transfer function identified from the CFD simulation. The temperatures upstream and downstream of the flame are also taken from the CFD simulation. The velocity reference point is located in the middle of the duct through the burner plate. The equations for the used network elements are summarized in Appendix A. The inlet and outlet boundary conditions are set to fully non-reflecting: $R_{in} = R_{out} = 0$. The network model computes the growth rate of the thermoacoustic system within a few seconds. But the CFD simulation, required to identify the flame transfer for one set of uncertain parameters, is expensive. The UQ analysis consists of the following steps:

1. Run CFD simulations to identify the flame transfer functions for the uncertain input parameter values defined by the quadrature rule.
2. Build a network model for each flame transfer function, compute the growth rates.
3. Build the NIPCE.

4.4. Convergence study

Since a single CFD simulation is expensive, it is not feasible to validate the NIPCE results with a Monte Carlo simulation. Therefore, we perform a convergence study using only NIPCE of different orders. The objective is to increase the order until the statistical moments do not change significantly, which we interpret as convergence of results. Table 5 shows the mean and standard deviation of the growth rate for the NIPCE with $p = 1$, $p = 2$ and $p = 3$. The second and third order expansions yield almost the same mean and standard deviation.

We also study the PDFs of the growth rate in Fig. 6, to better assess the convergence. The PDFs are computed with the Monte Carlo simulation of polynomial expansions with 10^5 samples, which suffice to ensure convergence of the PDF. The Monte Carlo simulation of the NIPCE is affordable, since the computation time of a single polynomial evaluation is negligibly small. The PDFs for the first, second and third order NIPCEs are shown in Fig. 6. The NIPCEs with $p = 2$ and $p = 3$ match. For the chosen uncertainty parameter space, the NIPCE needs at least a tensor product expansion of quadratic one-dimensional polynomials for the uncertainty propagation. Further increase of polynomial order does not significantly improve the PDF of the growth rate. We assume that the results are converged, and we stop the study with the third order expansion. For the convergence study 8, 27 and 64 CFD simulations were performed for $p = 1$, $p = 2$ and $p = 3$, respectively. For the further analysis, we consider only the NIPCE with $p = 3$.

4.5. Results

According to Fig. 6 the growth rate is always positive, which indicates that the intrinsic thermoacoustic mode is unstable in the entire uncertain input parameter space. For $u = 0.4\,m/s$, $T = 373\,K$ and $\phi = 0.8$ Silva et al. [37] showed that the intrinsic thermoacoustic mode is unstable in a thermoacoustic network model (growth rate $170\,s^{-1}$) as well as in a compressible CFD simulation with non-reflecting boundary conditions. It is noticeable that the PDF is skewed to left, which was not the case for the swirled combustor (see Fig. 2). The reason for the skewness was not investigated further, since it is beyond the scope of the paper.

The derivatives of the NIPCE are computed for sensitivity analysis. We are not interested in a local sensitivity, but rather in the sensitivity PDF, which reflects the global system behavior. The statistical moments and the PDFs of the sensitivities are built by means of the Monte Carlo simulation with 10^5 samples and are shown in Fig. 7. To allow an easy comparison of the sensitivities, they are normalized with the corresponding standard deviations σ_i of the corresponding input parameters ξ_i: $\sigma_i \partial\varsigma/\partial\xi_i$. Note that if the input parameter distribution or its bounds change, then the corresponding normalized sensitivity will also change. Fig. 7 shows that the velocity sensitivity $\sigma_u \partial\varsigma/\partial u$ is positive in the entire parameter space, i.e., increasing velocity always destabilizes the system. The mean and the spread of the temperature sensitivity $\sigma_T \partial\varsigma/\partial T$ are the smallest among the three parameters, thus the effect of temperature on the growth rate can be safely neglected for the given parameter bounds. The equivalence-ratio sensitivity $\sigma_\varphi \partial\varsigma/\partial\varphi$ does not show a clear trend: its mean is negative, but its standard deviation is roughly four times larger than the magnitude of the mean. As a consequence, the equivalence-ratio sensitivity has negative and positive values almost with equal probabilities. It is not possible to identify the most important parameter between velocity and equivalence ratio. The velocity sensitivity has a clear destabilizing trend and the largest mean value, but the equivalence-ratio sensitivity, on the other side, has the largest spread and a non-monotonous trend.

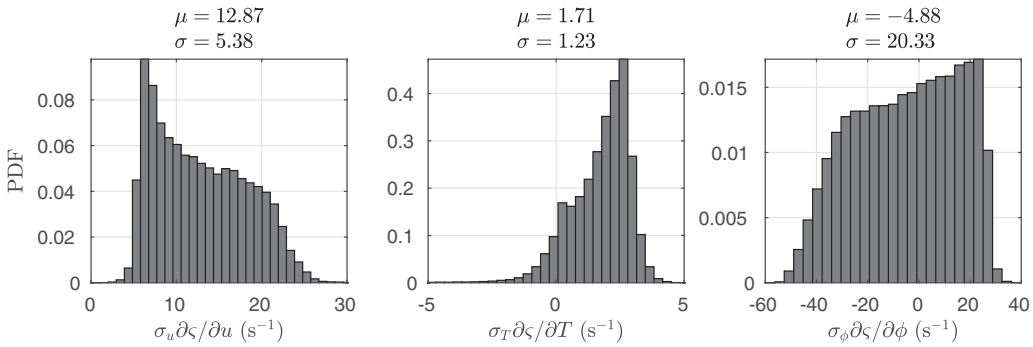

Fig. 7. Sensitivities of the growth rate. Histogram with 10^5 samples and bin size of 5, 2.5 and 10 s^{-1}, respectively.

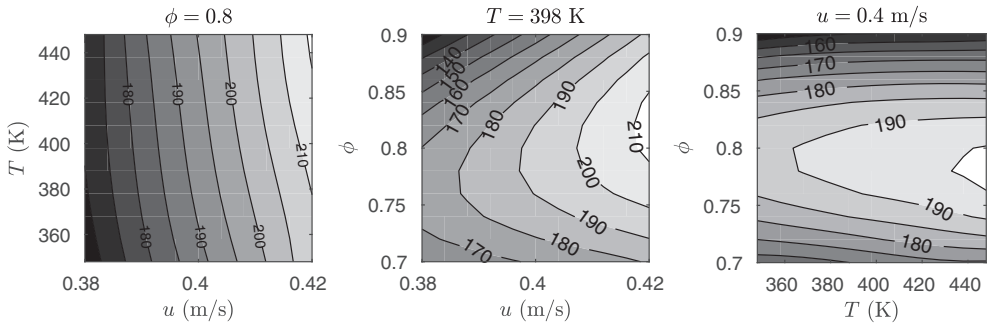

Fig. 8. Stability maps. Isolines correspond to the growth rate (s^{-1}).

Since the NIPCE provides the polynomial for the output quantity, a two-dimensional stability map can be plotted. The stability maps cannot be used to draw a conclusion for the entire three-dimensional input parameter space. Nevertheless, the stability maps can support the sensitivity analysis by visualizing overall trends. Figure 8 shows isolines of the growth rate depending on two input parameters. The remaining input parameter is kept constant at its mean value. The stability maps show that the increasing velocity increases the growth rate. The temperature has indeed a minor effect on the growth rate. The equivalence ratio behaves non-monotonically: there is a local maximum in the growth rate around $\phi = 0.78$.

5. UQ with additional uncertain input parameters

The aim of this section is to show that the UQ study can be extended by additional uncertain input parameters without significant computational effort, provided that these parameters are included only in the thermoacoustic model. We investigate the same thermoacoustic network model as in the previous Section – see Fig. 5 – but we introduce additional uncertainties in the inlet and outlet boundary conditions R_{in} and R_{out}.

5.1. Setup

The inlet and outlet reflection coefficients of the network model are assumed to be uniformly distributed over the ranges $0 \le R_{in} \le 0.4$ and $-0.4 \le R_{out} \le 0$. These uncertainty bounds were chosen with the intent to operate the thermoacoustic system in a parameter range, where stable as well as unstable behavior may occur (see below). The reflection coefficients are elements of the thermoacoustic network model, thus repeated network simulations have to be performed for the new setup. Fortunately, the identified flame transfer functions can be reused from the previous case, since they were computed with the weakly compressible CFD solver, which does not resolve acoustics. This implies that there is no need to perform any additional CFD simulations if we rely on the first, second or third order NIPCEs. Hence, the study is computationally inexpensive despite the curse of dimensionality.

Table 6
Mean and standard deviation of the growth rate. The last column indicates the number of simulations needed to construct the NIPCE. Values in parenthesis indicate the number of CFD simulations.

p	μ (s^{-1})	σ (s^{-1})	Samples
1	16.28	86.23	32 (8)
2	12.21	82.92	243 (27)
3	11.99	82.51	1024 (64)

5.2. Convergence study

We compute the first, second and third order NIPCEs. Table 6 shows statistical moments of the growth rate. Figure 9 shows the growth rate PDFs computed with Monte Carlo simulation of the NIPCE with 10^6 samples. The statistical moments and the PDFs indicate almost no difference between the second and third order expansions. Hence, we assume convergence, and we use the NIPCE with $p = 3$ for further analysis.

5.3. Results

In the previous configuration with non-reflecting boundaries $R_{in} = R_{out} = 0$, the system was thermoacoustically unstable over the entire range of parameters considered. In the new configuration with non-zero reflection coefficients, the system may be stable or unstable, depending on the respective values of reflection coefficients (see Fig. 9 and Table 6). The observation that an in-

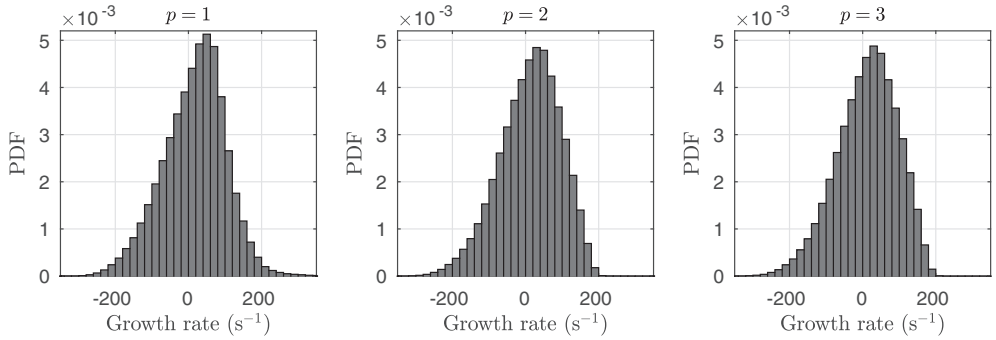

Fig. 9. PDFs of the growth rate with 10^6 samples, p is the NIPCE order, the bin size is $20\,s^{-1}$.

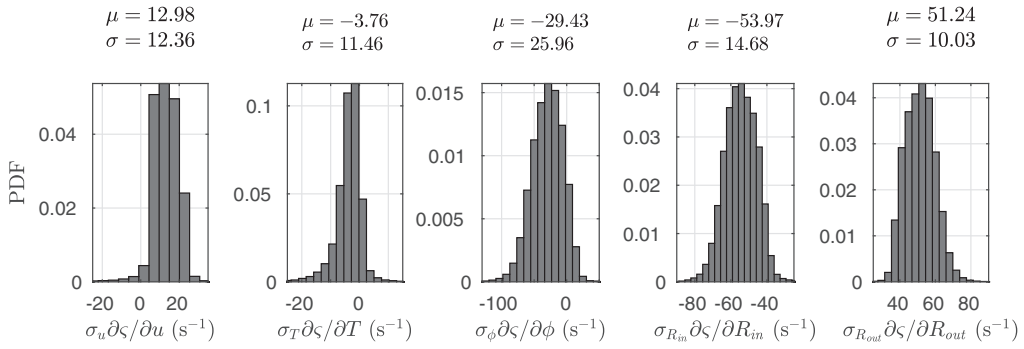

Fig. 10. Sensitivities of the growth rate. Histogram with 10^6 samples and bin size of 5, 2.5, 6, 5 and $5\,s^{-1}$, respectively.

crease in acoustic reflection coefficients may stabilize a system appears counter-intuitive at first sight. However, it has been reported repeatedly that *intrinsic* thermoacoustic instability may be stabilized by increasing reflections at the boundaries, and satisfactory explanations of this paradoxical behavior have been developed [33,37,45].

Using Eq. (21), the risk factors are computed to be 60.8%, 58.8% and 58.6% for $p = 1$, $p = 2$ and $p = 3$, respectively. The agreement between the last two risk factors correlates with the matching PDFs for $p = 2$ and $p = 3$ (see Fig. 9).

Figure 10 shows PDFs and statistical moments of the sensitivities. In this case the sensitivities with respect to the two reflection coefficients are dominant, i.e., they have the largest mean absolute values. Stronger acoustic reflection at the boundaries (i.e., higher R_{in} or lower R_{out}) decreases the growth rate. This observation supports the above statement about the possibly stabilizing effect of stronger reflections on intrinsic thermoacoustic instabilities. In comparison to the non-reflecting system, the uncertainty in reflection coefficients considerably increases the temperature and equivalence-ratio sensitivities. We argue that these increased sensitivities are a result of the stronger coupling between the flame dynamics and the acoustic environment that results from stronger acoustic reflections at the boundaries. With stronger coupling, the relative phase of the flame transfer function and the acoustic impedance becomes more important and can significantly modify the Rayleigh index and thus the growth rate of a thermoacoustic instability. The increasing equivalence ratio shows a predominantly stabilizing trend, distinct from the non-reflecting configuration (see Fig. 7). As before, compared to other uncertain input parameters, temperature has only a minor effect on the system stability. Finally, the velocity sensitivity is weakly coupled with the reflection coefficients and thus remains almost unchanged and shows the same destabilizing effect as previously.

To support our statements from the previous paragraph, the stability maps for (R_{in}, R_{out}), (u, ϕ) and (ϕ, R_{out}) are shown in Fig. 11. The stability maps exhibit stable and unstable zones. The reflection coefficients have the largest influence on the stability. The higher R_{out} and u are, the higher the growth rate is, and vice versa for ϕ and R_{in}.

6. Conclusion

This study successfully demonstrates the use of non-intrusive polynomial chaos expansion (NIPCE) for forward uncertainty quantification and sensitivity analysis in thermoacoustics. In particular, NIPCE was applied to investigate the linear thermoacoustic stability of two premixed flame configurations. The first test case allowed validation of the NIPCE against a Monte Carlo simulation and it was found that already the first order expansion yields accurate results. In the second test case, we considered a low order thermoacoustic network model coupled with a non-trivial flame transfer function, which was identified by CFD simulation. Three parameters of the CFD model were considered uncertain. With computationally expensive CFD simulations and a low number of uncertain parameters, this is a typical application case for NIPCE. The study was extended by introducing additional uncertain parameters. This could be done without significant computational effort, since the additional uncertain parameters were included only in the low order network model, but not in CFD simulations. In both cases, the second order polynomials suffice to model the uncertainties. Previous UQ studies on thermoacoustic stability with adjoint approach [11–14] also concluded that second order models are good enough to model the growth-rate uncertainties. However, we should not generalize this conclusion. The second order models might not suffice for higher input uncertainties or other system configurations.

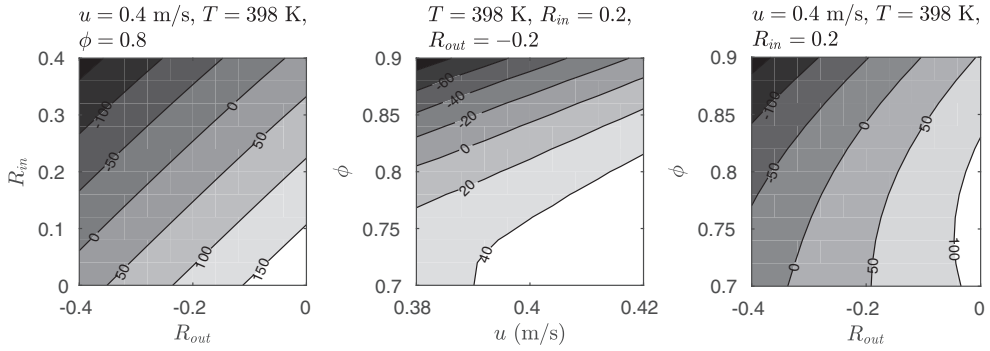

Fig. 11. Stability maps. Isolines correspond to the growth rate (s^{-1}).

In conclusion, NIPCE is suitable for problems with a small number of uncertain input parameters and with expensive single system evaluations, where a Monte Carlo simulation is unfeasible. NIPCE treats the system under investigation as a "black box", thus it can be applied to a wider variety of system models, provided that the uncertainties are continuous and smooth. For UQ of CFD simulations, characterized by a computation time from tens to hundreds of hours, the number of uncertain input parameters is limited to five or six for second order polynomials. On the other hand, for UQ of a low order model, characterized by a computation time of few minutes, the parameter number can be increased to ten. The NIPCE is also a powerful framework for sensitivity analysis, since it provides a polynomial function for the uncertain output. Mean, standard deviation and especially probability density function of sensitivities have been proven to be very useful for system analysis.

Acknowledgments

The authors gratefully acknowledge the Gauss Centre for Supercomputing e.V. for funding this project by providing computing time on the GCS Supercomputer SuperMUC at Leibniz Supercomputing Centre under grant *pr62mu*. We would also like to thank Armin Witte for a fruitful discussion about the uncertainty in the flame transfer function.

Appendix A. Network element equations

The scattering matrix of a duct of a length L is

$$\begin{bmatrix} g_u \\ f_d \end{bmatrix} = \begin{bmatrix} 0 & e^{-\omega \frac{L}{\bar{c}-\bar{u}}} \\ e^{-\omega \frac{L}{\bar{c}+\bar{u}}} & 0 \end{bmatrix} = \begin{bmatrix} f_u \\ g_d \end{bmatrix}. \tag{A.1}$$

The subscripts u and d denote the upstream and downstream positions, respectively.

The transfer matrix of a sudden area jump without losses is taken from [46]

$$\begin{bmatrix} \frac{p'}{\bar{\rho}\bar{c}} \\ u' \end{bmatrix}_d = \begin{bmatrix} 1 & \left(1-\alpha^2\right)\overline{M}_u \\ -\overline{M}_d & \alpha \end{bmatrix} = \begin{bmatrix} \frac{p'}{\bar{\rho}\bar{c}} \\ u' \end{bmatrix}_u, \tag{A.2}$$

where α is the area jump ratio A_u/A_d and M is the Mach number.

The scattering matrix representation of a flame transfer function is taken from [36], where it was derived using linearized Rankine–Hugoniot equations including Mach number effects

$$\begin{bmatrix} \frac{p'}{\bar{\rho}\bar{c}} \\ u' \end{bmatrix}_d = \begin{bmatrix} \frac{\bar{\rho}_u \bar{c}_u}{\bar{\rho}_d \bar{c}_d} & -\left(\frac{\overline{T}_d}{\overline{T}_u}-1\right)\overline{M}_d \\ -\bar{\gamma}\left(\frac{\overline{T}_d}{\overline{T}_u}-1\right)\overline{M}_u & 1 \end{bmatrix} \begin{bmatrix} \frac{p'}{\bar{\rho}\bar{c}} \\ u' \end{bmatrix}_u + \begin{bmatrix} -\overline{M}_d \\ 1 \end{bmatrix} \left(\frac{\overline{T}_d}{\overline{T}_u}-1\right) \bar{u}_u \frac{\dot{Q}'}{\bar{\dot{Q}}}, \tag{A.3}$$

References

[1] M.T. Reagan, H.N. Najm, P.P. Pébay, O.M. Knio, R.G. Ghanem, Quantifying uncertainty in chemical systems modeling, Int. J. Chem. Kinet. 37 (6) (2005) 368–382, doi:10.1002/kin.20081.

[2] T.N. Palmer, G.J. Shutts, R. Hagedorn, F.J. Doblas-Reyes, T. Jung, M. Leutbecher, Representing model uncertainty in weather and climate prediction, Ann. Rev. Earth Planet. Sci. 33 (1) (2005) 163–193, doi:10.1146/annurev.earth.33.092203.122552.

[3] H.N. Najm, Uncertainty quantification and polynomial chaos techniques in computational fluid dynamics, Ann. Rev. Fluid Mech. 41 (2009) 35–52.

[4] A. Chernatynskiy, S.R. Phillpot, R. LeSar, Uncertainty Quantification in multiscale simulation of materials: A prospective, Ann. Rev. Mater. Res. 43 (1) (2013) 157–182, doi:10.1146/annurev-matsci-071312-121708.

[5] P. Beran, B. Stanford, C. Schrock, Uncertainty quantification in aeroelasticity, Ann. Rev. Fluid Mech. 49 (1) (2017) 361–386, doi:10.1146/annurev-fluid-122414-034441.

[6] N. Metropolis, S. Ulam, The Monte Carlo method, J. Am. Stat. Assoc. 44 (247) (1949) 335–341, doi:10.1080/01621459.1949.10483310.

[7] M.D. McKay, R.J. Beckman, W.J. Conover, A comparison of three methods for selecting values of input variables in the analysis of output from a computer code, Technometrics 21 (2) (1979) 239–245, doi:10.2307/1268522.

[8] M. Bauerheim, A. Ndiaye, P. Constantine, S. Moreau, F. Nicoud, Symmetry breaking of azimuthal thermoacoustic modes: The UQ perspective, J. Fluid Mech. 789 (2016) 534–566, doi:10.1017/jfm.2015.730.

[9] P. Constantine, E. Dow, Q. Wang, Active subspace methods in theory and practice: Applications to Kriging surfaces, SIAM J. Sci. Comput. 36 (4) (2014) A1500–A1524, doi:10.1137/130916138.

[10] A. Ndiaye, M. Bauerheim, F. Nicoud, Uncertainty quantification of thermoacoustic instabilities on a swirled stabilized combustor, ASME Turbo Expo 2015: Turbine Technical Conference and Exposition, GT2015-44133, ASME, Montreal, Quebec, Canada (2015).

[11] C. Silva, T. Runte, W. Polifke, L. Magri, Uncertainty quantification of growth rates of thermoacoustic instability by an adjoint Helmholtz solver, ASME/IGTI Turbo Expo 2016, GT2016-57659, ASME, Seoul, Korea (2016), doi:10.1115/GT2016-57659.

[12] C. Silva, L. Magri, T. Runte, W. Polifke, Uncertainty quantification of growth rates of thermoacoustic instability by an adjoint Helmholtz solver, J. Eng. Gas Turb. Power 139 (1) (2017) 011901.

[13] G.A. Mensah, L. Magri, J.P. Moeck, Methods for the Calculation of Thermoacoustic Stability Margins and Monte Carlo-Free Uncertainty Quantification, in: Proceedings of ASME Turbo Expo 2017: Turbomachinery Technical Conference and Exposition, ASME, Charlotte, NC, USA, 2017. doi:10.1115/GT2017-64829.

[14] L. Magri, M. Bauerheim, F. Nicoud, M.P. Juniper, Stability analysis of thermoacoustic nonlinear eigenproblems in annular combustors. Part II. Uncertainty quantification, J. Comput. Phys. 325 (2016) 411–421, doi:10.1016/j.jcp.2016.08.043.

[15] I. Waugh, S. Illingworth, M. Juniper, Matrix-free continuation of limit cycles for bifurcation analysis of large thermoacoustic systems, J. Comput. Phys. (2013), doi:10.1016/j.jcp.2012.12.034.

[16] V. Nair, S. Sarkar, R. Sujith, Uncertainty quantification of subcritical bifurcations, Probab. Eng. Mech. 34 (2013) 177–188.

[17] H.N. Najm, J.C. Lee, M. Valorani, D.A. Goussis, M. Frenklach, Adaptive chemical model reduction, J. Phys. Conf. Ser. 16 (2005) 101–106.

[18] S. Hosder, R. Walters, R. Perez, A non-intrusive polynomial chaos method for uncertainty propagation in CFD simulations, 44th AIAA Aerospace Sciences Meeting and Exhibit, American Institute of Aeronautics and Astronautics, doi:10.2514/6.2006-891.

[19] S. Hosder, R. Walters, M. Balch, Efficient sampling for non-intrusive polynomial chaos applications with multiple uncertain input variables, 48th AIAA/ASME/ASCE/AHS/ASC Structures, Structural Dynamics, and Materials Conference, American Institute of Aeronautics and Astronautics (2007), doi:10.2514/6.2007-1939.

[20] S. Hosder, R. Walters, M. Balch, Efficient uncertainty quantification applied to the aeroelastic analysis of a transonic wing, 46th AIAA Aerospace Sciences Meeting and Exhibit, Reno, NV (2008), doi:10.2514/6.2008-729.
[21] M.T. Reagan, H.N. Najm, R.G. Ghanem, O.M. Knio, Uncertainty quantification in reacting-flow simulations through non-intrusive spectral projection, Combust. Flame 132 (3) (2003) 545–555, doi:10.1016/S0010-2180(02)00503-5.
[22] V.K. Tritschler, A. Avdonin, S. Hickel, X.Y. Hu, N.A. Adams, Quantification of initial-data uncertainty on a shock-accelerated gas cylinder, Phys. Fluids 26 (2) (2014) 026101, doi:10.1063/1.4865756.
[23] O.P. Le Maıtre, O.M. Knio, H.N. Najm, R.G. Ghanem, Uncertainty propagation using Wiener–Haar expansions, J. Comput. Phys. 197 (1) (2004) 28–57, doi:10.1016/j.jcp.2003.11.033.
[24] B.M. Adams, W. Bohnhoff, K. Dalbey, J. Eddy, M. Eldred, D. Gay, K. Haskell, P.D. Hough, L. Swiler, DAKOTA, a multilevel parallel object-oriented framework for design optimization, parameter estimation, uncertainty quantification, and sensitivity analysis: Version 5.0 user's manual, Technical Report No. SAND2010-2183, Sandia National Laboratories, 2009.
[25] M. Eldred, J. Burkardt, Comparison of non-intrusive polynomial chaos and stochastic collocation methods for uncertainty quantification, 47th AIAA Aerospace Sciences Meeting Including The New Horizons Forum and Aerospace Exposition, American Institute of Aeronautics and Astronautics, doi:10.2514/6.2009-976.
[26] P. Palies, D. Durox, T. Schuller, S. Candel, The combined dynamics of swirler and turbulent premixed swirling flames, Combust. Flame 157 (2010) 1698–1717.
[27] P. Palies, D. Durox, T. Schuller, S. Candel, Acoustic–convective mode conversion in an aerofoil cascade, J. Fluid Mech. 672 (2011) 545–569, doi:10.1017/S0022112010006142.
[28] C.F. Silva, F. Nicoud, T. Schuller, D. Durox, S. Candel, Combining a Helmholtz solver with the flame describing function to assess combustion instability in a premixed swirled combustor, Combust. Flame 160 (9) (2013) 1743–1754, doi:10.1016/j.combustflame.2013.03.020.
[29] L. Crocco, Aspects of combustion stability in liquid propellant rocket motors part1: Fundamentals. Low frequency instability with monopropellants, J. Am. Rocket Soc. (1951) 163–178.
[30] L. Crocco, Aspects of combustion stability in liquid propellant rocket motors part 2: low frequency instability with bipropellants. High frequency instabilitiy, J. Am. Rocket Soc. 22 (1) (1952) 7–16, doi:10.2514/8.4410.
[31] M. Bauerheim, F. Nicoud, T. Poinsot, Progress in analytical methods to predict and control azimuthal combustion instability modes in annular chambers, Phys. Fluids (1994-present) 28 (2) (2016) 021303, doi:10.1063/1.4940039.
[32] V.N. Kornilov, R. Rook, J.H.M. ten Thije Boonkkamp, L.P.H. de Goey, Experimental and numerical investigation of the acoustic response of multi-slit bunsen burners, Combust. Flame 156 (10) (2009) 1957–1970, doi:10.1016/j.combustflame.2009.07.017.
[33] M. Hoeijmakers, V. Kornilov, I. Lopez Arteaga, P. de Goey, H. Nijmeijer, Intrinsic instability of flame-acoustic coupling, Combust. Flame 161 (11) (2014) 2860–2867, doi:10.1016/j.combustflame.2014.05.009.
[34] E. Courtine, L. Selle, F. Nicoud, W. Polifke, C. Silva, M. Bauerheim, T. Poinsot, Causality and intrinsic thermoacoustic instability modes, Summer Program, Center for Turbulence Research, Stanford University, Stanford, USA (2014), pp. 169–178.
[35] S. Bomberg, T. Emmert, W. Polifke, Thermal versus acoustic response of velocity sensitive premixed flames, Proc. Combust. Inst. 35 (3) (2015) 3185–3192, doi:10.1016/j.proci.2014.07.032.
[36] T. Emmert, S. Bomberg, W. Polifke, Intrinsic thermoacoustic instability of premixed flames, Combust. Flame 162 (1) (2015) 75–85, doi:10.1016/j.combustflame.2014.06.008.
[37] C.F. Silva, T. Emmert, S. Jaensch, W. Polifke, Numerical study on intrinsic thermoacoustic instability of a laminar premixed flame, Combust. Flame 162 (9) (2015) 3370–3378, doi:10.1016/j.combustflame.2015.06.003.
[38] F. Duchaine, F. Boudy, D. Durox, T. Poinsot, Sensitivity analysis of transfer functions of laminar flames, Combust. Flame 158 (12) (2011) 2384–2394, doi:10.1016/j.combustflame.2011.05.013.
[39] S. Jaensch, M. Merk, E. Gopalakrishnan, S. Bomberg, T. Emmert, R. Sujith, W. Polifke, Hybrid CFD/low-o of nonlinear thermoacoustic oscillations, Proc. Combust. Inst. 36 (3) (2017) 3827–3834, doi:10.1016/j.proci.2016.08.006.
[40] E.T. Jaynes, Information theory and statistical mechanics, Phys. Rev. 106 (4) (1957) 620–630, doi:10.1103/PhysRev.106.620.
[41] L. Tay-Wo-Chong, S. Bomberg, A. Ulhaq, T. Komarek, W. Polifke, Comparative validation study on identification of premixed flame transfer function, J. Eng. Gas Turb. Power 134 (2) (2012) 021502–1–8, doi:10.1115/1.4004183.
[42] W. Polifke, Black-box system identification for reduced order model construction, Ann. Nucl. Energy 67C (2014) 109–128, doi:10.1016/j.anucene.2013.10.037.
[43] T. Emmert, S. Jaensch, C. Sovardi, W. Polifke, taX – a flexible tool for low-order duct acoustic simulation in time and frequency domain, 7th Forum Acusticum, DEGA, Krakow (2014).
[44] T. Emmert, M. Meindl, S. Jaensch, W. Polifke, Linear state space interconnect modeling of acoustic systems, Acta Acust. United Acust. 102 (5) (2016) 824–833, doi:10.3813/AAA.918997.
[45] T. Emmert, S. Bomberg, S. Jaensch, W. Polifke, Acoustic and intrinsic thermoacoustic modes of a premixed combustor, Proc. Combust. Inst. 36 (3) (2017) 3835–3842, doi:10.1016/j.proci.2016.08.002.
[46] A. Gentemann, A. Fischer, S. Evesque, W. Polifke, Acoustic transfer matrix reconstruction and analysis for ducts with sudden change of area, 9th AIAA/CEAS Aeroacoustics Conference, AIAA-2003-3142, AIAA, Hilton Head, SC, USA (2003), p. 11, doi:10.2514/6.2003-3142.

Quantification of the Impact of Uncertainties in Operating Conditions on the Flame Transfer Function With Nonintrusive Polynomial Chaos Expansion

Alexander Avdonin
Technische Universität München,
Fakultät für Maschinenwesen,
Garching b., München 85748, Germany
e-mail: avdonin@tfd.mw.tum.de

Wolfgang Polifke
Technische Universität München,
Fakultät für Maschinenwesen,
Garching b, München 85748, Germany

Nonintrusive polynomial chaos expansion (NIPCE) is used to quantify the impact of uncertainties in operating conditions on the flame transfer function (FTF) of a premixed laminar flame. NIPCE requires only a small number of system evaluations, so it can be applied in cases where a Monte Carlo simulation is unfeasible. We consider three uncertain operating parameters: inlet velocity, burner plate temperature, and equivalence ratio. The FTF is identified in terms of the finite impulse response (FIR) from computational fluid dynamics (CFD) simulations with broadband velocity excitation. NIPCE yields uncertainties in the FTF due to the uncertain operating conditions. For the chosen uncertain operating bounds, a second-order expansion is found to be sufficient to represent the resulting uncertainties in the FTF with good accuracy. The effect of each operating parameter on the FTF is studied using Sobol indices, i.e., a variance-based measure of sensitivity, which are computed from the NIPCE. It is observed that in the present case, uncertainties in the FIR as well as in the phase of the FTF are dominated by the equivalence-ratio uncertainty. For frequencies below 150 Hz, the uncertainty in the gain of the FTF is also attributable to the uncertainty in equivalence-ratio, but for higher frequencies, the uncertainties in velocity and temperature dominate. At last, we adopt the polynomial approximation of the output quantity, provided by the NIPCE method, for further uncertainty quantification (UQ) studies with modified input uncertainties.
[DOI: 10.1115/1.4040745]

Introduction

Thermoacoustic stability analysis should be an essential part of the design process of low-emission gas turbines. Typically, stability analysis is performed using low-order network models [1–5], which require a reliable model for the flow–flame interaction. Such a model can be provided in terms of the flame transfer function (FTF). The FTF can be obtained experimentally [6–8] or numerically [9–12]. Unfortunately, a lack of exact knowledge of operating conditions (such as inflow conditions or wall temperatures) yields uncertainties in the FTF, which should be quantified.

In this work, we show how to account for uncertain operating conditions in the identification of a flame transfer function from numerical simulations. We use nonintrusive polynomial chaos expansion (NIPCE) for that purpose. This method is particularly appealing in the industrial design process, since it treats the investigated system as a *black box*, so no modifications of the computational fluid dynamics (CFD) solver are required. In contrast to Monte Carlo simulations, NIPCE requires only a comparatively small number of CFD simulations (27 simulations in the present case), allowing uncertainty studies that would not be feasible otherwise. The method is easy to use, but constrained to a small number of uncertain parameters—typically less than ten.

Recently, we applied NIPCE in order to compute the uncertainties in the growth rate of thermoacoustic modes and validated the results against Monte Carlo simulation [13]. The present study focuses on uncertainty quantification (UQ) of a flame transfer function that is modeled as a finite impulse response (FIR) with uncertain coefficients. The uncertain FTF can be used to validate combustion simulations against experiments, where the operating conditions are not exactly known, or perform a more reliable stability analysis.

In the Flame Response Modeling section, we describe how we model the flame dynamics. Afterwards, we briefly describe the NIPCE methodology and explain how to use it for UQ of the flame model. Then, we perform a UQ study on a laminar flame with three uniformly distributed uncertain input parameters, i.e., inlet velocity, burner plate temperature, and equivalence ratio. Finally, we show how one may re-use the constructed uncertain flame model for a UQ study with input parameters that follow a distribution that is narrower and/or of a different type. Such a scenario could be relevant for an industrial development process, where input parameter uncertainties are initially large, but then reduce as the development evolves. A summary of results and an outlook on further investigations concludes the paper.

Flame Response Modeling. For longitudinal low-frequency instabilities, the flame can be considered as acoustically compact. In this case, details of the spatial distribution of heat release rate $\dot{q}$ are irrelevant for system stability, and it is sufficient to consider only the global heat release rate $\dot{Q}$. Typically, fluctuations of the global heat release rate $\dot{Q}'$ are related to velocity fluctuation u'_{ref} at a reference position upstream of the flame.

A simplistic flame response model is the n–τ model introduced by Crocco [14,15]: a flame responds with a certain gain n after a constant time delay τ to a perturbation u'_{ref}. This relation can be written in the time domain or the Laplace domain

Manuscript received June 26, 2018; final manuscript received June 28, 2018; published online September 17, 2018. Editor: Jerzy T. Sawicki.

$$\frac{\dot{Q}'(t)}{\bar{\dot{Q}}} = n\frac{u'_{\mathrm{ref}}(t-\tau)}{\bar{u}_{\mathrm{ref}}} \quad \text{or} \quad \frac{\hat{\dot{Q}}}{\bar{\dot{Q}}} = ne^{-s\tau}\frac{\hat{u}_{\mathrm{ref}}}{\bar{u}_{\mathrm{ref}}} \tag{1}$$

Here, the overline indicates time-averaged quantities, and the circumflex indicates the Laplace transform of fluctuating quantities. The Laplace variable $s = \varsigma + \mathrm{i}\omega$ comprises the growth rate $(-\varsigma)$, the imaginary number i, and the angular frequency ω.

In order to describe more realistic, nontrivial flame response functions, it has been proposed to generalize the n–τ model by regarding n and τ as functions of frequency. However, this idea has no sound physical justification and indeed the concept of a frequency-dependent time lag is ill-conceived. Instead, it is appropriate to model flame dynamics as a superposition of several time-lagged responses of varying strength with distributed time delays [16]. As a discrete-time signal, this superposition corresponds to a FIR model [17], which is used in this study for modeling the flame dynamics

$$\frac{\dot{Q}'[l]}{\bar{\dot{Q}}} = \sum_{k=0}^{N-1} b_k \frac{u_{\mathrm{ref}}[l-k]}{\bar{u}_{\mathrm{ref}}} \tag{2}$$

where $[l]$ indicates the lth discrete time-step, b_k are the FIR coefficients. Given the sampling time Δt, the time delay between lth and kth steps is $(l-k)\Delta t$, and the length of FIR is $N\Delta t$.

The finite impulse response can be z-transformed to a flame transfer function $\mathscr{F}(s)$

$$\mathscr{F}(s) = \sum_{k=0}^{N-1} b_k e^{-sk\Delta t} \tag{3}$$

Note that this FTF is defined for a Laplace variable s, see for instance [18]. Nevertheless, for graphical representation, the FTF is typically evaluated for purely imaginary values s, which corresponds to the angular frequency ω. In this case, one speaks of the flame frequency response (FFR) $F(\omega)$, since the response is evaluated only for frequencies with zero growth rate. The most common representation of the FFR is in terms of gain $||F(\omega)||$ and phase $\angle F(\omega)$, which are evaluated for an FIR model as

$$||F(\omega)|| = \left(\sum_{k=0}^{N-1}\sum_{l=0}^{N-1} b_k b_l e^{-\mathrm{i}\omega(k-l)\Delta t}\right)^{1/2} \tag{4}$$

$$\angle F(\omega) = \mathrm{atan2}\left(-\sum_{k=0}^{N-1} b_k \sin(\omega k\Delta t), \sum_{k=0}^{N-1} b_k \cos(\omega k\Delta t)\right) \tag{5}$$

If the flame response exceeds linearity limits, then it is typically modeled by a flame describing function [19,20], which can be represented as an FIR model with coefficients depending on excitation amplitude [21]. In this work, we focus on the linear regime, but in principle, the NIPCE method can also be applied to flame describing functions.

Nonintrusive Polynomial Chaos Expansion Methodology

Nonintrusive polynomial chaos expansion is an established method for UQ and is extensively documented and implemented in several open source software packages [22–24]. In this paper, we only briefly review the NIPCE methodology.

Uncertainty Quantification. Nonintrusive polynomial chaos expansion approximates an output quantity y as a truncated sum of multidimensional orthogonal polynomials Ψ_i of a number N uncertain input parameters $\underline{\xi} = [\xi_1, \xi_2, \ldots, \xi_N]$

$$y \cong \sum_{i=0}^{P-1} \alpha_i \Psi_i(\underline{\xi}) \tag{6}$$

where α_i are the weighting coefficients and P is the total number of expansion terms. The uncertain input parameters $\underline{\xi}$ are uncorrelated and standardized. If the uncertain input parameters are correlated, then they should be transformed into a reduced number of independent variables. The multidimensional polynomials $\Psi_i(\underline{\xi})$ are constructed using a tensor-product expansion of one-dimensional (1D) polynomials $\psi(\xi_j)$, i.e., the multidimensional polynomials are permutations of one-dimensional polynomials in all parameter dimensions. In this case, the total number of expansion terms P is constrained by one-dimensional polynomial-order bounds p_j for the jth uncertain input parameter

$$P = \prod_{j=1}^{N}(p_j + 1) \tag{7}$$

The above-mentioned tensor-product expansion supports anisotropy. Hence, the polynomial-order bounds p_j can be chosen independently for each uncertain parameter ξ_j. In this paper, we consider the same polynomial-order bounds for all uncertain input parameters $p = p_1 = p_2 = \ldots = p_N$. For brevity, we also refer to the NIPCE order as equal to the one-dimensional polynomial-order bound p, although the effective order of the NIPCE is Np due to the tensor-product expansion of the one-dimensional polynomials.

The choice of the one-dimensional polynomial $\psi(\xi_j)$ depends on the probability distribution of the uncertain input parameter ξ_j. Each probability distribution type has its own optimal polynomial type, as listed in Ref. [23]. Note that each ξ_j can follow its individual distribution.

In this study, we assume that all uncertain input parameters are uniformly distributed. Hence, according to Ref. [23], we use Legendre polynomials for the construction of the polynomial expansion. The Legendre polynomial of the k-th order can be computed using Rodrigues' formula [25]

$$\psi_k(\xi_j) = \frac{1}{2^k k!}\frac{d}{d\xi_j}\left[\left(\xi_j^2 - 1\right)^k\right] \tag{8}$$

For instance, a three-dimensional polynomial Ψ reads

$$\Psi(\xi_1, \xi_2, \xi_3) = \psi_i(\xi_1)\psi_j(\xi_2)\psi_k(\xi_3) \tag{9}$$

The polynomials Ψ_i are orthogonal. Hence, the weighting coefficients α_i of the expansion, defined in Eq. (6), are computed using a spectral projection

$$\alpha_i = \frac{\int_\Omega y\Psi_i\rho(\underline{\xi})d\underline{\xi}}{\int_\Omega \Psi_i^2\rho(\underline{\xi})d\underline{\xi}} \tag{10}$$

where Ω is the uncertain input parameter space. The joint probability density function (PDF) $\rho(\underline{\xi})$ is computed from one-dimensional probability density functions, since the uncertain input parameters are uncorrelated. The integral in the denominator of Eq. (10) is determined analytically, whereas the integral in the nominator is computed by a Gauss quadrature, which requires $p_j + 1$ quadrature points for exact integration in each dimension. If we consider, for instance, a three-dimensional polynomial with $p = 3$, then $(3+1)^3 = 64$ integration points are required to determine all coefficients of the expansion. Note that the integration points are strictly defined by the Gauss quadrature rules, and the points do not coincide for different polynomial orders.

The mean μ and variance σ^2 of the output quantity are defined as

$$\mu = E(y) = \int_\Omega y\rho(\underline{\xi})d\underline{\xi} \tag{11}$$

$$\sigma^2 = \mathrm{Var}(y) = \int_\Omega (y-\mu)^2 \rho(\underline{\xi}) d\underline{\xi} \tag{12}$$

Due to the orthogonality condition, it can be shown that the mean and variance are equal to the first two polynomial coefficients: $\mu = \alpha_0$ and $\sigma = \alpha_1$.

Sensitivity Analysis. The polynomial approximation of the output quantity makes possible the (approximate) analytical computation of *sensitivities*, i.e., derivatives of an output quantity with respect to input parameters

$$\frac{\partial y}{\partial \xi_i} = \sum_{j=0}^{P-1} \alpha_j \frac{\partial \Psi_j(\underline{\xi})}{\partial \xi_i} \tag{13}$$

These derivatives can be evaluated at the means of input parameters, or one can compute the mean and standard deviation of the derivatives. The latter approach was used for the growth-rate sensitivity analysis of thermoacoustic systems in a prior study [13].

In this study, we perform a derivative-free sensitivity analysis using variance-based sensitivity indices, also called Sobol indices [26]. They are a very effective tool to determine most critical uncertain parameters. Sobol indices S_{ξ_i} and $S_{\xi_i\xi_j\ldots}$ quantify contributions from each input parameter and from parameter interactions to the output variance

$$S_i = \frac{\mathrm{Var}(E(y|\xi_i))}{\mathrm{Var}(y)} \tag{14}$$

$$S_{ij} = \frac{\mathrm{Var}\big(E\big(y|\xi_i,\xi_j\big)\big)}{\mathrm{Var}(y)} - S_i - S_j \tag{15}$$

$$S_{ijk} = \frac{\mathrm{Var}\big(E\big(y|\xi_i,\xi_j,\xi_k\big)\big)}{\mathrm{Var}(y)} - S_i - S_j - S_{ij} - S_{ik} - S_{jk} \tag{16}$$

where $E(y|\ldots)$ is the conditional expectation. S_i is the individual contribution of parameter ξ_i, S_{ij}, and S_{ijk} are the contributions of interactions between parameters (ξ_i, ξ_j) and (ξ_i, ξ_j, ξ_k), respectively. The sum of all Sobol indices yields unity

$$\sum_{i=1}^{N} S_i + \sum_{i=1}^{N}\sum_{j>i}^{N} S_{ij} + \cdots + S_{1,2,\ldots,N} = 1 \tag{17}$$

We implemented NIPCE in MATLAB. Our implementation allows for an easy access to the polynomials and their postprocessing using the Symbolic Math Toolbox.

Application to Finite Impulse Response Model. Since the flame is modeled by an FIR (see Eq. (2)), uncertainties in FIR coefficients b_k are under investigation. Each coefficient is a function of uncertain inputs. NIPCE yields the polynomial approximation $b_k(\underline{\xi})$ as well as the mean $\bar{b}_k$ and standard deviation σ_{b_k}. Sobol indices of the FIR are computed analytically by integration of $b_k(\underline{\xi})$ according to Eqs. (14)–(16).

Uncertainty in the real part of the FFR may also be computed analytically

$$E(\mathrm{Re}(F(\omega))) = \sum_{k=0}^{N-1} \bar{b}_k \cos(-\omega k \Delta t) \tag{18}$$

$$\mathrm{Var}(\mathrm{Re}(F(\omega))) = \sum_{k=0}^{N-1}\sum_{l=0}^{N-1} \mathrm{cov}(b_k,b_l)\cos(\omega k\Delta t)\cos(\omega l \Delta t) \tag{19}$$

where $\bar{b}_k = E(b_k)$ and the covariance matrix $\mathrm{cov}(b_k,b_l) = E(b_k b_l) - \bar{b}_k\bar{b}_l$. For uncertainty in the imaginary part of the FFR, cos() should simply be replaced by sin() in Eqs. (18) and (19).

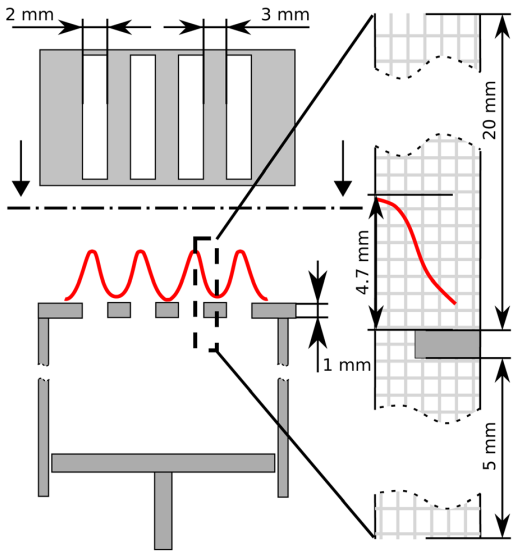

Fig. 1 Left: Sketch of the experimental test rig. Right: truncated CFD domain. Adapted from Ref. [13].

Unfortunately, we cannot propagate uncertainties in the FIR coefficients to the gain and phase of the FTF in a compact analytical form without additional assumptions, see Eqs. (4) and (5). Therefore, we apply a Monte Carlo simulation on the complex-valued frequency response function to access the statistical moments and Sobol indices for the gain and phase. Note that the Monte Carlo simulation takes at most a couple of minutes, since a single polynomial evaluation is very fast. The Global Sensitivity Analysis Toolbox [27] for MATLAB is used to compute Sobol indices numerically.

Computational Fluid Dynamics Model and Numerical Setup

We investigate the flame response of a laminar slit burner that was experimentally studied by Kornilov et al. [28]. The burner is fueled by the methane-air mixture. There are several numerical studies of the Kornilov flame [28–31]. A prior UQ study of a flame stability using NIPCE was also performed for the same setup [13].

The setup is sketched in Fig. 1. We simulate only one-half of a single flame in two-dimensional and use a truncated simulation domain with 65,700 structured cells. The flame is resolved with 18 cells in the streamwise direction.

For the CFD simulations, we use a weakly compressible low Mach number solver implemented in OPENFOAM [31]. This solver does not resolve the acoustics and suppresses thermoacoustic feedback, so no thermoacoustic instabilities can occur during simulations. The reaction is modeled by the two-step reaction mechanism 2S-CM2 [29].

The operating pressure is 101,325 Pa and the inlet temperature is 293 K. We consider uncertainty in three operating conditions: inlet velocity $u = 0.4 \pm 0.02$ m/s, burner plate temperature $T = 398 \pm 50$ K, and equivalence ratio $\phi = 0.8 \pm 0.1$. The uncertainty bounds are chosen in a rather generic way.[1] The uniform distribution was chosen, since it requires the least knowledge about the uncertain parameters: only the uncertainty bounds

[1]No information about uncertainties in the experiment was reported except of the burner plate temperature that was estimated to be between 373 K and 423 K.

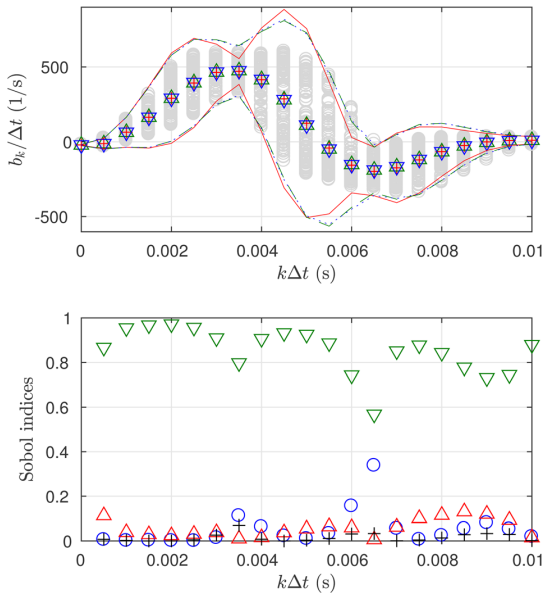

Fig. 2 Top: All identified firs used for construction of the NIPCEs (○); FIR represented by the mean coefficients and their confidence intervals $\pm 2.58\sigma$ for the NIPCE with $p=1$ (+, —), $p=2$ (△, - -), and $p=3$ (▽, ···). Bottom: sobol indices S_u (+), S_T (△), S_ϕ (▽), and $S_{T\phi}$ (○) for the NIPCE with $p=3$

should be defined. The three parameters are assumed independent. If the uncertain parameters are correlated, then they should be transformed into independent parameters.

Identification of the Flame Response

To estimate one flame impulse response, we perform one single CFD simulation with imposed broadband velocity excitation. We use MATLAB system identification (SI) toolbox for the FIR estimation. The identification process is well described by Tay-Wo-Chong et al. [12] or in the review of Polifke [17]. The length of a time series required for the identification is 0.25 s. That corresponds to roughly 24 h computation time on a 28-core Intel Xeon E5-2697 machine running at 2.6 GHz. The identified FIR model has 30 coefficients with the sampling time $\Delta t = 0.5$ ms.

The frequency response of the Kornilov flame as computed from the identified FIR was validated with good accuracy against experimental data and other numerical simulations in Refs. [13] and [30].

Results and Discussion

Due to high computational costs of CFD simulations, we cannot validate the NIPCE results against Monte Carlo simulation. Therefore, we use a sequence of increasing polynomial orders to judge the convergence. For convenience, we keep the same polynomial order for all uncertain inputs. We perform the NIPCE analysis with $p=1$, $p=2$, and $p=3$ resulting in 8, 27, and 64 CFD simulations, respectively.

Uniform Distribution. $p=1$ (—), $p=2$ (- -), AND $p=3$ (····) Fig. 2 (top) shows the mean FIR and confidence intervals given by $\pm 2.58\sigma$. These confidence intervals are often chosen, since they correspond to 99% probability assuming normally distributed output uncertainties. The NIPCE with $p=1$ predicts well the means of the FIR coefficients $\overline{b}_k$, but there are small differences in standard deviation σ_{b_k} to the NIPCE with $p=2$ and $p=3$ starting from the overshoot in the impulse response. The standard deviation is better predicted by the NIPCE with $p=2$ and $p=3$. In fact, the results do not significantly change from $p=2$ to $p=3$. Thus, we conclude that $p=2$ suffices to model the uncertainties in the FIR for the given uncertainty bounds.

Figure 2 (top) shows a typical flame behavior: the flame responses to the impulse velocity perturbation with the delayed increase of the heat release rate, followed by a restoration process. Both processes have time delays that are related to the convective transport of disturbances along the flame [32].

Figure 2 (top) also shows all FIR models used to construct the NIPCE. Some FIR coefficients are not symmetrically distributed around their means, and few coefficients lie outside of the $\pm 2.58\sigma$ confidence region for $t \approx 0.006$ s. Figure 3 shows the PDFs for six FIR coefficients that correspond to the impulse responses at six time-instants. PDFs are computed using a Monte Carlo simulation with 10^5 samples, which were enough to guarantee statistical convergence. PDFs do not follow a uniform or normal distribution; they show a rather complex shape with strong skewness or even two local maxima. Furthermore, the PDF shapes differ between the FIR coefficients considerably.

Four Sobol indices S_u, S_T, S_ϕ, and $S_{T\phi}$ are shown in Fig. 2 (bottom). S_{uT}, $S_{u\phi}$, S_{uT}, and $S_{uT\phi}$ are not shown, since their contributions are negligible. S_ϕ has the highest value for all FIR coefficients indicating that the uncertainty in equivalence ratio dominates other contributions. The second important contribution comes from the coupling terms between T and ϕ at the overshoot and undershoot of the impulse response.

According to Eqs. (18) and (19), the uncertainty in complex-valued FFR can be computed analytically from the uncertain FIR coefficients. Figure 4 shows the complex-valued frequency response function. All polynomials predict well the mean frequency response, but the NIPCE with $p=2$ and $p=3$ are better in the prediction of the standard deviation.

As mentioned in section *NIPCE Methodology*, we cannot analytically propagate the uncertainties from the complex-valued FFR to gain and phase. Thus, we perform again a Monte Carlo simulation with 10^5 samples to compute uncertainties in the gain and phase, which are shown in Fig. 5. The flame frequency response shows a typical behavior with an excess gain around 100 Hz. For higher frequencies, the gain decreases and roughly at 300 Hz the flame, practically does not respond to velocity fluctuations. The phase is decaying with an almost constant slope determined by the characteristic time delays in the finite impulse response.

The NIPCE with $p=1$ reproduces well the mean of the gain and phase, but overestimates the standard deviation in the gain by roughly a factor of 2 between 100 Hz and 300 Hz in comparison to the NIPCE with $p=2$ and $p=3$. Thus, to model the uncertainty in the gain, we need at least a second-order polynomial. The phase uncertainty grows with frequency and becomes very large for high frequencies. For frequencies below 300 Hz, all three

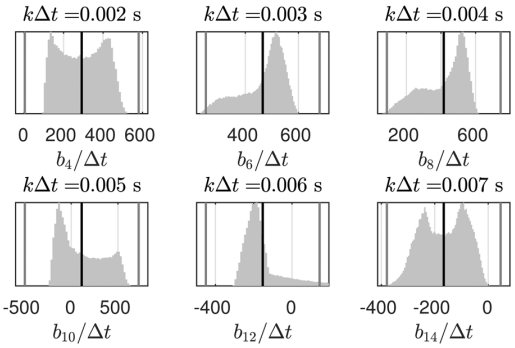

Fig. 3 Probability density function (of FIR coefficients with the mean (—) and confidence intervals $\pm 2.58\sigma$ (═)

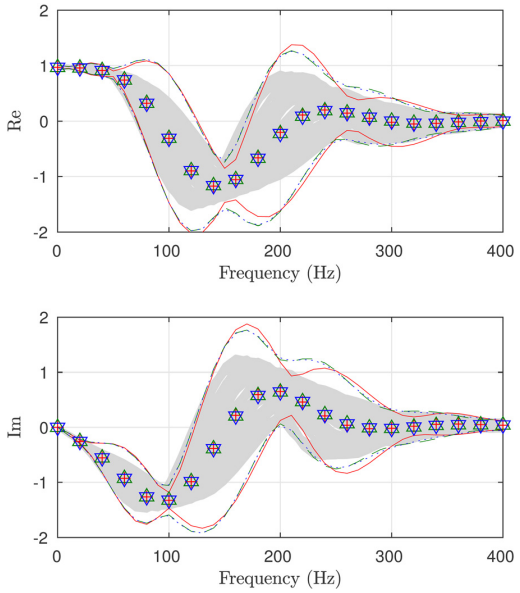

Fig. 4 Complex-valued frequency response of all identified firs used for construction of the NIPCES (—). Mean FFR and its confidence intervals $\pm 2.58\sigma$ for the NIPCE with $p=1$ (+, —), $p=2$ (+, —), $p=2$ (△, - -) AND $p=3$ (▽, ···).

polynomials yield almost the same standard deviation. Starting from 300 Hz, the heat release rate is close to zero and might change the sign, switching the phase by 180 deg. Therefore, the phase uncertainty drastically increases where the gain is close to zero. Such a problem does not exist in a complex-valued representation of the FFR, see Fig. 4.

Frequency responses of all identified FIRs used for the NIPCE construction lie within the $\pm 2.58\sigma$ confidence region. This observation is supported by Fig. 6, which shows PDFs of the gain for six different frequencies. All PDFs fit well into the confidence regions. Furthermore, the last four of them are even almost symmetric.

The Sobol indices of the NIPCE with $p=3$ are shown in Fig. 5 (bottom). We do not consider frequencies above 300 Hz, since the gain is almost zero there. For frequencies below 150 Hz, the gain uncertainty is mostly due to equivalence-ratio uncertainty. For higher frequencies, the gain uncertainty is mainly governed by the velocity and temperature. This result is remarkable, since the uncertainty in all FIR coefficients is mostly due to the equivalence ratio (see Fig. 2). Such a change in the Sobol indices occurs due to the interaction of uncertainties in the FIR coefficients while propagating to the gain of the FTF. The Sobol indices for the phase are similar to these of the FIR coefficients: S_ϕ and $S_{T\phi}$ dominate.

The reader should keep in mind that Sobol indices always correspond to a particular set of input uncertainties and their bounds. Any modification of input-uncertainty bounds or distribution type results in changes in Sobol indices.

Input-Uncertainty Modification. Since NIPCE yields a polynomial approximation of the output quantity, it can be adopted for further UQ studies with modified input uncertainties. This might be beneficial during a design process, where details of the input uncertainties are not known a priori and have to be redefined several times. In a first iteration of the UQ study, the NIPCE should be constructed assuming a uniform distribution with comparatively large uncertainty bounds for all input parameters, reflecting the fact that at the beginning of a design process uncertainties are typically high. The uniform distribution provides the best starting

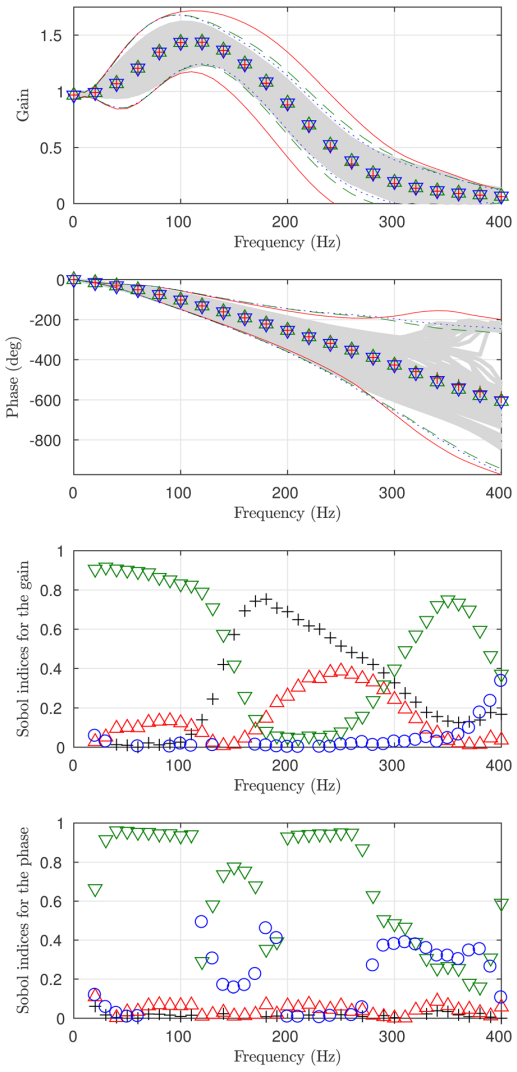

Fig. 5 Top: frequency response of all identified FIRS used for construction of the NIPCES (—); mean FFR and its confidence intervals $\pm 2.58\sigma$ for the NIPCE with $p=1$ (+,—), $p=2$ (△, - -), and $p=3$ (▽, ···). Bottom: Sobol indices S_u (+), S_T (△), S_ϕ (▽), and $S_{T\phi}$ (○) for the NIPCE with $p=3$.

point for this situation, since it aims for a polynomial that is approximated with equal accuracy in the entire parameter space. In subsequent studies, as more and refined information on input parameter values becomes available, one would take a smaller parameter space: reduce the number of parameters or decrease the parameter bounds. One could even change the parameter distribution type. The mean and variance of the output quantity have to be manually computed integrating the polynomial according to Eqs. (11) and (12) with the corresponding joint probability density function $\rho(\xi)$ and parameter space Ω. Certainly, the approximation quality might reduce: small-scale features that are not captured on a larger domain might become important on a smaller domain. Thus, several polynomials with increasing order should be investigated to ensure converged results.

For proof of concept, we use the previously constructed NIPCEs to propagate reduced input uncertainties that are either normally or uniformly distributed. The normal input distribution is

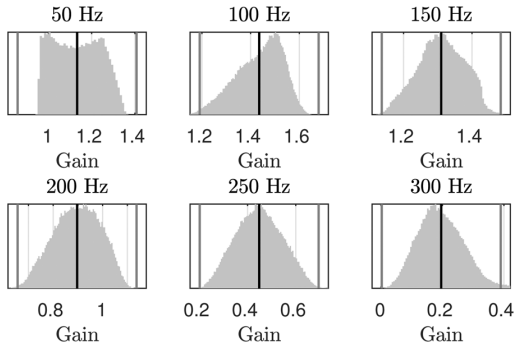

Fig. 6 Probability density function of frequency response with the mean (—) and confidence intervals $\pm 2.58\sigma$ (▬)

defined such that its 99% confidence interval is equal to the parameter space of the prior uniform input distribution: $2.58\sigma_u = 0.02$ m/s, $2.58\sigma_T = 50$ K, and $2.58\sigma_\phi = 0.1$. The new uniform distribution has the same standard deviation as this normal distribution, resulting in $u = 0.4 \pm 0.0134$ m/s, $T = 398 \pm 34$ K, and $\phi = 0.8 \pm 0.067$. Choosing the same standard deviations for the two modified input uncertainties allows us to study the effect of the distribution type.

Figure 7 shows uncertainty in the FIR coefficients for normally (top) and uniformly distributed input parameters (bottom). For both distributions, the NIPCE with $p = 1$ underestimates the standard deviation and shows slightly different mean values in comparison to $p = 2$ and $p = 3$. The NIPCE with $p = 2$ and $p = 3$ perform similarly and yields almost the same results. Therefore, we conclude that the NIPCE with $p = 2$, constructed originally for the uniformly distributed inputs with larger uncertainties, can be used in this case for both uniform and normal distributions with reduced uncertainties.

The mean FIR coefficients as well as their standard deviations are almost identical for uniformly and normally distributed inputs.

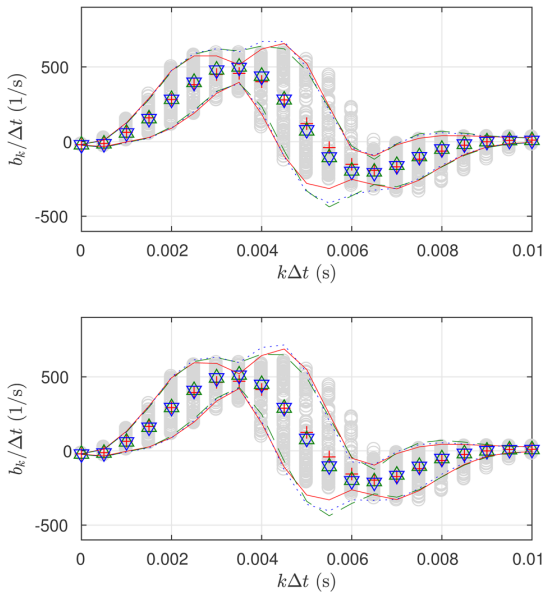

Fig. 7 Mean FIR with confidence intervals $\pm 2.58\sigma$ for reduced input-parameter uncertainties with normal distribution (top) and uniform distribution (bottom) cf. Fig. 2

Hence, we conclude that exact knowledge of the input distribution type is not crucial for the present UQ study. It is more important to specify the correct standard deviation of the input uncertainties.

Joint Uncertainty From Operating Conditions and System Identification. In general, SI *estimates* a model, i.e., the SI results are inherently uncertain. Since we consider a laminar flame in this study and carry on the CFD simulation for a significant number of flame time scales, the FIRs are identified with a very low uncertainty (fit to estimation data more than 97%). In this case, the uncertainty due to the SI process is negligible in comparison to the uncertainty coming from operating conditions: $\sigma_{\text{NIPCE}}/\sigma_{\text{SI}} \approx 10 - 100$.

However, the uncertainty of SI results is likely to become significant for large eddy simulation of turbulent flames, due to noise that results from resolved turbulent fluctuations, and due to the fact that long time series entail very significant computational costs [33]. In this case, one is advised to consider joint uncertainties from operating conditions as well as system identification. Unfortunately, it is not obvious how to do that. In a worst-case scenario, which is the easiest case to consider, one may assume that uncertainties are independent. Then, the joint uncertainty results in $\sigma = (\sigma_{\text{NIPCE}}^2 + \sigma_{\text{SI}}^2)^{1/2}$. Since σ_{SI} might vary between the FIR samples, which are required for the NIPCE construction, one could average σ_{SI} over all the samples or take its maximum value.

Summary and Outlook

Most UQ studies in thermoacoustics have focused on Helmholtz equation [34–38] or on low-order network models. In both cases, Monte Carlo simulation is feasible for UQ validation. In the current work as in Ref. [13], we made a step further by studying the uncertainty in the case for which Monte Carlo simulation is no longer possible due to high computational costs. We used non-intrusive polynomial chaos expansion for UQ because it converges after a small number of CFD simulations and thus allows for the investigation of computationally expensive problems.

We studied uncertainty in the flame transfer function due to uncertainties in operating conditions. We considered three uniformly distributed uncertain input parameters: inlet velocity, burner plate temperature, and equivalence ratio. Using the NIPCE method, we modeled the flame by a finite impulse response with uncertain coefficients. Then, we propagated uncertainties in the FIR coefficients to a flame frequency response. The second-order polynomial, constructed from 27 CFD simulations, was enough to model the uncertainties.

To quantify uncertainty contributions of each single input parameter and their combinations, we introduce Sobol indices. For the chosen uncertain operating bounds, the uncertainty in the finite impulse response as well as in the phase of the frequency response was mostly attributed to the equivalence-ratio uncertainty. At frequencies below 150 Hz, uncertainty in the gain of the frequency response was also dominated by the equivalence ratio. For higher frequencies uncertainties in velocity and temperature were dominant. Note that these results cannot be generalized, since they strictly belong to the distribution of the input uncertainties assumed in this study.

We showed that a polynomial, constructed for a UQ study with uniformly distributed input, can be used for other UQ studies with smaller input uncertainties. For that purpose, we additionally considered normal and uniform input distributions with the same standard deviations. The uncertainty in the finite impulse response was affected by the standard deviation of the inputs, but not by the input distribution type.

We briefly outlined a simple way to combine uncertainties coming from operating conditions and from FIR identification, if these uncertainties are assumed independent. In case of a laminar flame, uncertainty due to identification process is negligible, so the joint uncertainty can be safely neglected. The next step could be to study turbulent flames. Turbulence increases the uncertainty

due to FIR identification procedure, thereby necessitating evaluation of the joint uncertainty. Given that identification of the turbulent flame response requires significant computational resources, one could reduce the number of uncertain parameters to two in a worst case scenario. In that case, only 9 instead of 27 CFD simulations would be required to construct a second-order NIPCE.

Acknowledgment

The authors gratefully acknowledge Leibniz Supercomputing Centre for providing access to HPC resources (Linux-Cluster). We would also like to thank Armin Witte for a valuable discussion about the uncertainty in the flame transfer function.

Nomenclature

b = finite impulse response coefficient
cov = covariance
E = expected value
f = frequency (Hz)
F = flame frequency response (FFR)
$\mathcal{F}$ = flame transfer function (FTF)
i = imaginary number
i, j, k, l = indices
Im = imaginary part
n = gain of the n–τ model
N = number of uncertain input parameters
p = one-dimensional polynomial-order bound
P = total number of expansion terms
$\dot{q}$ = local heat release rate (W/m^3)
$\dot{Q}$ = global heat release rate (W)
Re = real part
s = Laplace variable
S = Sobol index
t = time (s)
T = temperature (K)
u = velocity (m/s)
Var = variance
y = output quantity
α = polynomial weighting coefficient
Δt = sampling time (s)
μ = mean
ξ = uncertain input parameter
ρ = probability density function
σ = standard deviation
$-\varsigma$ = growth rate (rad / s)
τ = time delay of the n–τ model (s)
ϕ = equivalence ratio
Ψ = multidimensional orthogonal polynomial
ψ = one-dimensional orthogonal polynomial
ω = angular frequency (rad/s)
$\underline{\Omega}$ = uncertain input parameter space
$\overline{()}$ = mean or time-averaged quantity
$()'$ = fluctuating quantity
$\hat{()}$ = Laplace transformed quantity

References

[1] Stow, S. R., and Dowling, A. P., 2001, "Thermoacoustic Oscillations in an Annular Combustor," ASME Paper No. 2001-GT-0037.
[2] Nicoud, F., Benoit, L., Sensiau, C., and Poinsot, T., 2007, "Acoustic Modes in Combustors With Complex Impedances and Multidimensional Active Flames," AIAA J., **45**(2), pp. 426–441.
[3] Emmert, T., Jaensch, S., Sovardi, C., and Polifke, W., 2014, "taX—A Flexible Tool for Low-Order Duct Acoustic Simulation in Time and Frequency Domain," Seventh Forum Acusticum, Kraków, Poland, Sept. 7–12.
[4] Li, J., and Morgans, A. S., 2015, "Time Domain Simulations of Nonlinear Thermoacoustic Behaviour in a Simple Combustor Using a Wave-Based Approach," J. Sound Vib., **346**, pp. 345–360.
[5] Emmert, T., Meindl, M., Jaensch, S., and Polifke, W., 2016, "Linear State Space Interconnect Modeling of Acoustic Systems," Acta Acust. Acust., **102**(5), pp. 824–833.
[6] Ducruix, S., Durox, D., and Candel, S., 2000, "Theoretical and Experimental Determinations of the Transfer Function of a Premixed Laminar Flame," Proc. Combust. Inst., **28**(1), pp. 765–773.
[7] Kunze, K., Hirsch, C., and Sattelmayer, T., 2004, "Transfer Function Measurements on a Swirl Stabilized Premix Burner in an Annular Combustion Chamber," ASME Paper No. GT2004-53106.
[8] Kim, K. T., Lee, H. J., Lee, J. G., Quay, B. D., and Santavicca, D., 2009, "Flame Transfer Function Measurement and Instability Frequency Prediction Using a Thermoacoustic Model," ASME Paper No. GT2009-60026.
[9] Bohn, D., Deutsch, G., and Krüger, U., 1998, "Numerical Prediction of the Dynamic Behaviour of Turbulent Diffusion Flames," ASME J. Eng. Gas Turbines Power, **120**(4), pp. 713–720.
[10] Gentemann, A. M. G., Hirsch, C., Kunze, K., Kiesewetter, F., Sattelmayer, T., and Polifke, W., 2004, "Validation of Flame Transfer Function Reconstruction for Perfectly Premixed Swirl Flames," ASME Paper No. GT-2004-53776.
[11] Zhu, M., Dowling, A. P., and Bray, K. N. C., 2005, "Transfer Function Calculations for Aeroengine Combustion Oscillations," ASME J. Eng. Gas Turbines Power, **127**(1), pp. 18–26.
[12] Tay-Wo-Chong, L., Bomberg, S., Ulhaq, A., Komarek, T., and Polifke, W., 2012, "Comparative Validation Study on Identification of Premixed Flame Transfer Function," ASME J. Eng. Gas Turbines Power, **134**(2), p. 021502.
[13] Avdonin, A., Jaensch, S., Silva, C. F., Češnovar, M., and Polifke, W., 2018, "Uncertainty Quantification and Sensitivity Analysis of Thermoacoustic Stability With Non-Intrusive Polynomial Chaos Expansion," Combust. Flame, **189**, pp. 300–310.
[14] Crocco, L., 1951, "Aspects of Combustion Stability in Liquid Propellant Rocket Motors—Part1: Fundamentals. Low Frequency Instability With Monopropellants," J. Am. Rocket Soc., **21**(6), pp. 163–178.
[15] Crocco, L., 1952, "Aspects of Combustion Stability in Liquid Propellant Rocket Motors—Part 2: Low Frequency Instability With Bipropellants. High Frequency Instability," J. Am. Rocket Soc., **22**(1), pp. 7–16.
[16] Subramanian, P., Blumenthal, R. S., Sujith, R., and Polifke, W., 2015, "Distributed Time Lag Response Functions for the Modelling of Combustion Dynamics," Combust. Theory Modell., **19**(2), pp. 223–237.
[17] Polifke, W., 2014, "Black-Box System Identification for Reduced Order Model Construction," Ann. Nucl. Energy, **67**, pp. 109–128.
[18] Emmert, T., Bomberg, S., and Polifke, W., 2015, "Intrinsic Thermoacoustic Instability of Premixed Flames," Combust. Flame, **162**(1), pp. 75–85.
[19] Dowling, A. P., 1997, "Nonlinear Self-Excited Oscillations of a Ducted Flame," J. Fluid Mech., **346**, pp. 271–290.
[20] Noiray, N., Durox, D., Schuller, T., and Candel, S., 2008, "A Unified Framework for Nonlinear Combustion Instability Analysis Based on the Flame Describing Function," J. Fluid Mech., **615**, pp. 139–167.
[21] Gopinathan, S. M., Iurashev, D., Bigongiari, A., and Heckl, M., 2017, "Nonlinear Analytical Flame Models With Amplitude-Dependent Time-Lag Distributions," Int. J. Spray Combust. Dyn. (epub).
[22] Andrianov, G., Burriel, S., Cambier, S., Dutfoy, A., Dutka-Malen, I., de Rocquigny, E., Sudret, B., Benjamin, P., Lebrun, R., Mangeant, F., and Pendola, M., 2007, "Open TURNS, an Open Source Initiative to Treat Uncertainties, Risks'N Statistics in a Structured Industrial Approach," European Safety and Reliability Conference, Risk, Reliability and Societal Safety (ESREL), Stavenger, Norway, June 25–27, pp. 1–7.
[23] Adams, B. M., Bohnhoff, W., Dalbey, K., Eddy, J., Eldred, M., Gay, D., Haskell, K., Hough, P. D., and Swiler, L., 2009, "DAKOTA, a Multilevel Parallel Object-Oriented Framework for Design Optimization, Parameter Estimation, Uncertainty Quantification, and Sensitivity Analysis: Version 5.0 User's Manual," Sandia National Laboratories, Livermore, CA, Technical Report No. SAND2010-2183.
[24] Feinberg, J., and Langtangen, H. P., 2015, "Chaospy: An Open Source Tool for Designing Methods of Uncertainty Quantification," J. Comput. Sci., **11**(Suppl. C), pp. 46–57.
[25] Rodrigues, O., 1816, "De L'attraction Des Sphéroïdes," Corresp. Sur. Éc. Imp. Polytech., **3**(3), pp. 361–385.
[26] Sobol', I., 1993, "Sensitivity Estimates for Nonlinear Mathematical Models," Math. Model. Comput. Exp., **1**(4), pp. 407–414.
[27] Cannavó, F., 2012, "Sensitivity Analysis for Volcanic Source Modeling Quality Assessment and Model Selection," Comput. Geosci., **44**(Suppl. C), pp. 52–59.
[28] Kornilov, V. N., Rook, R., ten Thije Boonkkamp, J. H. M., and de Goey, L. P. H., 2009, "Experimental and Numerical Investigation of the Acoustic Response of Multi-Slit Bunsen Burners," Combust. Flame, **156**(10), pp. 1957–1970.
[29] Duchaine, F., Boudy, F., Durox, D., and Poinsot, T., 2011, "Sensitivity Analysis of Transfer Functions of Laminar Flames," Combust. Flame, **158**(12), pp. 2384–2394.
[30] Silva, C. F., Emmert, T., Jaensch, S., and Polifke, W., 2015, "Numerical Study on Intrinsic Thermoacoustic Instability of a Laminar Premixed Flame," Combust. Flame, **162**(9), pp. 3370–3378.
[31] Jaensch, S., Merk, M., Gopalakrishnan, E., Bomberg, S., Emmert, T., Sujith, R., and Polifke, W., 2017, "Hybrid CFD/Low-Order Modeling of Nonlinear Thermoacoustic Oscillations," Proc. Combust. Inst., **36**(3), pp. 3827–3834.
[32] Blumenthal, R. S., Subramanian, P., Sujith, R., and Polifke, W., 2013, "Novel Perspectives on the Dynamics of Premixed Flames," Combust. Flame, **160**(7), pp. 1215–1224.
[33] Guo, S., Silva, C. F., Ghani, A., and Polifke, W., 2018, "Quantification and Propagation of Uncertainties in Identification of Flame Impulse Response for Thermoacoustic Stability Analysis," ASME Paper No. GT2018-75644.

[34] Ndiaye, A., Bauerheim, M., and Nicoud, F., 2015, "Uncertainty Quantification of Thermoacoustic Instabilities on a Swirled Stabilized Combustor," ASME Paper No. GT2015-44133.
[35] Bauerheim, M., Ndiaye, A., Constantine, P., Moreau, S., and Nicoud, F., 2016, "Symmetry Breaking of Azimuthal Thermoacoustic Modes: The UQ Perspective," J. Fluid Mech., **789**, pp. 534–566.
[36] Magri, L., Bauerheim, M., Nicoud, F., and Juniper, M. P., 2016, "Stability Analysis of Thermo-Acoustic Nonlinear Eigenproblems in Annular Combustors—Part II: Uncertainty Quantification," J. Comput. Phys., **325**, pp. 411–421.
[37] Silva, C., Magri, L., Runte, T., and Polifke, W., 2017, "Uncertainty Quantification of Growth Rates of Thermoacoustic Instability by an Adjoint Helmholtz Solver," ASME J. Eng. Gas Turbines Power, **139**(1), p. 011901.
[38] Mensah, G. A., Magri, L., and Moeck, J. P., 2017, "Methods for the Calculation of Thermoacoustic Stability Margins and Monte Carlo-Free Uncertainty Quantification," ASME Paper No. GT2017-64829.

Bibliography

[1] B. M. Adams, W. Bohnhoff, K. Dalbey, J. Eddy, M. Eldred, D. Gay, K. Haskell, P. D. Hough, and L. Swiler. DAKOTA, a multilevel parallel object-oriented framework for design optimization, parameter estimation, uncertainty quantification, and sensitivity analysis: Version 5.0 user's manual. *Sandia National Laboratories, Tech. Rep. SAND2010-2183*, 2009.

[2] A. Albayrak and W. Polifke. An analytical model based on the G-equation for the response of technically premixed flames to perturbations of equivalence ratio. *Int. J. Spray Comb. Dynamics*, 10(2):103–110, June 2018. doi: 10.1177/1756827717740776.

[3] A. Albayrak, R. S. Blumenthal, A. Ulhaq, and W. Polifke. An Analytical Model for the Impulse Response of Laminar Premixed Flames to Equivalence Ratio Perturbations. *Proceedings of the Combustion Institute*, 36(3):3725–3732, 2017. ISSN 1540-7489. doi: 10.1016/j.proci.2016.06.002.

[4] P. R. Amestoy, I. S. Duff, J.-Y. L'Excellent, and J. Koster. MUMPS: A General Purpose Distributed Memory Sparse Solver. In T. Sørevik, F. Manne, A. H. Gebremedhin, and R. Moe, editors, *Applied Parallel Computing. New Paradigms for HPC in Industry and Academia*, number 1947 in Lecture Notes in Computer Science, pages 121–130. Springer Berlin Heidelberg, June 2000. ISBN 978-3-540-41729-3 978-3-540-70734-9. doi: 10.1007/3-540-70734-416.

[5] G. Andrianov, S. Burriel, S. Cambier, A. Dutfoy, I. Dutka-Malen, E. de Rocquigny, B. Sudret, P. Benjamin, R. Lebrun, F. Mangeant, and M. Pendola. Open TURNS, an open source initiative to Treat Uncertainties, Risks'N Statistics in a structured industrial approach. In *Proceedings of the European Safety and Reliability Conference 2007, ESREL 2007 - Risk, Reliability and Societal Safety*, volume 2, Jan. 2007.

[6] A. Avdonin and W. Polifke. LES-basierte Analyse hochfrequenter Verbrennungsinstabilitäten. Abschlussbericht COOREFLEX 03ET7021U, 2018.

[7] A. Avdonin, A. Javareshkian, and W. Polifke. Prediction of premixed flame dynamics using LES with tabulated chemistry and Eulerian stochastic fields. In *ASME Turbo Expo 2019: Turbomachinery Technical Conference and Exposition*, GT2019-90140, Phoenix, USA, 2019.

[8] A. Avdonin, A. Javareshkian, and W. Polifke. Prediction of premixed flame dynamics using LES with tabulated chemistry and Eulerian stochastic fields. *J. Eng. Gas Turbines Power*, 141(11), 2019.

[9] M. Bauerheim, A. Ndiaye, P. Constantine, S. Moreau, and F. Nicoud. Symmetry breaking of azimuthal thermoacoustic modes: The UQ perspective. *Journal of Fluid Mechanics*, 789:534–566, Feb. 2016. ISSN 0022-1120, 1469-7645. doi: 10.1017/jfm.2015.730.

[10] T. Benaziz. *Sensitivity Analysis of a One-Dimensional Laminar Flame*. Master's Thesis, Technical University of Munich, 2015.

[11] A. C. Benim and K. J. Syed. Laminar Flamelet Modelling of Turbulent Premixed Combustion. *Applied Mathematical Modelling*, 22:113–136, 1998.

[12] F. M. Berger, T. Hummel, M. Hertweck, J. Kaufmann, B. Schuermans, and T. Sattelmayer. High-Frequency Thermoacoustic Modulation Mechanisms in Swirl-Stabilized Gas Turbine Combustors—Part I: Experimental Investigation of Local Flame Response. *Journal of Engineering for Gas Turbines and Power*, 139(7):071501–071501–9, Feb. 2017. ISSN 0742-4795. doi: 10.1115/1.4035591.

[13] F. M. Berger, T. Hummel, B. Schuermans, and T. Sattelmayer. Pulsation-Amplitude-Dependent Flame Dynamics of High-Frequency Thermoacoustic Oscillations in Lean-Premixed Gas Turbine Combustors. *Journal of Engineering for Gas Turbines and Power*, 140(4):041507–041507–10, Nov. 2017. ISSN 0742-4795. doi: 10.1115/1.4038036.

[14] M. Bertsch. *Evaluation of Impedance Boundary Conditions in ANSYS Fluent*. Semester Thesis, Technical University of Munich, 2017.

[15] J. Bibrzycki, T. Poinsot, and A. Zajdel. Investigation of Laminar Flame Speed of CH4/N2/O2 and CH4/CO2/O2 Mixtures Using Reduced Chemical Kinetic Mechanisms. *Archivum combustionis*, 30(4):287–296, 2010.

[16] T. Bieniek. *Comparative LES Study of Partially Premixed Sandia Flames Based on Alternative Progress Variable Definitions in the Context of the Flamelet/Progress Variable Combustion Model*. Master's Thesis, Technical University of Munich, 2017.

[17] M. Blanchard, T. Schuller, D. Sipp, and P. J. Schmid. Response Analysis of a Laminar Premixed M-Flame to Flow Perturbations Using a Linearized Compressible Navier-Stokes Solver. *Physics of Fluids*, 27(4):043602, Apr. 2015. ISSN 1070-6631, 1089-7666. doi: 10.1063/1.4918672.

[18] D. Bradley and A. K. C. Lau. The mathematical modelling of premixed turbulent combustion. *Pure and Appl. Chem*, 62(5):803–814, 1990.

[19] M. Brandt, W. Polifke, B. Ivancic, P. Flohr, and B. Paikert. Auto-Ignition in a Gas Turbine Burner at Elevated Temperature. In *Int'l Gas Turbine and Aeroengine Congress & Exposition*, ASME 2003-GT-38224, Atlanta, GA, U.S.A., June 2003.

[20] M. Češnovar. *Implementation of an Uncertainty Quantification Tool in MATLAB*. Semester Thesis, Technical University of Munich, 2016.

[21] J. H. Cho and T. C. Lieuwen. Laminar Premixed Flame Response to Equivalence Ratio Oscillations. *Combustion and Flame*, 140(1-2):116–129, 2005. doi: 10.1016/j.combustflame.2004.10.008.

[22] B.-T. Chu. On the generation of pressure waves at a plane flame front. *Symposium (International) on Combustion*, 4(1):603–612, Jan. 1953. doi: 10.1016/S0082-0784(53)80081-0.

[23] B. Cockburn, S.-Y. Lin, and C.-W. Shu. TVB Runge-Kutta local projection discontinuous Galerkin finite element method for conservation laws III: One-dimensional systems. *Journal of Computational Physics*, 84(1):90–113, Sept. 1989. ISSN 00219991. doi: 10.1016/0021-9991(89)90183-6.

[24] B. Cockburn, G. E. Karniadakis, and C.-W. Shu. The Development of Discontinuous Galerkin Methods. In *Discontinuous Galerkin Methods*, Lecture Notes in Computational Science and Engineering, pages 3–50. Springer, Berlin, Heidelberg, 2000. ISBN 978-3-642-64098-8 978-3-642-59721-3. doi: 10.1007/978-3-642-59721-3_1.

[25] P. Constantine, E. Dow, and Q. Wang. Active Subspace Methods in Theory and Practice: Applications to Kriging Surfaces. *SIAM Journal on Scientific Computing*, 36(4):A1500–A1524, Jan. 2014. ISSN 1064-8275. doi: 10.1137/130916138.

[26] L. Crocco. Aspects of Combustion Stability in Liquid Propellant Rocket Motors Part1: Fundamentals. Low frequency instability with monopropellants. *Journal of the American Rocket Society*, 21(6):163–178, 1951. doi: 10.2514/8.4393.

[27] L. Crocco. Aspects of Combustion Stability in Liquid Propellant Rocket Motors Part 2: Low Frequency Instability with Bipropellants. High Frequency Instabilitiy. *Journal of American Rocket Society*, 22(1):7–16, 1952. doi: 10.2514/8.4410.

[28] F. E. C. Culick. Stability of high-frequency pressure oscillations in rocket combustion chambers. *AIAA Journal*, 1(5):1097–1104, May 1963. ISSN 0001-1452. doi: 10.2514/3.1730.

[29] L. P. H. De Goey and J. H. M. ten Thije Boonkkamp. A flamelet description of premixed laminar flames and the relation with flame stretch. *Combustion and flame*, 119(3):253–271, 1999. ISSN 0010-2180.

[30] P. Domingo, L. Vervisch, and D. Veynante. Auto-ignition and flame propagation effects in LES of burned gases diluted turbulent combustion. In *Proceedings of the 2006 Summer Program*, pages 337–348. Center for Turbulence Research, Stanford University / NASA Ames Research Center,, 2006.

[31] T. Emmert, S. Jaensch, C. Sovardi, and W. Polifke. taX - a Flexible Tool for Low-Order Duct Acoustic Simulation in Time and Frequency Domain. In *7th Forum Acusticum*, Krakow, Sept. 2014. DEGA.

[32] T. Emmert, S. Bomberg, and W. Polifke. Intrinsic Thermoacoustic Instability of Premixed Flames. *Combustion and Flame*, 162(1):75–85, 2015. ISSN 0010-2180. doi: 10.1016/j.combustflame.2014.06.008.

[33] T. Emmert, M. Meindl, S. Jaensch, and W. Polifke. Linear State Space Interconnect Modeling of Acoustic Systems. *Acta Acustica united with Acustica*, 102(5):824–833, 2016. doi: 10.3813/AAA.918997.

[34] S. Evesque and W. Polifke. Low-Order Acoustic Modelling for Annular Combustors: Validation and Inclusion of Modal Coupling. In *Volume 1: Turbo Expo 2002*, ASME GT-2002-30064, pages 321–331, Amsterdam, The Netherlands, 2002. ASMEDC. doi: 10.1115/GT2002-30064.

[35] J. Feinberg and H. P. Langtangen. Chaospy: An open source tool for designing methods of uncertainty quantification. *Journal of Computational Science*, 11(Supplement C):46–57, Nov. 2015. ISSN 1877-7503. doi: 10.1016/j.jocs.2015.08.008.

[36] B. Fiorina, R. Baron, O. Gicquel, D. Thevenin, S. Carpentier, and N. Darabiha. Modelling non-adiabatic partially premixed flames using flame-prolongation of ILDM. *Combustion Theory and Modelling*, 7(3):449–470, Sept. 2003. ISSN 1364-7830. doi: 10.1088/1364-7830/7/3/301.

[37] B. Fiorina, R. Mercier, G. Kuenne, A. Ketelheun, A. Avdić, J. Janicka, D. Geyer, A. Dreizler, E. Alenius, C. Duwig, P. Trisjono, K. Kleinheinz, S. Kang, H. Pitsch, F. Proch, F. Cavallo Marincola, and A. Kempf. Challenging modeling strategies for LES of non-adiabatic turbulent stratified combustion. *Combustion and Flame*, 162(11):4264–4282, Nov. 2015. ISSN 0010-2180. doi: 10.1016/j.combustflame.2015.07.036.

[38] J. Galpin, A. Naudin, L. Vervisch, C. Angelberger, O. Colin, and P. Domingo. Large-eddy simulation of a fuel-lean premixed turbulent swirl-burner. *Combustion and Flame*, 155 (1):247–266, Oct. 2008. ISSN 0010-2180. doi: 10.1016/j.combustflame.2008.04.004.

[39] F. Gargouri. *Application of Iterative Solvers in Themoacoustics*. Bachelor's Thesis, Technical University of Munich, Nov. 2017.

[40] A. Ghani, T. Poinsot, L. Gicquel, and J.-D. Müller. LES Study of Transverse Acoustic Instabilities in a Swirled Kerosene/Air Combustion Chamber. *Flow, Turbulence and Combustion*, 96(1):207–226, 2016. ISSN 1386-6184, 1573-1987. doi: 10.1007/s10494-015-9654-9.

[41] A. Giauque, T. Poinsot, W. Polifke, and F. Nicoud. Validation of a Flame Tranfer Function Reconstruction Method for Complex Turbulent Configurations. Technical report, CERFACS, Toulouse, France, 2008.

[42] J. Gikadi, S. Föller, and T. Sattelmayer. Impact of turbulence on the prediction of linear aeroacoustic interactions: Acoustic response of a turbulent shear layer. *Journal of Sound and Vibration*, 333(24):6548–6559, Dec. 2014. ISSN 0022-460X. doi: 10.1016/j.jsv.2014.06.033.

[43] D. G. Goodwin, H. K. Moffat, and R. L. Speth. Cantera: An Object-Oriented Software Toolkit for Chemical Kinetics, Thermodynamics, and Transport Processes. http://www.cantera.org, 2016.

[44] S. Guo, C. F. Silva, M. Bauerheim, A. Ghani, and W. Polifke. Evaluating the impact of uncertainty in flame impulse response model on thermoacoustic instability prediction: A dimensionality reduction approach. *Proceedings of the Combustion Institute*, 37:5299–5306, 2019. doi: 10.1016/j.proci.2018.07.020.

[45] S. Guo, C. F. Silva, A. Ghani, and W. Polifke. Quantification and Propagation of Uncertainties in Identification of Flame Impulse Response for Thermoacoustic Stability Analysis. *J. Eng. Gas Turbines and Power*, 141(2):021032–10, Feb. 2019. ISSN 0742-4795. doi: 10.1115/1.4041652.

[46] S. Guo, C. F. Silva, and W. Polifke. Efficient Robust Design for Thermoacoustic Instability Analysis: A Gaussian Process Approach. *Journal of Engineering for Gas Turbines and Power*, 142(3), Mar. 2020. ISSN 0742-4795. doi: 10.1115/1.4044197.

[47] S. Guo, C. F. Silva, and W. Polifke. Reliable Calculation of Thermoacoustic Instability Risk Using an Imperfect Surrogate Model. *Journal of Engineering for Gas Turbines and Power*, Volume 143(Issue 1):011010 (9 pages), Dec. 2020. ISSN 0742-4795. doi: 10.1115/1.4049314.

[48] S. Guo, C. F. Silva, and W. Polifke. A Gaussian-Process-based framework for high-dimensional uncertainty quantification analysis in thermoacoustic instability prediction. *Proceedings of the Combustion Institute*, 38(4):6251–6259, Jan. 2021. doi: 10.1016/j.proci.2020.06.229.

[49] S. Guo, C. F. Silva, and W. Polifke. Robust identification of flame frequency response via multi-fidelity Gaussian process approach. *Journal of Sound and Vibration*, 502:116083, June 2021. ISSN 0022-460X. doi: 10.1016/j.jsv.2021.116083.

[50] S. Hosder, R. Walters, and R. Perez. A Non-Intrusive Polynomial Chaos Method For Uncertainty Propagation in CFD Simulations. In *44th AIAA Aerospace Sciences Meeting and Exhibit*. American Institute of Aeronautics and Astronautics. doi: 10.2514/6.2006-891.

[51] S. Hosder, R. Walters, and M. Balch. Efficient Sampling for Non-Intrusive Polynomial Chaos Applications with Multiple Uncertain Input Variables. In *48th AIAA/ASME/ASCE/AHS/ASC Structures, Structural Dynamics, and Materials Conference*, Structures, Structural Dynamics, and Materials and Co-Located Conferences. American Institute of Aeronautics and Astronautics, Apr. 2007. doi: 10.2514/6.2007-1939.

[52] S. Hosder, R. Walters, and M. Balch. Efficient Uncertainty Quantification Applied to the Aeroelastic Analysis of a Transonic Wing. *Proceedings of the 46th AIAA Aerospace Sciences Meeting and Exhibit (2008, Reno, NV)*, Jan. 2008. doi: 10.2514/6.2008-729.

[53] T. Hummel, F. Berger, M. Hertweck, B. Schuermans, and T. Sattelmayer. High-Frequency Thermoacoustic Modulation Mechanisms in Swirl-Stabilized Gas Turbine Combustors—Part II: Modeling and Analysis. *Journal of Engineering for Gas Turbines and Power*, 139(7):071502–071502–10, Feb. 2017. ISSN 0742-4795. doi: 10.1115/1.4035592.

[54] M. Ihme and H. Pitsch. Prediction of extinction and reignition in nonpremixed turbulent flames using a flamelet/progress variable model: 2. Application in LES of Sandia flames D and E. *Combustion and Flame*, 155(1):90–107, Oct. 2008. ISSN 0010-2180. doi: 10.1016/j.combustflame.2008.04.015.

[55] A. Javareshkian. *Investigation of Premixed Turbulent Flame Dynamics by Means of LES with Stochastic Fields and Tabulated Chemistry*. Master's Thesis, Technical University of Munich / Politecnico Milano, 2017.

[56] M. P. Juniper and R. I. Sujith. Sensitivity and Nonlinearity of Thermoacoustic Oscillations. *Annual Review of Fluid Mechanics*, 50(1):661–689, 2018. doi: 10.1146/annurev-fluid-122316-045125.

[57] K. A. Kemenov and S. B. Pope. Molecular diffusion effects in LES of a piloted methane–air flame. *Combustion and Flame*, 158(2):240–254, Feb. 2011. ISSN 0010-2180. doi: 10.1016/j.combustflame.2010.08.014.

[58] K. A. Kemenov, H. Wang, and S. B. Pope. Modelling effects of subgrid-scale mixture fraction variance in LES of a piloted diffusion flame. *Combustion Theory and Modelling*, 16(4):611–638, Aug. 2012. ISSN 1364-7830. doi: 10.1080/13647830.2011.645881.

[59] K. T. Kim, H. J. Lee, J. G. Lee, B. D. Quay, and D. Santavicca. Flame Transfer Function Measurement and Instability Frequency Prediction Using a Thermoacoustic Model. In *Int'l Gas Turbine and Aeroengine Congress & Exposition*, GT2009-60026, pages 799–810, Orlando, FL, Jan. 2009. doi: 10.1115/GT2009-60026.

[60] T. Komarek and W. Polifke. Impact of Swirl Fluctuations on the Flame Response of a Perfectly Premixed Swirl Burner. *Journal of Engineering for Gas Turbines and Power*, 132(6):061503, June 2010. doi: 10.1115/1.4000127.

[61] M. Kühn. *Linearized Reactive Flow with Equivalence Ratio Perturbations*. Semester Thesis, Technical University of Munich, 2017.

[62] R. Kulkarni and W. Polifke. LES of Delft-Jet-In-Hot-Coflow (DJHC) with Tabulated Chemistry and Stochastic Fields Combustion Model. *Fuel Processing Technology*, 107: 138–146, 2013. doi: 10.1016/j.fuproc.2012.06.015.

[63] R. Kulkarni, M. Zellhuber, and W. Polifke. LES Based Investigation of Autoignition in Turbulent Co-flow Configurations. *Combustion Theory and Modelling*, 17:224–259, 2013. doi: 10.1080/13647830.2012.739711.

[64] R. Kulkarni, B. Bunkute, F. Biagioli, M. Düsing, and W. Polifke. Large Eddy Simulation of ALSTOM's Reheat Combustor using Tabulated Chemistry and Stochastic Fields Combustion Model. In *Proceedings of ASME Turbo Expo 2014*, GT2014-26053, Düsseldorf, Germany, 2014. doi: 10.1115/GT2014-26053.

[65] R. Lehoucq and D. Sorensen. Deflation Techniques for an Implicitly Restarted Arnoldi Iteration. *SIAM Journal on Matrix Analysis and Applications*, 17(4):789–821, Oct. 1996. ISSN 0895-4798. doi: 10.1137/S0895479895281484.

[66] T. Lieuwen and V. Yang, editors. *Combustion Instabilities in Gas Turbine Engines: Operational Experience, Fundamental Mechanisms and Modeling*. Number v. 210 in Progress in Astronautics and Aeronautics. American Institute of Aeronautics and Astronautics, Reston, VA, 2005. ISBN 978-1-56347-669-3.

[67] M. Meindl, A. Albayrak, and W. Polifke. A state-space formulation of a discontinuous Galerkin method for thermoacoustic stability analysis. *Journal of Sound and Vibration*, 481:115431, 2020. doi: 10.1016/j.jsv.2020.115431.

[68] M. Meindl, C. F. Silva, and W. Polifke. On the spurious entropy generation encountered in hybrid linear thermoacoustic models. *Combustion and Flame*, 223:525–540, Jan. 2021. ISSN 00102180. doi: 10.1016/j.combustflame.2020.09.018.

[69] G. A. Mensah, L. Magri, and J. P. Moeck. Methods for the Calculation of Thermoacoustic Stability Margins and Monte Carlo-Free Uncertainty Quantification. In *Proceedings of ASME Turbo Expo 2017: Turbomachinery Technical Conference and Exposition*, Charlotte, NC, USA, June 2017. ASME. doi: 10.1115/GT2017-64829.

[70] Y. Méry. Impact of Heat Release Global Fluctuations and Flame Motion on Transverse Acoustic Wave Stability. *Proceedings of the Combustion Institute*, 36(3):3889–3898, 2017. ISSN 1540-7489. doi: 10.1016/j.proci.2016.08.009.

[71] Y. Méry. Dynamical response of a perfectly premixed flame and limit behavior for high power density systems. *Combustion and Flame*, 192:410–425, June 2018. ISSN 0010-2180. doi: 10.1016/j.combustflame.2018.02.007.

[72] N. Metropolis and S. Ulam. The Monte Carlo Method. *Journal of the American Statistical Association*, 44(247):335–341, Sept. 1949. ISSN 0162-1459. doi: 10.1080/01621459.1949.10483310.

[73] J.-B. Michel, O. Colin, and C. Angelberger. On the formulation of species reaction rates in the context of multi-species CFD codes using complex chemistry tabulation techniques. *Combustion and Flame*, 157(4):701–714, Apr. 2010. ISSN 0010-2180. doi: 10.1016/j.combustflame.2009.12.014.

[74] V. Nair, S. Sarkar, and R. I. Sujith. Uncertainty quantification of subcritical bifurcations. *Probabilistic Engineering Mechanics*, 34:177–188, Oct. 2013. ISSN 0266-8920. doi: 10.1016/j.probengmech.2013.09.005.

[75] H. N. Najm. Uncertainty quantification and polynomial chaos techniques in computational fluid dynamics. *Annual Review of Fluid Mechanics*, 41:35–52, 2009.

[76] A. Ndiaye, M. Bauerheim, and F. Nicoud. Uncertainty Quantification of Thermoacoustic Instabilities on A Swirled Stabilized Combustor. In *Proceedings of the ASME Turbo Expo 2015: Turbine Technical Conference and Exposition*, GT2015-44133, Montreal, Quebec, Canada, June 2015. ASME. doi: 10.1115/GT2015-44133.

[77] F. Nicoud and F. Ducros. Subgrid-Scale Stress Modelling Based on the Square of the Velocity Gradient Tensor. *Flow Turbulence and Combustion*, 62(3):183–200, 1999. doi: 10.1023/A:1009995426001.

[78] F. Nicoud and T. Poinsot. Thermoacoustic instabilities: Should the Rayleigh criterion be extended to include entropy changes? *Combust. and Flame*, 142(1-2):153–159, 2005. doi: 10.1016/j.combustflame.2005.02.013.

[79] F. Nicoud, L. Benoit, C. Sensiau, and T. Poinsot. Acoustic Modes in Combustors with Complex Impedances and Multidimensional Active Flames. *AIAA Journal*, 45(2):426–441, 2007. doi: 10.2514/1.24933.

[80] N. Noiray and B. Schuermans. Deterministic quantities characterizing noise driven Hopf bifurcations in gas turbine combustors. *International Journal of Non-Linear Mechanics*, 2012.

[81] C. Pankiewitz and T. Sattelmayer. Time Domain Simulation of Combustion Instabilities in Annular Combustors. In *Int'l Gas Turbine and Aeroengine Congress & Exposition*, GT-2002-30063, Amsterdam, NL, 2002. ASME.

[82] C. Pera, O. Colin, and S. Jay. Development of a FPI Detailed Chemistry Tabulation Methodology for Internal Combustion Engines. *Oil & Gas Science and Technology - Revue de l'IFP*, 64(3):243–258, May 2009. ISSN 1294-4475, 1953-8189. doi: 10.2516/ogst/2009002.

[83] N. Peters. Laminar Flamelet Concepts in Turbulent Combustion. *Proc. Combust. Inst*, 21:1231–1250, 1986.

[84] E. L. Petersen, D. M. Kalitan, S. Simmons, G. Bourque, H. J. Curran, and J. M. Simmie. Methane/propane oxidation at high pressures: Experimental and detailed chemical kinetic modeling. *Proceedings of the Combustion Institute*, 31(1):447–454, Jan. 2007. ISSN 1540-7489. doi: 10.1016/j.proci.2006.08.034.

[85] C. Pierce and P. Moin. Progress-variable approach for large-eddy simulation of non-premixed turbulent combustion. *Journal of Fluid Mechanics*, 504:73–97, 2004.

[86] T. Poinsot and S. K. Lele. Boundary Conditions for Direct Simulation of Compressible Viscous Flows. *Journal of Computational Physics*, 101(1):104–129, 1992. doi: 10.1016/0021-9991(92)90046-2.

[87] T. Poinsot and D. Veynante. *Theoretical and Numerical Combustion*. CNRS, Paris, third edition, 2012. ISBN 978-2-7466-3990-4.

[88] W. Polifke. Black-Box System Identification for Reduced Order Model Construction. *Annals of Nuclear Energy*, 67C:109–128, May 2014. ISSN 0306-4549. doi: 10.1016/j.anucene.2013.10.037.

[89] W. Polifke. Modeling and Analysis of Premixed Flame Dynamics by Means of Distributed Time Delays. *Prog. Energy Combust. Sci.*, 79:100845, 2020. doi: 10.1016/j.pecs.2020.100845.

[90] W. Polifke, C. O. Paschereit, and K. Döbbeling. Constructive and Destructive Interference of Acoustic and Entropy Waves in a Premixed Combustor with a Choked Exit. *International Journal of Acoustics and Vibration*, 6(3):135–146, 2001. doi: 10.20855/ijav.2001.6.382.

[91] M. T. Reagan, H. N. Najm, R. G. Ghanem, and O. M. Knio. Uncertainty quantification in reacting-flow simulations through non-intrusive spectral projection. *Combustion and*

Flame, 132(3):545–555, Feb. 2003. ISSN 0010-2180. doi: 10.1016/S0010-2180(02)00503-5.

[92] D. E. Rogers and F. E. Marble. A mechanism for high-frequency oscillations in ramjet combustors and afterburners. *Jet Propulsion*, (Rogers56):456–462, 1956.

[93] A. Saghafian, V. E. Terrapon, and H. Pitsch. An efficient flamelet-based combustion model for compressible flows. *Combustion and Flame*, 162(3):652–667, Mar. 2015. ISSN 0010-2180. doi: 10.1016/j.combustflame.2014.08.007.

[94] S. Schlimpert, M. Meinke, and W. Schröder. Nonlinear Analysis of an Acoustically Excited Laminar Premixed Flame. *Combustion and Flame*, 163:337–357, 2016. ISSN 0010-2180. doi: 10.1016/j.combustflame.2015.09.035.

[95] M. Schulze, T. Hummel, N. Klarmann, F. M. Berger, B. Schuermans, and T. Sattelmayer. Linearized Euler Equations for the Prediction of Linear High-Frequency Stability in Gas Turbine Combustors. *Journal of Engineering for Gas Turbines and Power*, 139 (3):031510, Mar. 2017. ISSN 0742-4795, 1528-8919. doi: 10.1115/1.4034453.

[96] J. Schwing and T. Sattelmayer. High-Frequency Instabilities in Cylindrical Flame Tubes: Feedback Mechanism and Damping. In *ASME Turbo Expo 2013: Turbine Technical Conference and Exposition*, page V01AT04A003, June 2013. doi: 10.1115/GT2013-94064.

[97] V. Sharifi, A. M. Kempf, and C. Beck. Large-Eddy Simulation of Acoustic Flame Response to High-Frequency Transverse Excitations. *AIAA Journal*, 57(1):1–14, 2019. ISSN 0001-1452. doi: 10.2514/1.J056818.

[98] Shreekrishna, S. Hemchandra, and T. Lieuwen. Premixed Flame Response to Equivalence Ratio Perturbations. *Combustion Theory and Modelling*, 14(5):681–714, 2010. ISSN 1364-7830. doi: 10.1080/13647830.2010.502247.

[99] C. F. Silva, F. Nicoud, T. Schuller, D. Durox, and S. Candel. Combining a Helmholtz solver with the flame describing function to assess combustion instability in a premixed swirled combustor. *Combustion and Flame*, 160(9):1743–1754, Sept. 2013. ISSN 0010-2180. doi: 10.1016/j.combustflame.2013.03.020.

[100] C. F. Silva, L. Magri, T. Runte, and W. Polifke. Uncertainty quantification of growth rates of thermoacoustic instability by an adjoint Helmholtz solver. *J. Eng. Gas Turbines and Power*, 139(1):011901, 2017. doi: 10.1115/1.4034203.

[101] I. Sobol'. Sensitivity Estimates for Nonlinear Mathematical Models. *Mathematical Modeling & Computational Experiment*, 1:407–414, 1993.

[102] P. Subramanian, R. S. Blumenthal, R. Sujith, and W. Polifke. Distributed Time Lag Response Functions for the Modelling of Combustion Dynamics. *Combustion Theory and Modelling*, 19(2):223–237, Feb. 2015. ISSN 1364-7830. doi: 10.1080/13647830.2014.1001438.

[103] L. Tay-Wo-Chong, R. Kaess, T. Komarek, S. Föller, and W. Polifke. Identification of Flame Transfer Functions Using LES of Turbulent Reacting Flows. In S. Wagner,

M. Steinmetz, A. Bode, and M. Müller, editors, *High Performance Computing in Science and Engineering*, ISBN 978-3-642-13871-3, pages 255–266. Springer, 2010. ISBN 3-642-13871-3.

[104] L. Tay-Wo-Chong, T. Komarek, R. Kaess, S. Föller, and W. Polifke. Identification of Flame Transfer Functions from LES of a Premixed Swirl Burner. In *Proceedings of ASME Turbo Expo 2010*, GT2010-22769, pages 623–635, Glasgow, UK, June 2010. ASME. ISBN 978-0-7918-4397-0. doi: 10.1115/GT2010-22769.

[105] L. Tay-Wo-Chong, S. Bomberg, A. Ulhaq, T. Komarek, and W. Polifke. Comparative Validation Study on Identification of Premixed Flame Transfer Function. *Journal of Engineering for Gas Turbines and Power*, 134(2):021502–1–8, 2012. doi: 10.1115/1.4004183.

[106] L. Tay-Wo-Chong, A. Scarpato, and W. Polifke. LES Combustion Model with Stretch and Heat Loss Effects for Prediction of Premix Flame Characteristics and Dynamics. In *ASME Turbo Expo 2017: Turbomachinery Technical Conference and Exposition*, GT2017-63357, Charlotte, NC, USA, 2017. ASME. doi: 10.1115/GT2017-63357.

[107] V. K. Tritschler, A. Avdonin, S. Hickel, X. Y. Hu, and N. A. Adams. Quantification of initial-data uncertainty on a shock-accelerated gas cylinder. *Physics of Fluids*, 26(2): 026101, Feb. 2014. ISSN 1070-6631. doi: 10.1063/1.4865756.

[108] E. van den Berg and M. Friedlander. Probing the Pareto Frontier for Basis Pursuit Solutions. *SIAM Journal on Scientific Computing*, 31(2):890–912, Nov. 2008. ISSN 1064-8275. doi: 10.1137/080714488.

[109] J. F. van Kampen, J. B. W. Kok, and T. H. van der Meer. Efficient Retrieval of the Thermo-Acoustic Flame Transfer Function from a Linearized CFD Simulation of a Turbulent Flame. *International Journal for Numerical Methods in Fluids*, 54(9):1131–1149, July 2007. ISSN 1097-0363. doi: 10.1002/fld.1424.

[110] C. K. Westbrook and F. L. Dryer. Simplified Reaction Mechanisms for the Oxidation of Hydrocarbon Fuels in Flames. *Combustion Science and Technology*, 27(1-2):31–43, Dec. 1981. ISSN 0010-2202. doi: 10.1080/00102208108946970.

[111] S. Zahirovic and K. Knapp. Ansaldo GT26 Sequential Combustor Performance in Long-Term Commercial Operation. In *Volume 4B: Combustion, Fuels and Emissions*, page V04BT04A008, Charlotte, North Carolina, USA, June 2017. American Society of Mechanical Engineers. ISBN 978-0-7918-5085-5. doi: 10.1115/GT2017-64289.

[112] M. Zahn, M. Betz, M. Schulze, C. Hirsch, and T. Sattelmayer. Predicting the Influence of Damping Devices on the Stability Margin of an Annular Combustor. page V04AT04A081, June 2017. doi: 10.1115/GT2017-64238.

[113] M. Zellhuber, B. Schuermans, and W. Polifke. Impact of Acoustic Pressure on Auto-Ignition and Heat Release. *Combustion Theory and Modelling*, 18:1–31, 2014. doi: 10.1080/13647830.2013.817609.

[114] M. Zellhuber, J. Schwing, B. Schuermans, T. Sattelmayer, and W. Polifke. Experimental and Numerical Investigation of Thermo-Acoustic Sources Related to High-Frequency Instabilities. *Int. J. Spray and Combustion Dynamics*, 6:1–34, 2014. doi: 10.1260/1756-8277.6.1.1.

[115] J. Zips, H. Müller, and M. Pfitzner. Efficient Thermo-Chemistry Tabulation for Non-Premixed Combustion at High-Pressure Conditions. *Flow, Turbulence and Combustion*, 101(3):832–850, 2018. ISSN 1573-1987. doi: 10.1007/s10494-018-9932-4.